Summer 2009

Still oxides run deep: studying redox transformations involving Fe and Mn oxides using selective isotope techniques

Robert Michael Handler
University of Iowa

STILL OXIDES RUN DEEP: STUDYING REDOX TRANSFORMATIONS INVOLVING FE AND MN OXIDES USING SELECTIVE ISOTOPE TECHNIQUES

by

Robert Michael Handler

An Abstract

Of a thesis submitted in partial fulfillment
of the requirements for the Doctor of
Philosophy degree in Civil and Environmental Engineering
in the Graduate College of
The University of Iowa

July 2009

Thesis Supervisor: Associate Professor Michelle M. Scherer

ABSTRACT

Reactions of aqueous Fe(II) with Fe and Mn oxides influence heavy metal mobility, transformation of trace organics, and important elemental cycles as Fe precipitates form or dissolve, and as electrons move between aqueous and solid phases. Our objective was to characterize reactions of Fe(II) with important metal oxides, using a suite of complementary tools to investigate the extent and underlying mechanisms of Fe(II)-metal oxide redox activity.

Nanoscale materials (1-100 nm) may have fundamentally different surface or electronic properties than larger solids. Goethite was synthesized with primary particle dimensions above or below the nanoscale. Despite large differences in particle surface area, goethite nanorods and microrods had similar net Fe(II) sorption and electron transfer properties. Experimental evidence suggested particle aggregation resulted in particle complexes of a similar size, meaning considerations of available reactive surface area could explain our results.

Kinetics and extent of Fe(II)-Fe(III) redox reactions between aqueous Fe(II) and goethite were examined using a stable isotope tracer approach. Aqueous Fe(II) that had been enriched in ^{57}Fe was mixed with isotopically-normal goethite. Convergence of Fe isotope ratios in aqueous and solid phases to values predicted by complete Fe atom exchange provided evidence that all goethite Fe(III) atoms could eventually react with Fe(II), despite no evidence for complete atom exchange from bulk measurements of the aqueous or solid phase. Fe isotope data at different experimental conditions was combined with theoretical considerations governing electron transfer in goethite to provide evidence for redox-driven atom exchange involving bulk conduction of electrons between spatially distinct Fe(II) sorption and release sites. Procedures for stable Fe isotope tracer studies have been adapted to investigate redox transformations of magnetite solids with different divalent cation content.

Evolution of aqueous Fe(II)-Mn(IV) redox reactions was examined using complementary techniques. After pyrolusite particles were exposed to aqueous Fe(II), aqueous Fe and Mn were analyzed, and X-ray diffraction was utilized with electron microscopy to assess solid phase evolution during continued exposure to Fe(II). Selective use of Fe isotopes during Fe(II) resuspensions allowed us to track chemical changes occurring to one particular Fe addition using ^{57}Fe Mössbauer spectroscopy.

Abstract Approved: _____
Thesis Supervisor

_____
Title and Department

_____
Date

STILL OXIDES RUN DEEP: STUDYING REDOX TRANSFORMATIONS INVOLVING FE AND MN OXIDES USING SELECTIVE ISOTOPE TECHNIQUES

by

Robert Michael Handler

A thesis submitted in partial fulfillment
of the requirements for the Doctor of
Philosophy degree in Civil and Environmental Engineering
in the Graduate College of
The University of Iowa

July 2009

Thesis Supervisor: Associate Professor Michelle M. Scherer

Graduate College
The University of Iowa
Iowa City, Iowa

CERTIFICATE OF APPROVAL

PH.D. THESIS

This is to certify that the Ph.D. thesis of

Robert Michael Handler

has been approved by the Examining Committee
for the thesis requirement for the Doctor of Philosophy
degree in Civil and Environmental Engineering at the July 2009 graduation.

Thesis Committee: _____
Michelle M. Scherer, Thesis Supervisor

_____
Vicki H. Grassian

_____
Clark M. Johnson

_____
Gene F. Parkin

_____
Richard L. Valentine

In the realm of ideas, everything depends on enthusiasm...
in the real world, all rests on perseverance.
Johann Wolfgang von Goethe

ACKNOWLEDGMENTS

I would like to begin by thanking my wife Shannon for all of her support over the past few years – really, the past $^{1}/_{3}$ of my life! Graduate school has been demanding, and when I think about the amount of time that it has kept me away from home, I often feel extremely guilty. It's amazing that you were always glad to see me at the end of a long night! Shannon, you have been a wonderful companion, and I couldn't have done it without you.

I love you.

I also have to thank my advisor Michelle for the past five years. I would imagine that most people don't really know what they are truly getting into when they sign up for graduate school, and I certainly was no different. I am so lucky to have stumbled into such a great advisor. You have been a wonderful role model as a scientist and as a person. As much as I have enjoyed the thought-provoking science, I could just as easily talk to you about gardening or your kids and have just as much fun! My time at Iowa has come in the middle of several new challenges for you, some much more exciting than others – watching you navigate your life and career with grace, integrity, and good humor has been the best instruction of all.

A big thanks goes out to my committee members, and the rest of the faculty in the Dept. of Environmental Engineering. Vicki and Clark, it has been a great advantage to have access to such high-caliber brainpower, and your enthusiasm for research has been infectious. To Craig, Gene, Jerry, Keri, Michelle, Rich, and Tim – what a group! You have built quite a community here, which we are all lucky to be a part of. How can your hearts so big, to be so nice to everyone you meet for this many years? It must be exhausting.

I would like to thank Brian Beard at UW-Madison for his tremendous support on stable Fe isotope analysis, and his willingness to guide me through the process of

interpreting some pretty complex data. Adrianna Heimann, Andy Czaja, and Lingling Wu also provided a great deal of support in sample preparation for mass spectrometry. Staff members at University of Iowa Central Microscopy, particularly Jonas Baltrusaitis and Jean Ross, were very helpful and patient as I learned a variety of microscopic techniques. John Pettibone was nice enough to assist me on the court and in the lab, particularly with BET analysis.

I am thankful for the support of Angie, Collin, Ginny, and Judy – there is absolutely no way I would have made it through without your help. I was unable to find a problem that you couldn't solve, and you even managed to be nice the entire time! Collin, thank you for letting me donate to the EES basketball pool every year, just know that I'm planning a huge comeback next time around.

I would like to thank all of my fellow students, past and present, for enriching my time in graduate school. I may never get another opportunity to meet such a large group of friendly people – this should make me sad, but it makes me smile when I scroll through all of your faces in my mind. It will be fun to have so many friends in so many different places! The friends I have made here will last me a lifetime. I would like to thank the members of the Scherer research group – Aaron, Korey, Justine, Sharon, Phil, Tim P, David, Chris, Drew, Mike, Angela, Cristina, and Tim P. again – for making it all so enjoyable. Special thanks go out to Phil and David for teaching me how to work and how to think, to Chris and Mike for being fantastic co-workers, and to Drew for blessing us with a shared Rhapsody account.

ABSTRACT

Reactions of aqueous Fe(II) with Fe and Mn oxides influence heavy metal mobility, transformation of trace organics, and important elemental cycles as Fe precipitates form or dissolve, and as electrons move between aqueous and solid phases. Our objective was to characterize reactions of Fe(II) with important metal oxides, using a suite of complementary tools to investigate the extent and underlying mechanisms of Fe(II)-metal oxide redox activity.

Nanoscale materials (1-100 nm) may have fundamentally different surface or electronic properties than larger solids. Goethite was synthesized with primary particle dimensions above or below the nanoscale. Despite large differences in particle surface area, goethite nanorods and microrods had similar net Fe(II) sorption and electron transfer properties. Experimental evidence suggested particle aggregation resulted in particle complexes of a similar size, meaning considerations of available reactive surface area could explain our results.

Kinetics and extent of Fe(II)-Fe(III) redox reactions between aqueous Fe(II) and goethite were examined using a stable isotope tracer approach. Aqueous Fe(II) that had been enriched in ^{57}Fe was mixed with isotopically-normal goethite. Convergence of Fe isotope ratios in aqueous and solid phases to values predicted by complete Fe atom exchange provided evidence that all goethite Fe(III) atoms could eventually react with Fe(II), despite no evidence for complete atom exchange from bulk measurements of the aqueous or solid phase. Fe isotope data at different experimental conditions was combined with theoretical considerations governing electron transfer in goethite to provide evidence for redox-driven atom exchange involving bulk conduction of electrons between spatially distinct Fe(II) sorption and release sites. Procedures for stable Fe isotope tracer studies have been adapted to investigate redox transformations of magnetite solids with different divalent cation content.

Evolution of aqueous Fe(II)-Mn(IV) redox reactions was examined using complementary techniques. After pyrolusite particles were exposed to aqueous Fe(II), aqueous Fe and Mn were analyzed, and X-ray diffraction was utilized with electron microscopy to assess solid phase evolution during continued exposure to Fe(II). Selective use of Fe isotopes during Fe(II) resuspensions allowed us to track chemical changes occurring to one particular Fe addition using ^{57}Fe Mössbauer spectroscopy.

TABLE OF CONTENTS

LIST OF TABLES

LIST OF FIGURES

CHAPTER 1: INTRODUCTION

Overview

Iron (Fe) and manganese (Mn) oxides are common constituents of the Earth's crust (*1*). Redox transitions between oxidized and reduced forms of Fe and Mn influence the availability and transformation of countless chemical species, such as nitrogen (*2*), arsenic (*3*), and trace organics (*4*). These transitions between Fe(II) and Fe(III) or Mn(II), Mn(III), and Mn(IV) are often catalyzed by microbial action, although redox reactions can also occur through abiotic mechanisms (e.g., *5, 6*). Reduced forms of Fe and Mn often exist in the aqueous phase while oxidized Fe(III) and Mn are much less soluble, which makes their heterogeneous redox chemistry an important pathway for solid and aqueous species to interact through the formation and dissolution of Fe and Mn. Ferrous iron also serves as an important reductant in natural and engineered settings. Fe(II) associated with mineral surfaces has been demonstrated to reduce a variety of chemical species of concern, including heavy metals and trace organics (*7, 8*). It is important to understand the availability and intrinsic ability of Fe(II) to participate in redox reactions with chemical species of concern in a variety of scenarios, especially in relation to the solid mineral phases that are also present and potentially participating in competing redox reactions with aqueous Fe(II). An improved understanding of the dynamics and extent of redox reactions between Fe and Mn oxides and aqueous Fe(II) would aid in efforts to model and predict environmental outcomes based on a given set of biogeochemical conditions.

Initial work on the interaction of aqueous Fe(II) and Fe oxides treated Fe(II) as a typical cationic sorbent, which would associate with the solid surface and disassociate as solution conditions (pH, Fe(II) concentration, etc.) were changed (e.g., *9*). This view of Fe(II) acting as a passive sorbent on Fe(III) oxides has become complicated in recent years, as evidence is accumulating that indicates reduced Fe(II) can participate in redox

reactions with Fe(III) oxides. Rather than viewing Fe(II) interactions with Fe(III) oxides as a simple process that is relatively static, we are seeing now that Fe(II)-Fe oxide interactions are dynamic processes where Fe(II) electron transfer to underlying Fe oxides can be coupled to new mineral formation, conduction of electrons through the solid, and/or reductive dissolution of Fe (*10-14*). Geochemical factors controlling all of these processes, as well as implications of these recently-elucidated mechanisms on contaminant fate in environmental settings, are issues that require further study.

Interactions between Fe(II) and manganese oxides have typically been viewed as a heterogeneous redox reaction as opposed to a sorbent-sorbate interaction, due to clear thermodynamic indications that oxidation of Fe(II) would occur in the presence of oxidized Mn species. What has not been made clear, however, is the chemical nature of the reaction products occurring as a result of Fe-Mn redox activity, or the implications of Fe oxidation products on overall solid phase redox capacity. In previous work, characterization of Fe(III) reaction products was made difficult by the low mass % of solid Fe formed in relation to the underlying Mn solid (*15, 16*). Also, production of aqueous Mn was less than predicted by considerations of theoretical reaction stoichiometry, and often complicated by inability of colorimetric methods to speciate oxidation states of Mn (*15, 17*). Questions also remain concerning environmental implications of Fe-Mn redox reactions involving Mn oxides. Initial reports have indicated Fe precipitates may form a "passivating" surface layer on Mn oxides, preventing further Mn redox chemistry from taking place (*18, 19*). Evaluation of these claims under a wide variety of geochemical conditions is required to have a better understanding of effects on beneficial (e.g., oxidation of organics (*20*)) or undesirable (e.g., Cr(VI) production (*21*)) Mn redox activity.

Of particular interest in the course of this work was the influence of primary particle size on reactions between Fe(II) and Fe oxides, particularly as solids enter the nanoscale, with one or more dimensions of 100 nm or less. As solids decease in size,

reactivity is increasingly governed by quantum effects between a discrete number of atoms, which may give nanoscale materials drastically different physical and chemical properties than bulk solids of the same chemical composition (e.g., *22, 23*). Although a variety of Fe oxides may exist in the nanoscale, goethite was chosen due to its prevalence in natural environments, both as a bulk oxide and as a nanoscale material (*24, 25*).

Complementary Enriched Isotope Studies

Analysis of interactions between separate Fe phases, such as reduced Fe(II) and Fe oxides, can often be complicated by the inability to distinguish between Fe atoms in most common analytical procedures measuring bulk characteristics of the aqueous or solid phase. Colorimetric Fe measurements can quantify Fe concentrations in solution, but cannot distinguish between atoms in the aqueous phase that simply remained in the aqueous phase or aqueous atoms that were initially bound in the Fe solid. Similarly, X-ray diffraction or extended X-ray absorption studies may reveal bulk chemical composition of solids, but can not determine the contributions of initially distinct metal cations to any particular solid phase. One general solution to this basic problem is to utilize differences in Fe atoms that can be detected in various types of instrumentation - namely, differences between Fe isotopes of different atomic mass.

This approach has been used by members of our group in conjunction with ^{57}Fe Mössbauer spectroscopy. Fe oxides synthesized using Mössbauer-invisible ^{56}Fe were reacted with Mössbauer-active ^{57}Fe(II), or ^{57}Fe(III) oxides were reacted with ^{56}Fe(II). Resulting spectral characteristics of ^{57}Fe atoms after reaction indicated that Fe atoms initially present as aqueous Fe(II) had become oxidized into a ferric solid with similar composition to the initial Fe(III) oxide, and Fe(III) atoms within the solid were reduced to Fe(II) (*11, 26*), providing evidence for electron transfer between aqueous Fe(II) and Fe(III) oxides.

Recent developments in mass spectroscopy (multi-collector inductively-coupled plasma mass spectrometry or MC-ICP-MS) have allowed researchers to measure small deviations in isotope distributions of heavy elements like Fe with great precision, and with greater speed than previous methods. Using this advanced instrumentation, researchers can monitor isotope distributions of compounds as different stable isotopes are preferentially used in a chemical reaction, or as they move between different elemental reservoirs, and infer reaction kinetics and mechanisms based on these outcomes (e.g., *27, 28*). This analytical tool holds great promise in enabling researchers to investigate biogeochemical processes.

Objective and Hypotheses

Objective

To investigate the mechanisms controlling environmentally relevant Fe(II)-metal oxide redox reactions using novel isotope tracing approaches in conjunction with complimentary traditional tools.

Working Hypotheses

1. Goethite rods in the nanoscale will interact with aqueous Fe(II) to an extent that is not predicted by differences in specific surface area between nanoparticles and larger scale counterparts.
2. Extent of atom exchange between aqueous Fe(II) and goethite is much greater than previously expected, involving more than a "reactive pool" of surface Fe(III) atoms.
3. Fe(II)-goethite atom exchange is facilitated by conduction of electrons through the solid, linking separate sites of Fe(II) oxidation and reductive Fe(II) dissolution.
4. Electron transfer between aqueous Fe(II) and nanoscale goethite will not differ fundamentally from electron transfer involving bulk goethite solids.

5. Rates of Fe(II)-goethite exchange are controlled by processes influencing Fe(II) accessibility to the mineral surface.
6. Redox reactions between Fe(II) and Mn oxides will result in the formation of an Fe(III) precipitate on the Mn oxide surface, but this precipitate will not completely hinder the ability of resulting Mn/Fe particle complexes to participate in environmentally relevant redox reactions.
7. Rates and extent of redox-driven atom exchange between Fe(II) and magnetite will be reduced by decreased initial Fe(II) content or cation substitution into the solid phase.

Thesis Outline

This thesis is organized into five main chapters, each of which is independent and contains sections detailing background information, experimental objectives, experimental approach, results and discussion, and literature cited. A brief summary of the following chapters is included below.

Chapter 2 addresses hypotheses 1. In this study, goethite particles were synthesized with distinct size ranges. Goethite rods with average lengths above and below the nanoscale size range (1-100 nm) were synthesized and characterized. Reactions of these particles with aqueous Fe(II) were assessed using several complementary techniques, and macroscopic Fe(II) sorption behavior was explained using evidence of particle aggregation at specific solution conditions. This chapter is in press in *Geochimica et Cosmochimica Acta*, and consists of the published manuscript and supplementary materials.

Chapter 3 addresses hypotheses 2 and 3. For this work, a stable isotope tracer study was used to track the interaction of aqueous Fe(II) enriched in ^{57}Fe with goethite nanorods containing a normal distribution of Fe isotopes. Despite a stable aqueous Fe(II) concentration after initial net Fe(II) uptake and seemingly unchanging goethite

morphology, Fe isotope analyses reveal that the aqueous Fe(II) and goethite Fe(III) had reached similar isotope distributions over the course of 30 d. Convergence of isotope ratios to the value predicted as a system-wide average calculated by mass balance provides evidence that near-complete atom exchange had occurred between aqueous Fe(II) and goethite. This chapter is in press in *Environmental Science and Technology,* and consists of the published manuscript and supplementary materials.

Chapter 4 of this thesis addresses hypotheses 4 and 5. Mechanistic constraints of Fe(II)-Fe oxide atom exchange observed in chapter 3 were studied by varying experimental conditions (goethite particle size, solution pH) and performing sequential extractions in order to more concretely track the location of electrons and Fe isotopes within the system. Experimental data was placed in the context of different Fe electron transfer and flux models to evaluate the feasibility of a bulk conduction mechanism to explain our observations. This chapter is in preparation for submission to *Geochimica et Cosmochimica Acta.*

Chapter 5 addresses working hypothesis 6. Manganese oxides were reacted with aqueous Fe(II), resulting in production of an Fe(III) precipitate coupled to production of aqueous Mn. Resulting Mn/Fe solids were resuspended in a series of buffer solutions containing aqueous Fe(II) to examine the evolution of Mn-Fe redox activity in this system. Using a combination of X-ray diffraction, electron microscopy, bulk analyses of aqueous Fe and Mn, and selective use of ^{56}Fe(II) or ^{57}Fe(II) additions in conjunction with Mössbauer spectroscopy, we were able to fingerprint the initial Fe(III) precipitate and monitor the continued redox activity of Fe and Mn as additional Fe(II) was introduced. This chapter is in preparation for submission to *Environmental Science and Technology.*

Chapter 6 details recent experimental results collected by adapting our enriched ^{57}Fe(II) isotope tracer approach to the Fe(II)-magnetite system, addressing hypothesis 7. Magnetite solids with a different initial Fe(II) content were compared, as well as magnetite solids in which Co(II) was substituted for Fe(II). Initial magnetite

stoichiometry influenced the rate and extent of observed Fe atom exchange, and Co(II) substitution appears to have restricted Fe atom exchange to the first few surface layers of solid Fe/Co atoms.

The appendix contains supplemental information and figures from chapters 2 and 3, as referred to in the text.

CHAPTER 2: INTERPRETING NANOSCALE SIZE-EFFECTS IN AGGREGATED FE-OXIDE SUSPENSIONS: REACTION OF FE(II) WITH GOETHITE

Abstract

The Fe(II)/Fe(III) redox couple plays an important role in both the subsurface fate and transport of groundwater pollutants and the global cycling of carbon and nitrogen in iron-limited marine environments. Iron oxide particles involved in these redox processes exhibit broad size distributions, and the recent demonstrations of dramatic nanoscale size-effects with various metal oxides has compelled us, as well as many others, to consider whether the rate and extent of Fe(II)/Fe(III) cycling depends upon oxide particle size in natural systems. Here, we investigated the reaction of Fe(II) with three different goethite particle sizes in pH 7.5 suspensions. Acicular goethite rods with primary particle dimensions ranging from 7 by 80 nm to 25 by 670 nm were studied. Similar behavior with respect to Fe(II) sorption, electron transfer and nitrobenzene reduction was observed on a mass-normalized basis despite almost a three-fold difference in their specific surface areas. Scanning electron microscopy (SEM) images, dynamic light scattering and sedimentation measurements all indicated that, at pH 7.5, significant aggregation occurred with all three sizes of goethite particles. SEM images further revealed that nanoscale particles formed dense aggregates on the order of several microns in diameter. The clear formation of particle aggregates in solution raises questions regarding the use of primary particle surface area as a basis for assessing nanoscale size-effects in iron oxide suspensions at circum-neutral pH values. In our case, normalizing the Fe(II) sorption densities and rate constants for nitrobenzene reduction by BET surface area

---

Cwiertny, D. M.; Handler, R. M.; Schaefer, M. V.; Grassian, V. H.; Scherer, M. M. Interpreting nanoscale size-effects in aggregated Fe-oxide suspensions: reaction of Fe(II) with goethite. *Geochimica Cosmochimica Acta,* In Press.

implies that goethite nanoparticles are less reactive than larger particles. We suspect, however, that aggregation is responsible for this observed size-dependence, and argue that BET values should not be used to assess differences in surface site density or intrinsic surface reactivity in aggregated particle suspensions. In order to realistically assess nanoscale size-effects in environmental systems that are likely to aggregate, new methods are needed to quantify the amount of surface area accessible for sorption and reaction in wet nanoparticle suspensions, rather than assuming that this value is equivalent to the surface area determined from the characterization of dry nanoparticles.

Introduction

Ferrous and ferric iron are one of the most familiar environmental redox couples, playing critical roles in air, water and soil systems. In subsurface environments, the Fe(II)-Fe(III) redox cycle is driven by microbial processes, in which bacteria gain energy by using naturally occurring ferric iron solids as terminal electron acceptors (*29, 30*). In addition to contributing to subsurface elemental cycling, such Fe(II)-Fe(III) redox reactions are intricately linked to contaminant fate via the formation of sorbed Fe(II) species on Fe(III) mineral surfaces and biogenic, ferrous iron-containing phases, both of which have been shown to reduce a broad spectrum of common groundwater pollutants (*7, 8, 31-36*).

In natural environments, iron oxides and (oxyhydr)oxides (hereafter collectively referred to as iron oxides) are ubiquitous and often display a broad distribution of particle sizes. Their occurrence in the nanometer size regime has been previously demonstrated, with examples ranging from ultra-fine aerosols (*37*) to precipitates in soils and sediments (*38-40*). Recent field-scale evidence has even suggested a predominance of nanoscale goethite in some natural aquatic systems, where its occurrence was attributed to iron redox cycling at the boundary between anoxic and oxic zones in sediments (*25*). Although the persistence of iron oxides as nanoparticles could result from coprecipitation

or surface complexation that inhibits further growth into larger crystallites (*25*), it is also possible that the surface energies of some oxides are low enough to allow nanoparticles to represent metastable phases (*41*). Because of their large specific surface area, iron oxide nanoparticles could represent, therefore, a key reactive constituent in many environmental systems even though they may only comprise a small fraction of total iron in the system on the basis of mass or volume (*42*).

Because of their prominence in natural environments, as well as their widespread application in industry and catalysis (*24*), the size-dependent properties and reactivity of iron oxides have long been the focus of laboratory investigations (e.g., *43*). Nanoparticles are generally assumed to be more reactive than larger particles, and indeed, many unique size-dependent properties of nanoparticles have been reported (*22, 44*). Although their reactivity is sometimes attributed to very high specific surface areas, recent experimental evidence indicates that iron oxide nanoparticles may display reactive properties that cannot be extrapolated to the behavior of larger materials simply on the basis of surface area differences. These investigations have focused on common iron oxides such as goethite, ferrihydrite and hematite, and have reported enhanced nanoparticle reactivity with respect to interfacial processes such as cation adsorption, electron transfer and oxide dissolution (*23, 45, 46*). Such behavior could result from a greater density of reactive sites per unit surface area on nanoparticle surfaces, or greater inherent reactivity of nanoparticle surface sites relative to sites on larger particles (*47*). In the latter case, factors potentially responsible for the unique reactivity of iron oxide nanoparticles were recently detailed in a review by Waychunas et al. (*42*), and these include surface restructuring, surface curvature, and quantum confinement effects, all of which could emerge as a function of decreasing particle size.

However, the tendency of iron oxides to aggregate under many environmentally relevant conditions can make it difficult to determine whether the observed reactivity of nanoparticle suspensions reflects inherent particle size effects or the behavior of larger

particle aggregates. Aggregation influences the transport (*48*), thermal conductivity (*49, 50*) and toxicity (*51*) of nanoparticles. Others (*52*) have also commented on the likelihood that aggregation impacts nanoparticle redox reactivity by altering the amount of reactive surface area available in suspensions, a scenario that is supported by the relatively few studies that have directly explored the influence of nanoparticle aggregation on interfacial redox reactivity. For example, recent results of Vikesland et al. (*53*) demonstrated that the rate of carbon tetrachloride (CCl_4) reduction by nanoscale magnetite decreased with increasing ionic strength, which was varied to control the extent of aggregation in suspensions. Aggregation was also proposed to influence the extent of Fe(II) uptake and the rate of CCl_4 reduction in suspensions of larger goethite particles (*54*). These findings agree with earlier work from the field of colloid chemistry, where it has long been recognized that reactivity measurements carried out in wet suspensions will be influenced by the system's dispersivity (*55*). These studies suggest that the extent of particle aggregation needs to be considered when assessing whether iron oxides display unique behavioral properties at the nanoscale.

Here, we investigate whether nanoscale size-effects are observed for the reaction of aqueous Fe(II) with goethite. Fe(II) generated from microbial respiration of Fe(III) oxides has been shown to significantly impact oxide dissolution and secondary mineral precipitation, as well as heavy metal sequestration, and contaminant reduction (*7, 14, 32, 56, 57*). Yet despite the importance of Fe(II)-Fe(III) cycling in these processes, the influence of oxide particle size on this redox couple remains relatively unexplored, as is the case for the many geochemically relevant redox processes (*22*).

Our work, as well as the work of several others, has shown that sorption of Fe(II) on Fe(III) oxides involves electron transfer between Fe(II) and structural Fe(III) resulting in reductive dissolution and/or some form of secondary mineral formation (*10, 12, 14, 58, 59*). Previous studies have even suggested that this electron exchange reaction may be impacted by particle size (*60, 61*). Mulvaney and coworkers found that the electrons

transferred to hematite particles by radiolytically generated viologen radicals could either produce surface-bound Fe(II) or be transferred into the bulk of the oxide particle (*60, 62*). Based upon the stoichiometry of the reduction reaction and results of Fe(II) recovery experiments, they proposed that the extent of charge migration into the bulk particle was limited on colloidal iron oxides due to their small bulk volume, in turn producing a greater fraction of surface-bound Fe(II) on nanoparticles relative to larger oxides. Such a scenario has obvious implications for the biogeochemical cycling of iron, as well as pollutant fate in anoxic, reducing environments; if the extent of Fe(II)-Fe(III) interfacial electron exchange decreases with particle size, then a greater fraction of surface-bound Fe(II) may exist on iron oxide nanoparticles, potentially making smaller oxide phases the dominant player in Fe(II)-Fe(III) redox cycling in natural systems.

For our experimental approach, three sizes of goethite particles were synthesized and their reactivity with Fe(II) was examined in batch systems. We investigated the rate of Fe(II) uptake on goethite, as well as the influence of common geochemical variables such as pH, aqueous Fe(II) concentration and goethite solids loading on the extent of Fe(II) uptake. In addition to traditional batch sorption measurements, we used isotope specific ^{57}Fe Mössbauer spectroscopy to investigate interfacial electron transfer between ^{57}Fe(II)(aq) and structural Fe(III) present within isotopically enriched ^{56}Fe goethite nanoparticles. To gain insights into the fate of Fe(II) on goethite as a function of particle size, complementary recovery studies were also performed in which particles reacted with Fe(II) were resuspended in dilute buffer solutions to examine whether any release of Fe(II) from the reacted particles was observed. Finally, to explore the role of goethite particle size in pollutant fate and transport, we compared the rate of reduction of nitrobenzene, a model groundwater contaminant, in suspensions with Fe(II) and different sizes of goethite.

An important consideration for this work was establishing the appropriate basis for comparing the reactivity of different particle sizes. As is most common for

investigations of nanoparticle behavior, size-dependent reactivity trends were developed using properties determined from characterization of dry goethite powders, namely values of specific surface area determined from BET adsorption isotherms and transmission electron microscopy (TEM) particle size analysis. Alternatively, because particle aggregation is inevitable in the near-neutral pH solutions used to investigate Fe(II) reaction with goethite, the contribution of aggregation to our observed size-dependent reactivity trend was also considered. The size and nature of aggregates in suspensions of different goethite particle sizes were estimated using a combination of techniques including dynamic light scattering, scanning electron microscopy (SEM) imaging of suspended particles, and sedimentation rates determined by monitoring changes in the visible light transmitted through each suspension as a function of time. Comparison of the size-dependent reactivity trend identified from batch studies to the results of dry particle and wet suspension characterization provided an opportunity to explore whether the properties of primary particles or particle aggregates dictate the macroscopic reactivity of goethite toward Fe(II) under environmentally relevant conditions.

Materials and Methods

Reagents

All reagents were used as received. The following chemicals were used during goethite synthesis: ferric nitrate nonahydrate ($Fe(NO_3)_3 \cdot 9H_2O$; Sigma Aldrich; ≥98%), sodium bicarbonate ($NaHCO_3$, Sigma Aldrich, ≥99.5%), and potassium hydroxide (KOH, Sigma Aldrich; ACS Reagent). Stock solutions of Fe(II) (~ 300 mM) were prepared by dissolving anhydrous ferrous chloride beads ($FeCl_2$, Sigma Aldrich, 99.99%) in 0.5 M HCl. Sorption experiments were conducted in buffer solutions of either 4-(2-hydroxyethyl)-1-piperazineethanesulfonic acid (HEPES; Sigma Aldrich, ≥99.5%) or piperazine-N,N'-bis(ethanesulfonic acid) (PIPES, Sigma Aldrich, ≥99%) with potassium

bromide (KBr; Fisher, ACS Reagent grade). All solutions in sorption and reactivity experiments were degassed prior to use by sparging with high purity N_2 for 1 h/L and were stored in an anaerobic chamber with an atmosphere of 95% N_2 and 5% H_2. Measurements of dissolved Fe(II) and total dissolved iron were performed with 1,10-phenanthroline (Sigma-Aldrich, ≥ 99%), hydroxylamine hydrochloride (Sigma Aldrich, 98%) and a buffer from ammonium acetate (Fisher, 98.5%) and glacial acetic acid (EMD, 99.7%).

Goethite Synthesis

Three primary particles sizes of goethite were synthesized. The largest particles, referred to as microrods, were synthesized according to Schwertmann and Cornell (*63*). Briefly, 180 mL of 5 M KOH was rapidly added to 100 mL of 1 M $Fe(NO_3)_3$. The mixture was diluted with distilled water to a final volume of 2 L and was then held in a closed polyethylene flask at 70 °C for 60 h. Goethite nanoparticles, referred to as nanorods, were synthesized according to a modified version of the method provided by Burleson and Penn for goethite synthesis from ferrihydrite (*64*), in which 1 L of 0.48 M $NaHCO_3$ solution was added dropwise (rate of approximately 4.5 mL/min) to an equal volume of 0.4 M $Fe(NO_3)_3$ that was being vigorously stirred. During this titration, the pH of the ferric nitrate solution increased from approximately 1.0 to 2.4. The resulting suspension was then microwaved to boiling, immediately cooled to ~ 20 °C using an ice bath, and purified via dialysis for three days according to the details provided in Anschutz and Penn (*45*). Conversion of the resulting ferrihydrite particles to goethite was accomplished by first raising the pH to 12 using 5 M KOH and then heating the resulting suspension at 90 °C for 24 h. In all instances, goethite particles were purified via three cycles of water washes and centrifugation. Particles were then freeze-dried, ground by mortar and pestle and passed through a 150 μm or 45 μm sieve for microrods and nanorods, respectively.

An intermediate size of goethite particle was synthesized by following a protocol adapted from that used for goethite nanoparticles. An 0.2 M ferric iron solution was prepared by dissolving iron metal (Fe(0); Aldrich, 99%) in 0.5 M HCl rather than using a ferric nitrate starting solution. After several days to allow for near complete dissolution of the iron metal, this solution was oxidized with excess 30% H_2O_2, and subsequently filtered to remove any undissolved iron metal. The pH of this ferric iron solution was first increased to 1.0 via the dropwise addition (rate of ~ 1 mL/min) of 5 M KOH, then an 0.24 M sodium bicarbonate solution was added at the same rate until a pH of 2.4 was attained. The resulting suspension was microwaved and purified via dialysis as described above. Then, 5 M KOH was used to raise the pH of the suspension to 13, followed by the baking, washing and drying steps described for nanorods and microrods.

As in our earlier work (*11, 12*), isotopically enriched goethite nanoparticles were synthesized from a starting material of isotopically enriched $^{56}Fe(0)$ to explore Fe(II)-Fe(III) electron transfer. Briefly, a solution of 50 mM Fe(III) was prepared by dissolving $^{56}Fe(0)$ in 0.5 M HCl as described previously for the synthesis of intermediate rods. As a result of the greater acidity and higher ionic strength of the resulting $^{56}Fe(III)$ solution relative to the ferric nitrate solution used during synthesis of istotopically normal nanorods, a modified procedure was required. First, a 5 M KOH solution was added in a dropwise manner to increase the pH of this solution to 1.9 (which was the pH of an equivalent ferric nitrate solution), followed by the dropwise addition of a 60 mM bicarbonate solution to achieve a final pH of 2.4. Following the method of Penn et al. (*65*), the ferric iron solution was immersed in an ice bath during the addition of these bases. The lower temperature controls the size of ferrihydrite particles generated during this hydrolysis step (*65*). Finally, rather than baking the final suspension in an oven at 90 °C for 24 h , we aged the suspension at room temperature for 1 week, during which time the suspension changed color from light brown to the brownish-orange color typical of

goethite. To ensure full conversion to goethite, the aged suspension was placed in an oven at 40 °C for 24 h prior to washing and freeze-drying as described above.

Characterization of Goethite Powders

Freeze-dried goethite particles were characterized via powder X-ray diffraction (XRD) using a Bruker D-5000 diffractometer with a Cu Kα source. Additional oxide characterization was performed using ^{57}Fe Mössbauer spectroscopy using the system described by Larese-Casanova and Scherer (*12*). The specific surface area of all powders was determined from seven-point N_2-BET adsorption isotherms performed on a Quantachrome Nova 1200 surface area analyzer. The size and morphology of primary goethite particles were determined using TEM. For TEM primary particle size analysis, suspensions (~ 0.2 g/L) of each particles size were prepared in methanol and sonicated for at least 1 h. A drop of this suspension was then applied to a carbon-coated Cu TEM grid (400 mesh; EMS). Images of goethite particles were collected on a JEOL JEM-1230 transmission electron microscope operated at a 100 keV accelerating voltage. Digital images were acquired using a Gatan UltraScan CCD camera with Gatan imaging software. The size of goethite particles was then determined by analyzing TEM images in the software package Image J.

Characterization of Aqueous Goethite Suspensions

Dynamic light scattering (DLS) was used to obtain information regarding the relative size of particles in nanorod and microrod suspensions. All DLS measurements were made with a Zeta Sizer S series from Malvern instruments operated at a laser wavelength of 532 nm. Suspensions for DLS analysis consisted of goethite concentrations ranging from 0.05 – 0.2 g/L, a pH of either 2 (0.01 N HCl) or 7.5 (25 mM HEPES buffer), and the ionic strength of all suspensions was adjusted to 25 mM with KBr. For pH 7.5 suspensions, independent experiments revealed that ionic strength had little influence on goethite aggregation for solutions with KBr concentrations as high as 1

M (data not shown). All solutions were passed through a 0.2 μm nylon syringe filter prior to addition of solid to minimize contamination from dust. All suspensions were prepared 24 h prior to DLS analysis and were not sonicated prior to light scattering measurements. For a typical analysis, 1 mL of a well-mixed suspension was delivered to a 1 cm pathlength cuvette, and the suspension was allowed to sit for approximately 30 seconds prior to analysis to allow any extremely large aggregates to settle out of solution.

Because DLS could only be performed on relatively dilute suspensions (< 0.2 g/L), qualitative insights regarding the size of particles in concentrated suspensions more representative of our sorption studies were obtained using UV/visible spectrophotometry to measure rates of particle sedimentation. This approach has previously been used to monitor to the stability and rates of aggregation in suspensions of zero-valent iron nanoparticles (*66, 67*). Goethite suspensions were added to a 1 cm pathlength cuvette and the change in transmitted light (λ = 510 nm) was monitored as a function of time. Suspensions were prepared as described for DLS analysis, with goethite concentrations ranging anywhere between 0.02 and 1 g/L. For this range of goethite concentrations, we observed a linear relationship between the absorbance values reported by the UV/visible spectrophotometer and the mass loading of goethite.

To complement DLS and sedimentation results, additional suspension characterization was accomplished using a Hitachi S-4800 SEM. Nanorod and microrod suspensions were prepared at pH 2 and pH 7.5 with loadings of 0.2 g/L, conditions identical to those used in DLS and sedimentation studies. A drop of suspension was applied to the SEM sample stub, and rather than allowing the solution to air dry, which likely would alter the aggregation state of the particles, the sample stub was immediately transferred to a -20°C freezer for 30 minutes. The sample stub was then placed in a freeze dry vessel to sublimate off the frozen solution. Because dried electrolyte and buffer would limit our ability to clearly image the particles in suspension, the freeze-dried

sample was washed with a few drops of deionized water, which was then removed from the sample by repeating the freezing and freeze-drying steps.

Fe(II) Sorption Experiments

All experiments investigating Fe(II) sorption on goethite were performed within an anoxic glove box. Unless otherwise noted, all experiments were conducted in the dark with well-mixed reactors containing 25 mM HEPES with 25 mM KBr at pH 7.5. Prior to the addition of goethite to the reactors, the buffer solution was allowed to equilibrate for at least 1 h after the addition of aqueous $FeCl_2$ solution. This solution was then passed through a 0.2 μm filter to remove any precipitates that may have accumulated from the initial spike of Fe(II), and the aqueous Fe(II) concentration was measured.

Experiments investigating the rate of Fe(II) sorption were conducted with a goethite loading of 4 g/L, an initial dissolved Fe(II) concentration of ~1 mM, and reactors were mixed end-over-end at a rate of ~10 rpm. Sorption isotherms for Fe(II) used a goethite loading of either 1 or 2 g/L and initial Fe(II) concentrations ranging from 0.1-5 mM. The extent of Fe(II) sorption as a function of pH was investigated in reactors with pH values ranging from 6.1-7.5. These experiments used a 25 mM PIPES buffer with 25 mM KBr, a goethite concentration of 1 g/L, and an initial Fe(II) concentration of ~1 mM. For isotherm and pH-edge experiments, reactors were mixed end-over-end at approximately 45 rpm and were allowed to equilibrate for at least 1 h, at which time the aqueous Fe(II) concentration was determined by filtering a portion of the oxide slurry. The loss of aqueous Fe(II) was determined by the difference between the concentration of Fe(II) prior to the addition of the oxide phase compared to the concentration after equilibration.

Additional studies examined the extent of Fe(II) sorption over the range of goethite loadings from 0.2-20 g/L at pH 7.5 in solutions of 25 mM HEPES with 25 mM KBr. In these reactor systems, the ratio of goethite mass loading to initial dissolved Fe(II)

concentration was held constant at a value of 0.25 mmole of Fe(II) per g of goethite. Accordingly, for goethite concentrations of 0.2, 2 and 20 g/L, initial dissolved Fe(II) concentrations of 0.05, 0.5 and 5 mM were used, respectively.

Reaction of ^{57}Fe(II) with ^{56}Fe Goethite

Experiments investigating Fe(II)-Fe(III) electron exchange followed the procedures listed above, but instead used isotopically enriched ^{56}Fe goethite particles and a $^{57}FeCl_2$ solution. Mössbauer spectroscopy was used to examine the products of the reaction between ^{57}Fe(II)(aq) and ^{56}Fe goethite. Reacted goethite particles were collected on 13 mm filter discs and mounted as a wet paste between two layers of Kapton tape for analysis. All measurements were made on the Mössbauer spectroscopy system described in Larese-Casanova and Scherer (*12*).

Fe(II) Recovery Experiments

We also examined whether the Fe(II)(aq) that had been reacted with goethite could be recovered. According to the procedures already described, goethite particles were reacted with a range of aqueous Fe(II) concentrations in suspensions containing 2 g/L goethite at pH 7.5 (25 mM HEPES with 25 mM KBr). After equilibration, the concentration of aqueous Fe(II) was measured, and the suspension was centrifuged. The supernatant was discarded, and the reacted particles were resuspended in a more dilute solution of Fe(II)(aq) and transferred to a new glass vial. These new reactors were allowed to equilibrate for approximately 1 h, at which time the solution phase concentration of Fe(II) was measured.

Nitrobenzene Reduction Experiments

The reduction of nitrobenzene was examined in goethite suspensions containing Fe(II). Reactions were conducted at pH 7.5 (25 mM HEPES with 25 mM KBr) and contained an initial nitrobenzene concentration of approximately 100 μM, an initial

aqueous Fe(II) concentration of 1 mM and 0.25 g/L goethite. Nitrobenzene was added as a methanolic spike to a suspension of goethite that had been equilibrated with Fe(II) according to the methods used in sorption experiments. Samples of the goethite slurry were periodically removed from the reactor, passed through a 0.2 μm PTFE syringe filter to quench the reaction and transferred to a crimp-sealed autosampler vial for HPLC analysis.

Chemical Analyses

Dissolved Fe(II) concentrations were measured colorimetrically with the 1,10-phenanthroline method at 510 nm on a UV/visible spectrophotometer according to the procedure detailed by Larese-Casanova and Scherer (*12*). Analysis of nitrobenzene and its reduction products were performed via HPLC. Details regarding the system and conditions used for nitrobenzene analysis can be found elsewhere (*11*).

Results

Primary Particle Characterization

We have adopted a nomenclature for goethite particles similar to that introduced by Anschutz and Penn (*45*), and refer to the different particle sizes as nanorods, intermediate rods and microrods. Properties determined from the characterization of freeze-dried powders of each synthetic goethite are summarized in Table 2.1, whereas TEM images showing the acicular, or rod-like, morphology of each primary particle size are shown in Figure 2.1. For TEM analysis, particles indicative of other iron oxide phases were not observed, suggesting near-complete transformation of ferrihydrite to goethite during the aging step of all synthetic procedures.

XRD patterns were consistent with goethite, and the pattern for nanorods revealed considerable line broadening, which was anticipated due to the lower degree of crystallinity resulting from their nanoscale dimensions. For all samples, ^{57}Fe Mössbauer

spectra and the corresponding model fits were also consistent with those anticipated for goethite (see electronic annex Figure A1). Our Mössbauer detection limit determined from mixtures of ferrihydrite and goethite was approximately 3% ferrihydrite by mass, which provides an upper limit as to how much ferrihyrite might be present. Notably, Mössbauer spectra collected at 298 (room temperature), 250 and 140 K revealed less magnetic ordering in nanorods relative to microrods, behavior that is often attributable to smaller particles (*68, 69*). Differences in magnetic ordering observed from the Mössbauer characterization of these particles were subtle, however, and by 77 K, both the nanorods and microrods had achieved full magnetic ordering.

The distribution of nanorod dimensions was determined from TEM analysis of 530 unagreggated particles (Figure 2.2). On average, nanorods were 80 nm long and 7 nm wide, slightly larger than the nanorods prepared by Anshutz and Penn (*45*) using the same synthesis procedure. Size distributions for the intermediate rods and microrods were determined from smaller sample sizes (n = 240 and 285, respectively). This was due in part to the greater tendency of these particles to exist as dense aggregates when dispersed and dried on TEM grids, and sonication of these suspensions prior to imaging failed to improve their dispersion. Microrods were roughly 670 nm in length and 25 nm in width, but exhibited a much broader size distribution, as indicated by the rather large standard deviations associated with their dimensions. The size distribution for the intermediate rods, which were approximately 330 nm long and 14 nm wide, was also relatively broad. In fact, there is a relatively large overlap for the particle size distributions of intermediate rods and microrods.

Nanorods exhibited the highest specific surface area of 110 (± 7) m^2/g, as determined from seven-point N_2-BET adsorption measurements performed in triplicate (uncertainty represents one standard deviation). Specific surface areas for the intermediate rods (55 m^2/g) and microrods (40 ± 3 m^2/g) were smaller by roughly a factor of 2 and 3, respectively. Goethite specific surface areas were also approximated from the

average rod dimensions in Table 2.1 using the approach of Anschutz and Penn (*45*), who modeled goethite rods as rhomboidal prisms bounded by (*70*). These values, assuming a goethite density of 4.26 g/cm^3 (*24*), are also included in Table 2.1, and the relationship between particle dimensions (length and width) and specific surface area calculated assuming this geometry is displayed in Figure A2. Although some variation exists between specific surface areas determined from BET measurements and those estimated from particle geometry, the trend of increasing specific surface area with decreasing particle size holds true for both sets of values.

Isotopically enriched ^{56}Fe nanorods were nearly identical to nanorods prepared from isotopically normal iron starting materials. A TEM image of these particles is shown in Figure A3, which reveals that these primary particles had a greater tendency to adhere to one another relative to isotopically normal nanorods. The X-ray diffraction pattern for ^{56}Fe nanorods was consistent with goethite and revealed the expected line broadening. Furthermore, their specific surface area and size distribution were similar to those obtained for the nanorods synthesized from isotopically normal materials (Table 2.1).

Characterization of Goethite Suspensions

Visual inspection suggested that all sizes of goethite extensively aggregated in pH 7.5 suspensions, as large aggregates settled out of solution if the suspensions were not mixed. Figure 2.3 illustrates the role of solids concentration on aggregate settling rates at pH 7.5. Rather than plotting transmitted light as a function of time, we report normalized absorbance measurements (A/A_0), assuming that absorbances measured by the UV/visible spectrophotometer account primarily for scattered light. We reiterate that suspensions were prepared 24 h prior to conducting sedimentation measurements and were not sonicated prior to the experiment. Thus, rates of sedimentation shown in Figure 2.3 reflect the aggregates in our suspensions at what we assume to be steady state.

The initial change (for $t \leq 10$ min) in normalized absorbance over time adhered to exponential decay, allowing initial rate coefficients for settling to be determined from semilog plots of normalized absorbance versus time. Initial rate constants were comparable in nanorod and microrod suspensions, ranging from approximately 0.03 – 0.05 min^{-1} for nanorods and from 0.02-0.04 min^{-1} for microrods over the solid loadings investigated. Over time, the rate of aggregate settling slowed in all suspensions, and normalized absorbance values approached a stable value after roughly two hours. This behavior is most clearly observed for the 0.02 g/L suspensions of microrods and nanorods, which indicates that some fraction of the suspended particles either do not settle out of solution or do so at a very slow rate. At these longer timescales, higher goethite concentrations resulted in lower values of A/A_0, consistent with a greater extent of particle settling with increasing solids loading. Also note that over the entire experimental duration, values of A/A_0 were greater in microrod suspensions than the values observed in the corresponding nanorod suspensions.

Intensity-weighted size distributions determined from DLS analysis of pH 2.0 and pH 7.5 goethite suspensions are shown in Figure 2.4. For pH 2.0 suspensions, nanorod and microrod size distributions are presented for solids concentrations of 0.01 g/L and a 0.2 g/L because these distributions are representative of all solid loadings analyzed over this range. Generally, no systematic trend in size distribution with increasing solid loading was observed for either particle size. In all, thirteen different analyses were conducted with nanorod suspensions at pH 2, and the mean hydrodynamic diameter from these distributions was determined to be 130 (± 20) nm. Similarly, eight different analysis were conducted with microrod suspensions at pH 2, yielding an average hydrodynamic diameter of 550 (± 160) nm.

We also present in Figure 2.4 intensity weighted sized distributions for suspensions at pH 7.5. Shown are replicate measurements performed on a 0.2 g/L suspension of each particle size. Nanorod suspensions were analyzed in quadruplicate

and produced an average hydrodynamic diameter 1600 (± 600) nm, which is nearly an order of magnitude greater than the hydrodynamic diameter determined at pH 2.0. A comparable hydrodynamic diameter of 1500 (± 200) nm was determined from triplicate analysis of a microrod suspension at pH 7.5. In fact, as is observed in Figure 2.4, the size distributions measured at pH 7.5 for the microrod suspension essentially overlapped with the distributions measured for nanorods.

Representative SEM images of the particles in 0.2 g/L nanorod and microrod suspensions at pH 2 and 7.5 are shown in Figure 2.5. For nanorods, SEM images revealed that pH 2 suspensions consisted primarily of well-dispersed or loosely packed individual nanorods, although aggregates typically less than 1 μm in diameter were occasionally observed. At pH 7.5, on the other hand, images revealed a predominance of relatively large and dense aggregates that were typically on the order of a few microns, but sometimes as large as 30 μm. The dense nature of these nanorod aggregates is shown in the inset in Figure 2.5, which is a high magnification image of the surface of a nanorod aggregate.

Similar observations were made for microrod suspensions at pH 2 and 7.5. At pH 2, a number of well-dispersed or loosely associated microrods were clearly observed, whereas aggregates were rarely found. In contrast, larger aggregates were frequently encountered at pH 7.5, typically ranging between 5-10 μm, although aggregates with diameters up to 30 μm were sometimes observed. Notably, SEM images of pH 7.5 suspensions suggest that there are a greater number of individually dispersed microrods relative to freely dispersed nanorods.

Recall that sedimentation studies indicated that a fraction of the particles in suspensions at pH 7.5 either did not settle or did so at a very slow rate. SEM images of suspensions taken after 30 min of settling reveal that the relatively stable particles consist primarily of small aggregates ranging from 0.5 -1 μm in nanorod systems, whereas in

microrods systems, a mixture of individually dispersed microrods and small aggregates typically on the order of a couple of microns was observed (see Figure A4).

Fe(II) Sorption on Goethite

Fe(II) sorption isotherms collected for pH 7.5 suspensions of each goethite particle size are shown in Figure 2.6. Independent experiments (Figure 2.7) revealed that the density of sorbed Fe(II) in both nanorod and microrod suspensions was comparable over a much broader range of mass loadings than those used to construct the sorption isotherms presented in Figure 2.6.

Sorption isotherms for Fe(II) revealed relatively small differences in the concentrations of sorbed Fe(II) per gram of goethite determined for each particle size. Whereas sorption data for intermediate rods and microrods were essentially identical, sorbed concentrations of Fe(II) on the nanorods were slightly greater than the values measured with larger particles. This result is most easily observed from the Fe(II) sorption densities reported in Figure 2.7, in which densities measured for nanorods were on average 1.3 (± 0.1) times greater than the values measured in the corresponding microrod system. Figures 2.6 and 2.7 also reveal, however, that the increase in Fe(II) uptake on nanorods was often within the uncertainty associated with measurements of sorbed Fe(II) concentration, which was determined from replicate experiments.

Additional experiments examined whether the rate of Fe(II) sorption (Figure A5) or the extent of Fe(II) sorption as a function of pH (Figure A5) exhibited more pronounced variations between nanorod and microrod systems containing equivalent goethite mass. Consistent with the results of our Fe(II) isotherms, only a modest increase in the rate and extent of Fe(II) sorption was observed for nanorods relative to the behavior observed in otherwise identical microrod suspensions.

Fe(II)-Fe(III) Interfacial Electron Transfer on Goethite

Temperature profiles of Mössbauer spectra collected after the reaction of 0.25 mM aqueous ^{57}Fe(II) with suspensions containing 2 g/L of either ^{56}Fe goethite nanorods or microrods are shown in Figure 2.8. For both nanorods and microrods, these conditions produced an equivalent concentration of 0.11 mmoles of sorbed ^{57}Fe per gram of ^{56}Fe goethite. The resulting temperature profiles for ^{56}Fe nanorods and ^{56}Fe microrods reacted with ^{57}Fe(II)(aq) revealed nearly identical ferric iron sextets, suggesting that electron transfer had occurred between sorbed ^{57}Fe(II) and structural ^{56}Fe(III) present within the goethite. As in our earlier study with ^{56}Fe microrods (*11*), model fit parameters for the 13 K spectra suggested that these sextets correspond to goethite with a low degree of magnetic ordering.

As confirmation that the aqueous ^{57}Fe(II) was oxidized by structural ^{56}Fe(III) in the nanorods and not by trace oxidants in our system, we dissolved the reacted goethite nanoparticles in ~ 3 M HCl and subsequently measured the dissolved Fe(II) concentration. To account for the background signal of Fe(III) generated from goethite dissolution, we subtracted the absorbance measured in samples of dissolved goethite without Fe(II). This procedure typically resulted in near complete (95-100%) recovery of the sorbed Fe(II), providing further evidence that the Mössbauer spectra in Figure 2.8 reflect oxidation of the sorbed Fe(II) by goethite.

Recovery of Fe(II) after Reaction with Goethite Nanorods and Microrods

The results of recovery experiments used to explore the fate of the Fe(II) species generated from interfacial electron exchange are shown in Figure 2.9. Open symbols correspond to the sorbed and aqueous Fe(II) concentrations measured after fresh goethite particles were equilibrated with aqueous solutions containing variable concentrations of Fe(II). Solid symbols indicate the concentrations of sorbed and aqueous Fe(II)

determined after these reacted particles were recovered via centrifugation, resuspended and equilibrated with a new, more dilute Fe(II) solution. We observed relatively good agreement between Fe(II) concentration data collected from sorption and recovery experiments, suggesting that most of the Fe(II) species generated via interfacial electron transfer was released back into solution upon dilution. Our ability to recover Fe(II) was independent of the size of goethite particles used in sorption and recovery experiments.

Nitrobenzene Reduction by Fe(II) in the Presence of Goethite

Under our experimental conditions (0.25 g/L goethite, pH 7.5, 1 mM initial dissolved Fe(II) concentration), roughly 15-20% of the initial aqueous Fe(II) concentration was sorbed in the nanorod and microrod suspensions. In both systems, nitrobenzene was rapidly reduced, and the end product of the reaction was aniline. Near complete transformation of nitrobenzene was observed over the course of 1 h.

For both sizes of goethite particles, the concentration profile for nitrobenzene as a function of time generally followed exponential decay, although a moderately steep (and reproducible) decrease in the concentration of nitrobenzene was observed by the first sampling point (t ~ 1 min) in nanorod systems. Pseudo-first-order rate constants for the reduction of nitrobenzene (k_{obs} values) were determined from plots of the natural log of nitrobenzene concentration versus time (Figure 2.10) and equaled $(2.6 \pm 0.4) \times 10^3$ s^{-1} and $(1.8 \pm 0.1) \times 10^3$ s^{-1} for nanorods and microrods, respectively. Values of k_{obs} indicate only a modest increase in the rate of nitrobenzene reduction in nanorod systems on the basis of goethite mass loading. Moreover, as the experimental conditions chosen for these experiments resulted in a comparable amount of sorbed Fe(II) in both nanorod and microrod suspensions, little change in their relative reactivity was observed when k_{obs} values were normalized by the concentration of sorbed Fe(II).

Discussion

Aggregation of Suspended Goethite Particles

Goethite nanorods and microrods aggregate in pH 7.5 suspensions. Aggregate formation is clearly shown in SEM images (Figure 2.5), with additional evidence from sedimentation studies and DLS analysis. The mean hydrodynamic diameter estimated for particles in nanorod suspensions at pH 7.5 was roughly one order of magnitude greater than the corresponding value measured at pH 2. Although the magnitude of increase was not as great in microrod suspensions, the average hydrodynamic diameter at pH 7.5 was still greater than that observed at pH 2. Such results illustrate the control that solution pH exerts on the stability of goethite suspensions.

A dominant role for pH in suspension stability is anticipated from DLVO theory (*71*), which is widely applied to explain aggregation in colloidal suspensions. At low pH values (e.g., pH 2.0), protonation of surface hydroxyl groups produces a net positive surface charge that, due to unfavorable electrostatic interactions, minimizes aggregation. As a result, the mean hydrodynamic diameter measured at pH 2.0 for nanorods (~ 130 nm) agrees reasonably well with the nanorod dimensions determined from characterization of dry goethite powders (80 × 7 nm), especially since we did not use any algorithms to correct for the acicular nature of our particles In contrast, pH 7.5 is nearer to the pH at which the net surface charge on goethite is zero (reported range of pH_{zpc} 7.5-9.5; (*24*), a condition that increases particle-particle interactions and results in aggregate formation.

Results from DLS analysis and sedimentation studies also appear to suggest that the aggregates in nanorod and microrod suspensions at pH 7.5 are of comparable size. Specifically, mean hydrodynamic diameters in both systems were on the order of 1 micron at pH 7.5. Furthermore, the comparable rates of nanorod and microrod settling could also be interpreted as evidence that similarly sized aggregates were present in both

systems. Unfortunately, both approaches have limitations; sedimentation velocities are influenced by a variety of factors including the permeability and density of the aggregates (*72*), which were not rigorously quantified for our experimental systems, whereas DLS analysis requires suspensions with non-settling particles moving entirely as a result of Brownian motion (*73*). Although our application of DLS to pH 2 goethite suspensions meets this requirement (sedimentation plots show that both suspensions are essentially stable at pH 2, see Figure A6), our unstable pH 7.5 suspensions likely pushed this approach to its analytical limits.

The most definitive evidence as to the relative size and nature of the particles in suspension at pH 7.5 is provided by the images from SEM (see Figure 2.5). These images support a scenario in which aggregates of nanorods are of comparable size to the aggregates encountered in microrod suspensions, as aggregates generally on the order of 5-10 μm are found in both systems. There are also a fewer number of primary particles dispersed in nanorod suspensions, and the nanorod aggregates appear to be much denser. It seems, therefore, that nanorods aggregate more extensively than microrods at pH 7.5, resulting in denser aggregates and fewer primary particles suspended in solution.

Influence of Goethite Particle Size on Fe(II) Sorption and Contaminant Reduction

Little difference with regards to Fe(II) sorption and contaminant reduction was observed over the range of primary particle sizes used in our study. On the basis of mass, Fe(II) sorption isotherms and rates of nitrobenzene reduction appear nearly independent of goethite particle size. Thus, the significant enhancements in rates or extent of reaction that we had originally hypothesized were not observed. The lack of significant increases in reactivity contrasts several previous reports in which nanoparticles generally outperform larger particles on a mass basis (e.g., see review by Savage and Diallo (*74*) and references therein).

For investigations of nanoparticle reactivity, the influence of particle size is traditionally determined by normalizing measures of reactivity (e.g., sorbate concentrations or reaction rate constants) to a primary particle characteristic determined from the characterization of dry nanoparticles. The most widely used property is specific surface area, which is often assumed to be representative, or at least a good indicator, of reactive surface area. Nanoscale size-effects are then identified by determining whether nanoparticles display enhanced reactivity beyond that expected from their greater surface area.

In Figure 2.11, we plot our Fe(II) sorption isotherms normalized to BET surface area. A clear trend emerges that implies that the amount of Fe(II) sorbed per m^2 of goethite decreases with decreasing particle size. A similar trend is observed if we normalize our rate constants for nitrobenzene reduction by BET surface area, which yields surface-area-normalized rate constants (or k_{SA} values) of 2.3 ($\pm$ 0.4) $\times 10^6$ and 4.4 ($\pm$ 0.3) $\times 10^6$ $L \cdot m^2 \cdot s^{-1}$ for nanorods and microrods, respectively. The lower observed reactivity of the nanorods is not limited to specific surface areas derived from BET measurements, as the use of specific surface areas estimated from particle geometries obtained with TEM (Table 2.1) produced the same trend.

That smaller k_{SA} values and less Fe(II) sorbed per m^2 are observed for nanorods again runs counter to the typical trends commonly associated with nanoparticles. Both reactivity and sorption capacity per unit surface area are often expected to increase as particle sizes approach the nanoscale. Indeed, there are many examples of where significant increases in reactivity of nanoparticles have been observed. Sorption studies by Zhang et al. (*75*) reported as much as a 70-fold increase in the sorption coefficients of simple organic acids on 6 nm TiO_2 particles relative to 16 nm TiO_2 material, and a more recent study by Mayo et al. (*76*) reported enhanced uptake of arsenic on 12 nm magnetite nanoparticles relative to larger particles that could not be attributed to differences in surface area. With respect to reaction rates, larger k_{SA} values have been observed for the

reduction of carbon tetrachloride by 9 nm magnetite particles compared to values measured with 80 nm particles (*53*), and surface-area normalized rates of hematite (*23*) and goethite (*45*) reductive dissolution have also been shown to increase with decreasing particle size.

There are, however, a few others that have also observed less reactivity with smaller particles on the basis of surface area. Most notable for comparison to this work are two studies which investigated the size-dependent sorption of Hg(II), protons, and carbonate on goethite. For Hg(II) sorption, Waychunas et al. (*42*) observed a similar size dependence on the basis of goethite surface area for particles ranging from 5 to 75 nm that were prepared via nearly the same synthetic methods used here. Likewise, Villalobos et al. (*77*) also measured less proton and carbonate sorption per m^2 on goethite rods with specific surface areas (45 and 94 m^2/g) that were quite close to our microrods and nanorods.

The lesser reactivity of the goethite nanoparticles in these prior studies was attributed to different phenomena. In the proton and carbonate sorption study, the lesser reactivity was interpreted as evidence that the density of reactive goethite sites (i.e., sites per m^2) decreases as particle size becomes smaller. In the Hg(II) study, on the other hand, the size-dependent reactivity trend was attributed to increased curvature of nanoparticle surfaces resulting in distorted $Fe(III)(O,OH)_6$ octahedra and thus a poorer coordination environment for metal surface complexation. Their hypothesis of distorted octahedra was supported by EXAFS measurements that revealed a ~0.2 Å increase in the Hg-Fe interatomic distance for the smallest (highest specific surface area) goethite particles relative to the largest (smallest specific surface area) goethite particles studied. Additional explanations for the lesser reactivity of the smaller particles may also be related to differences in the manner charge accumulates on nanoparticle surfaces (*78*) or to the relative amounts of specific crystal faces available on nanorods in comparison to microrods (*79*).

Influence of Aggregation on Fe(II) Sorption and Reactivity

An alternative explanation for the lesser reactivity of the nanorods we observed here is loss of reactive surface area due to aggregation. Based upon SEM images, DLS analysis, and sedimentation studies, we can reasonably conclude that goethite nanorods and microrods both aggregate at pH 7.5, which introduces uncertainty as to whether macroscopic observations of material reactivity reflect the behavior of the aggregate or the nanoparticles comprising the aggregate (*52*). The size-dependent behavior suggested from the surface-area normalized isotherms in Figure 2.11 could, therefore, simply be an artifact resulting from the inappropriate use of primary particle surface area for normalization.

Aggregation may also influence the results of studies exploring interfacial Fe(II)-Fe(III) electron exchange in nanorod and microrod suspensions. From Mössbauer spectroscopy and the results of our Fe(II) recovery experiments, we found that the products of electron exchange are of a nearly identical nature for each particle size and that the Fe(II) species generated via this process displays comparable behavior upon resuspension of each particle size after reaction. Both observations were unexpected; we initially anticipated the surface coating on less ordered nanorods to be more poorly ordered than the microrod coating, and previously, we found that the Fe(II) created after Fe(II)-Fe(III) electron transfer on hematite could not be recovered (*12*). Furthermore, Mulvaney et al. (*62*) provided experimental evidence that the fate of Fe(II) generated by the reduction of iron oxides depends upon particle size, with larger particles having a greater tendency for charge migration into the bulk of the oxide where the Fe(II) could not be recovered via chemical extraction. We saw no evidence to support such a scenario, as our recovery studies illustrate that the Fe(II) generated from goethite reduction is equally susceptible to recovery from both particle sizes. We suspect such similarities are also a consequence of the extensive aggregation occurring in nanorod suspensions,

ultimately producing particles that are typically within the range of particle sizes encountered in microrod suspensions.

Although the implications of aggregation on the environmental transport of nanoparticles are well-recognized (*47*), its impact on reactivity in environmentally relevant systems has not been widely considered in previous investigations. Often times, a response in particle reactivity to variations in ionic strength, which will affect suspension stability, is used to infer a role for aggregation in altering the reactivity of colloidal or nanoparticle suspensions (*53, 55*). Another approach was employed by Amonette et al. (*54*), who interpreted a systematic decrease in the amount of sorbed Fe(II) per gram of goethite with increasing goethite loading as a result of aggregation in their microrod suspensions. Recall, however, that this behavior was not observed in the current study, as the amount of Fe(II) sorbed per gram of goethite was relatively constant in both microrod and nanorod systems for goethite concentrations ranging from 0.02 to 20 g/L (Figure 2.7), which may indicate that the size of aggregates does not change appreciably over the range of goethite concentrations employed in Fe(II) batch sorption studies.

Conclusions

Results from both batch and spectroscopic investigations revealed little difference in the reactivity of goethite nanorods and microrods with regard to Fe(II) sorption, Fe(II)-Fe(III) interfacial electron transfer, and nitrobenzene reduction on a mass-normalized basis. SEM images, DLS analysis, and sedimentation studies all indicate that aggregation occurs in near-neutral pH suspensions of goethite nanorods and microrods. Taken together, these findings illustrate the challenges frequently encountered when evaluating whether nanoparticles display size-dependent reactivity in environmentally relevant systems. Specifically, it is difficult to quantify reactive surface area in aggregating

systems, particularly when different primary particle sizes display different aggregation behavior.

Based upon SEM images, DLS analysis, and sedimentation studies, we contend that the amount of reactive surface area in our goethite suspensions is unknown. Clearly, the extensive aggregation we observed indicates that the reactive surface area is less than what would be predicted from our BET measurements, but exactly how much less is difficult to assess. Consequently, presenting our experimental results as evidence that nanorods are inherently less reactive toward Fe(II) uptake and nitrobenzene reduction than larger particles on the basis of primary particle specific surface area is suspect. In fact, the nearly equivalent reactivity observed for nanorod and microrod systems on the basis of particle mass could be interpreted as evidence that the reactive surface area is roughly equivalent in the pH 7.5 suspensions that consist primarily of aggregates of each particle size.

Many previous studies have fit macroscopic sorption data similar to the data we collected here and concluded that differences in amount of sorption were due to either differences in surface site density or intrinsic reactivities. For example, the distorted surface octahedra on nanoscale goethite particles observed by Waychunas et al. (*42*) could be interpreted to produce a lower intrinsic reactivity of the nanorod surface, whereas the observation of less proton and carbonate uptake on goethite nanoparticles was modeled by invoking a decrease in surface site density with decreasing particle size (*77*). Both represent viable explanations for the depressed reactivity of goethite nanorods with respect to Fe(II) sorption that we have observed here on the basis of primary particle surface area. In fact, our Fe(II) sorption results are remarkably consistent with the findings of Villalobos et al. (*77*), as their site densities of 8.6 μmoles/m^2 on goethite particles similar to our microrods (SA_{BET} = 45 m^2/g) and 3.0 μmoles/m^2 for particles comparable to our nanorods (SA_{BET} = 94 m^2/g) correspond reasonably well our isotherm data (as illustrated by the dashed lines in Figure 2.11).

Such conclusions regarding surface site density and intrinsic reactivity, however, are based on the assumption that the dry particle surface area is the same as the reactive surface area in a wet suspension. We argue, and demonstrate, that when that assumption is no longer valid (i.e., in an aggregated suspension), it is no longer possible to isolate whether the differences in sorption are due to differences in *i*) intrinsic reactivity of a site, *ii*) site densities, or *iii*) changes in available surface area. With this data set, we show that the exercise of fitting sorption isotherms to determine site densities or intrinsic reactivities when particles aggregate is not appropriate. The "reactive" surface area has changed due to aggregation, and with this number unknown, the fitted isotherm parameters are no longer meaningful. We emphasize, as have others before us (e.g., Nurmi et al. (2005)), that the role of aggregation must be considered when attempting to evaluate nanoscale effects based upon the behavior and reactivity of particle suspensions.

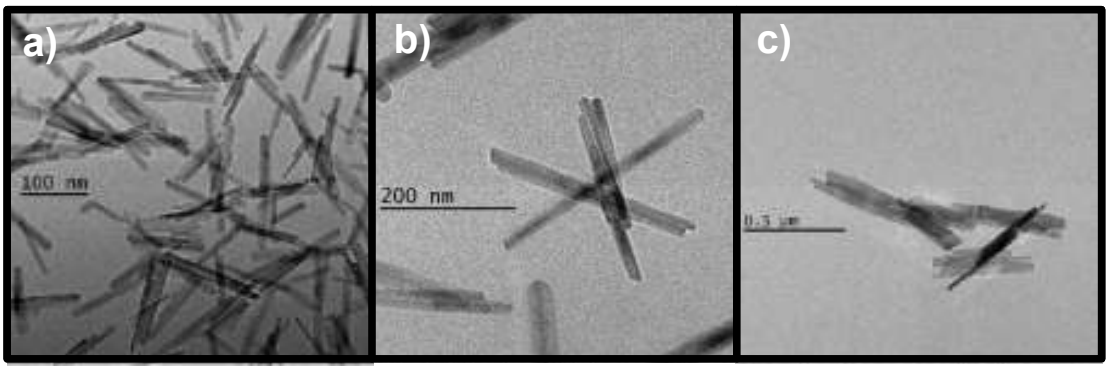

Figure 2.1 TEM images of the three goethite primary particle sizes synthesized in the current study. Shown are goethite (a) nanorods, (b) intermediate rods and (c) microrods. The dimensions and surface area of these materials are summarized in Table 1.

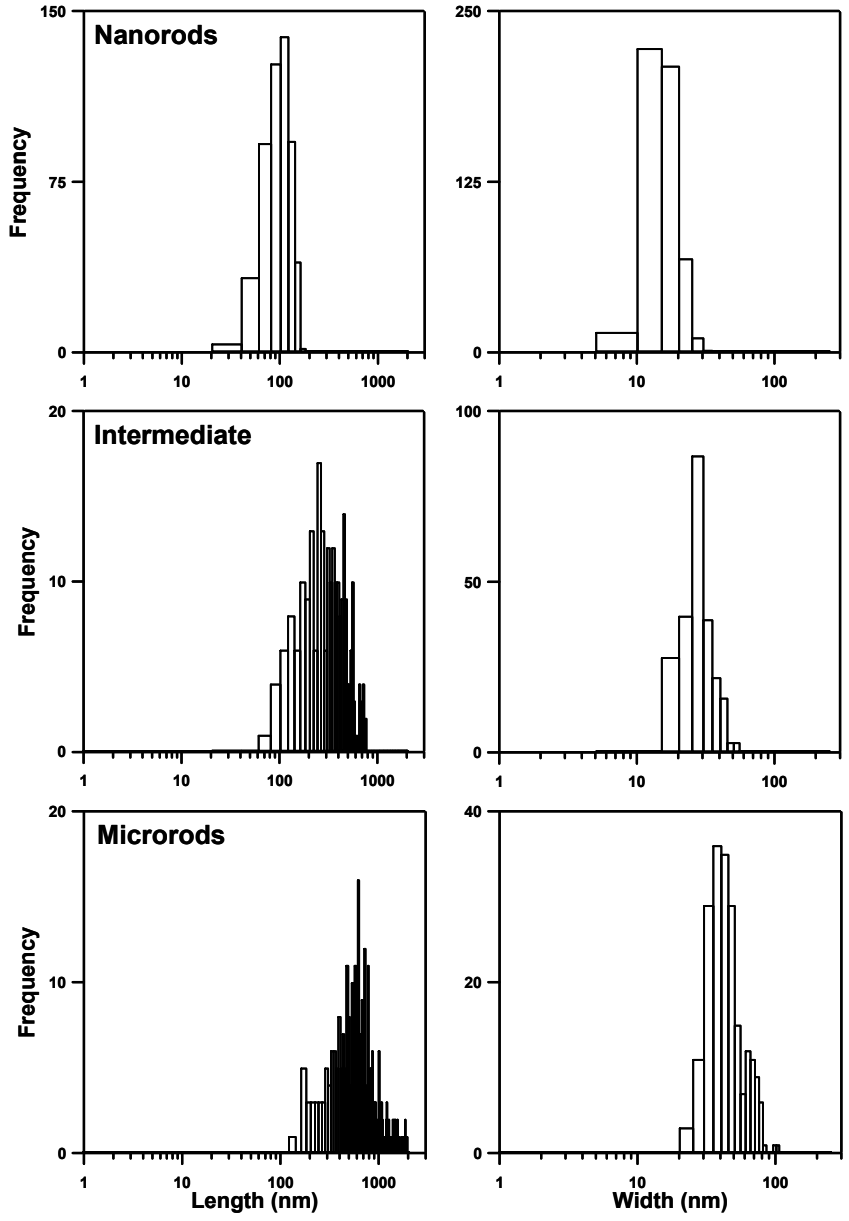

Figure 2.2 Size distributions for nanorods, intermediate rods and microrods determined from TEM analysis of unaggregated goethite primary particles. Values are shown on a logarithmic scale with equivalent bin sizes so that the distributions of each primary particle size can be directly compared.

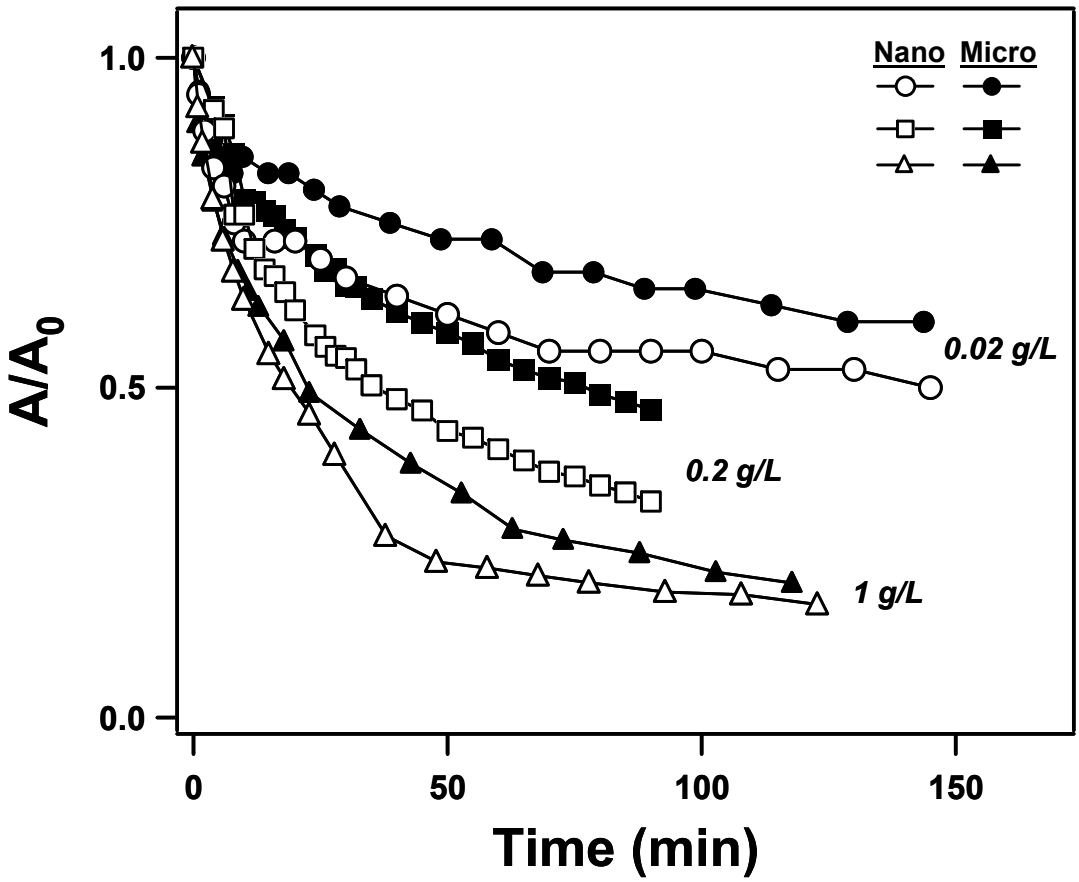

Figure 2.3 Sedimentation plots for nanorods and microrods shown as a function of mass loading at pH 7.5. Particles were suspended in 25 mM HEPES buffer with 25 mM KBr, conditions to equivalent to those used in Fe(II) sorption studies. Normalized absorbance values correspond to the amount of light (λ = 510 nm) transmitted through a 1 cm path length cell containing goethite suspensions.

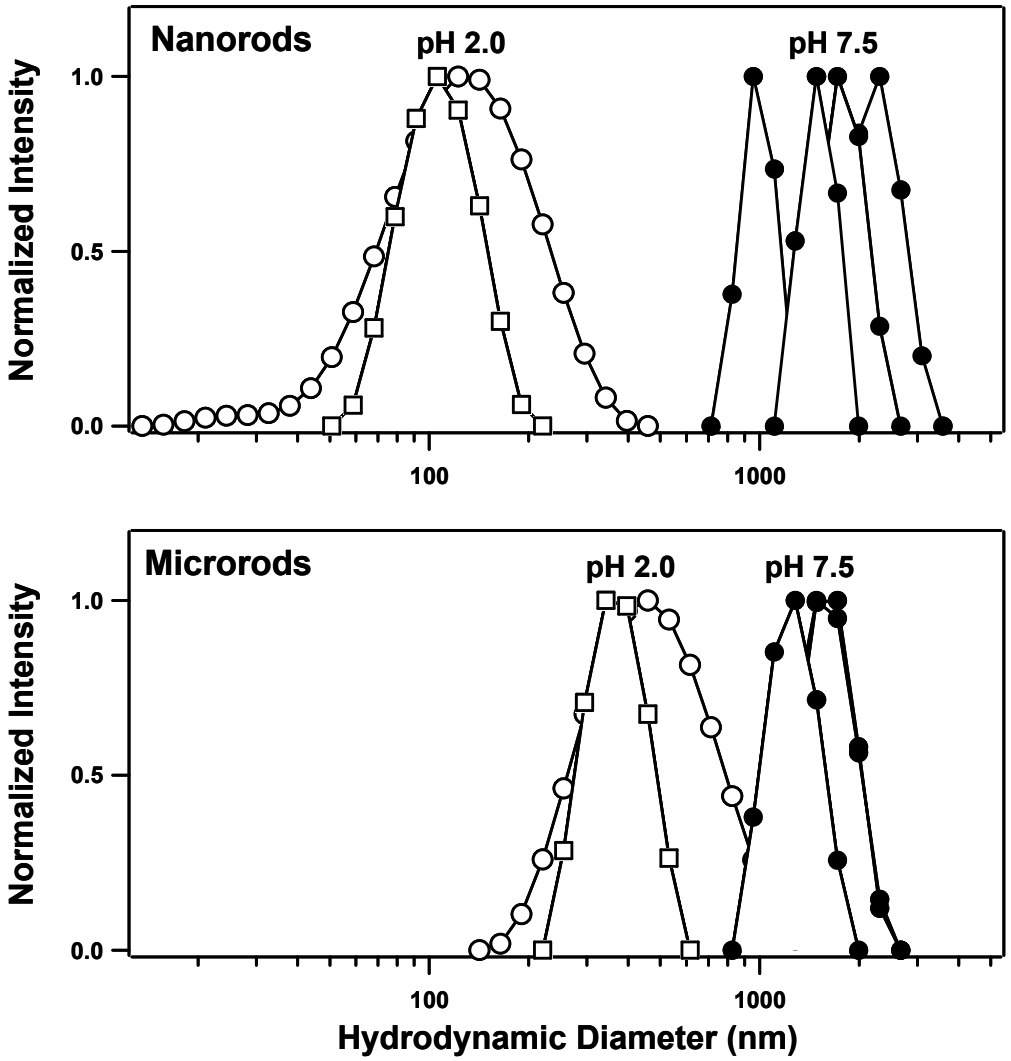

Figure 2.4 Intensity-weighted size distributions for nanorod and microrod suspensions determined from dynamic light scattering. Data at pH 2.0 (0.01 N HCl) represent size distributions for 0.01 (open squares) and 0.2 g/L (open circles) suspensions, whereas data at pH 7.5 (25 mM HEPES) are replicate measurements performed on a single 0.2 g/L suspension of each material. The ionic strength of all systems was adjusted to 25 mM with KBr.

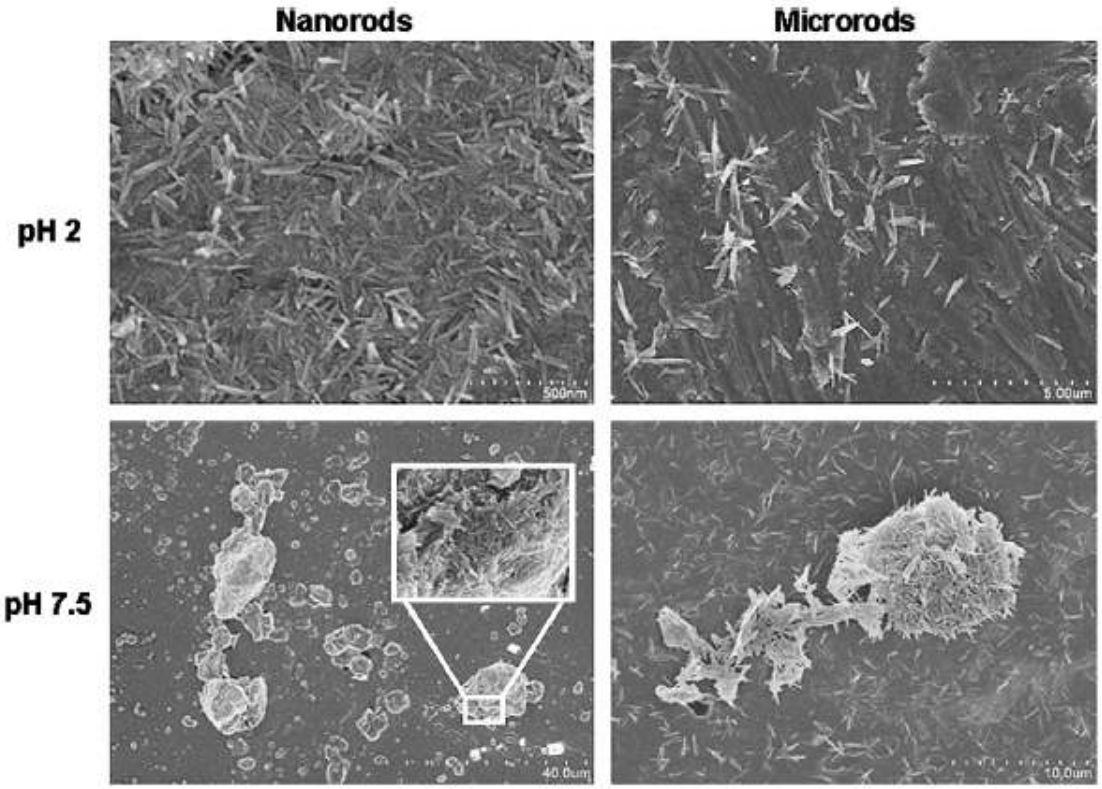

Figure 2.5 SEM images of nanorod and microrod suspensions at pH 2 and pH 7.5. Inset for nanorods at pH 7.5 reveals the dense nature of aggregates in these suspensions.

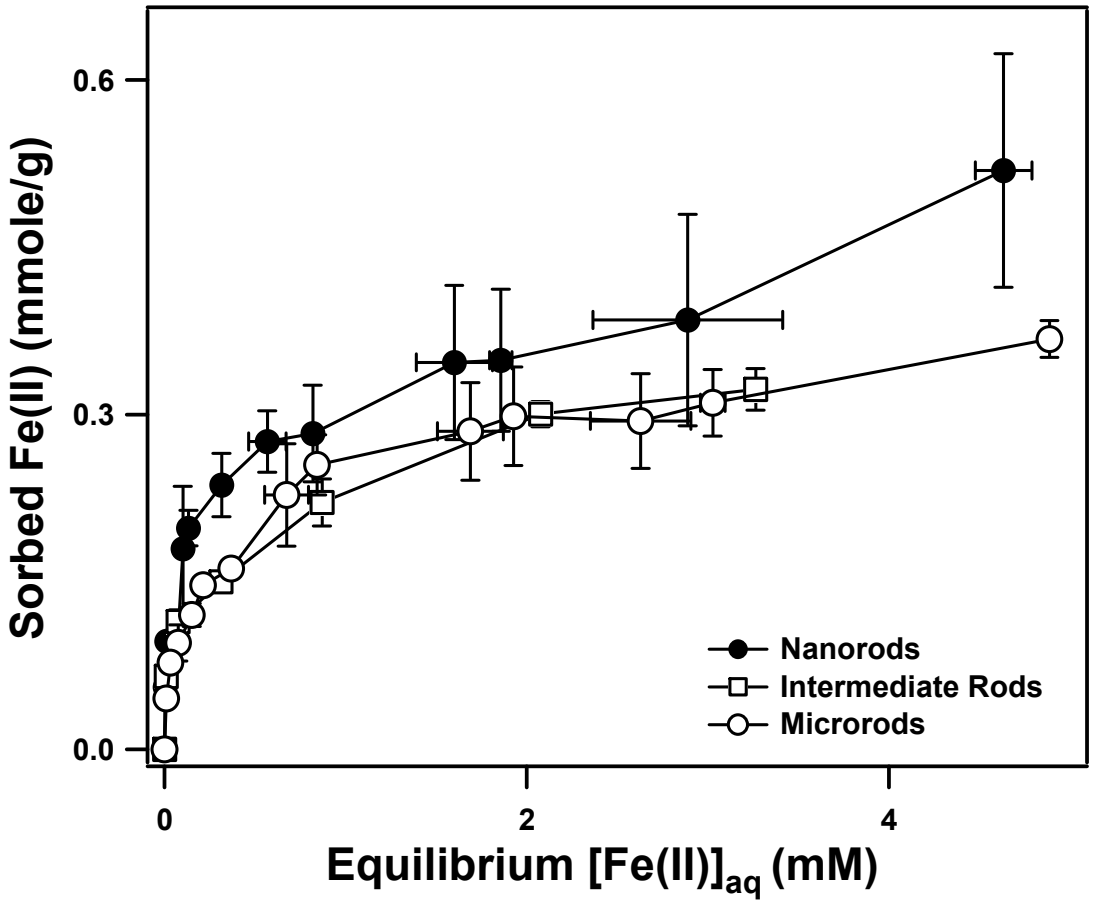

Figure 2.6 Fe(II) sorption isotherms for goethite suspensions of different particle sizes. Isotherms were conducted at pH 7.5 in 25 mM HEPES buffer with 25 mM KBr, using either 1 or 2 g/L goethite (15 or 30 mg into 15 mL). Uncertainties represent one standard deviation determined from replicate experiments, where *n* ranged between 3 and 21.

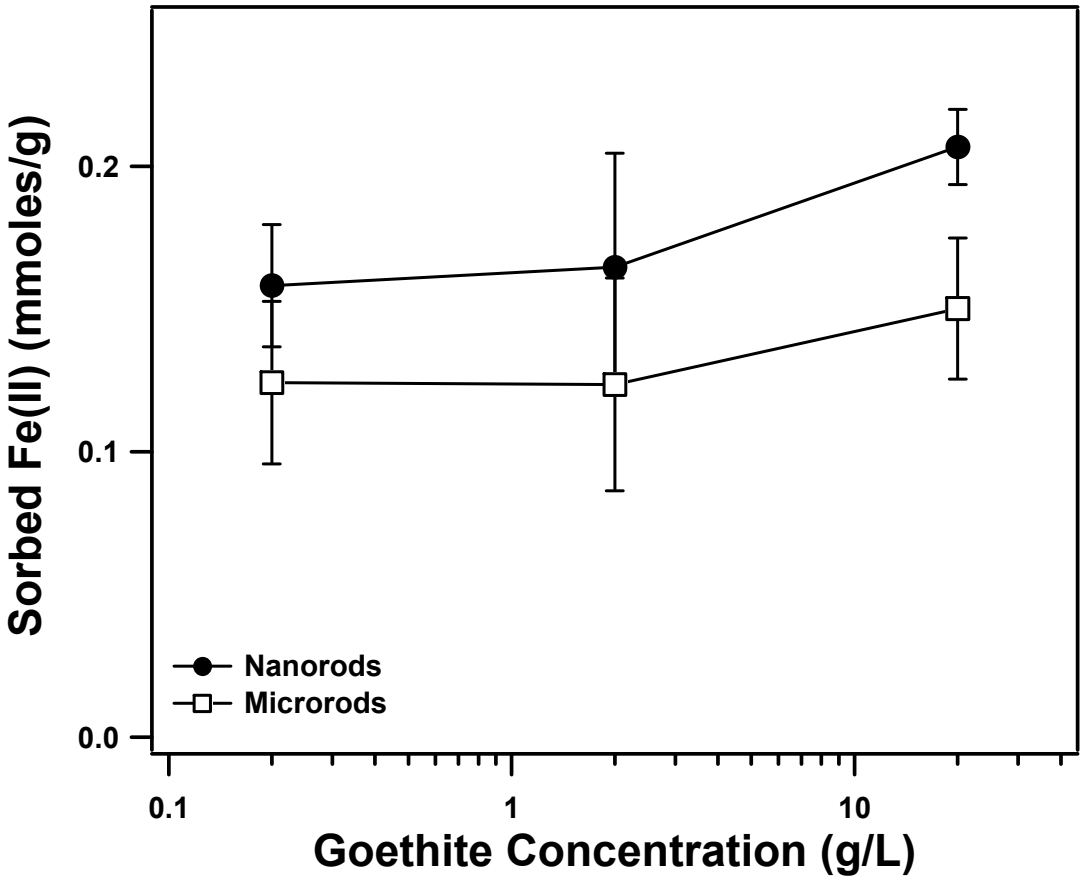

Figure 2.7 Concentration of sorbed Fe(II) as a function of goethite solids loading for nanorod and microrod suspensions at pH 7.5 (25 mM HEPES with 25 mM KBr). For each goethite concentration, experimental systems contained an initial ratio of 0.25 mmoles of Fe(II)(aq) per gram of goethite. Uncertainties represent one standard deviation determined from replicate experiments (n = 6).

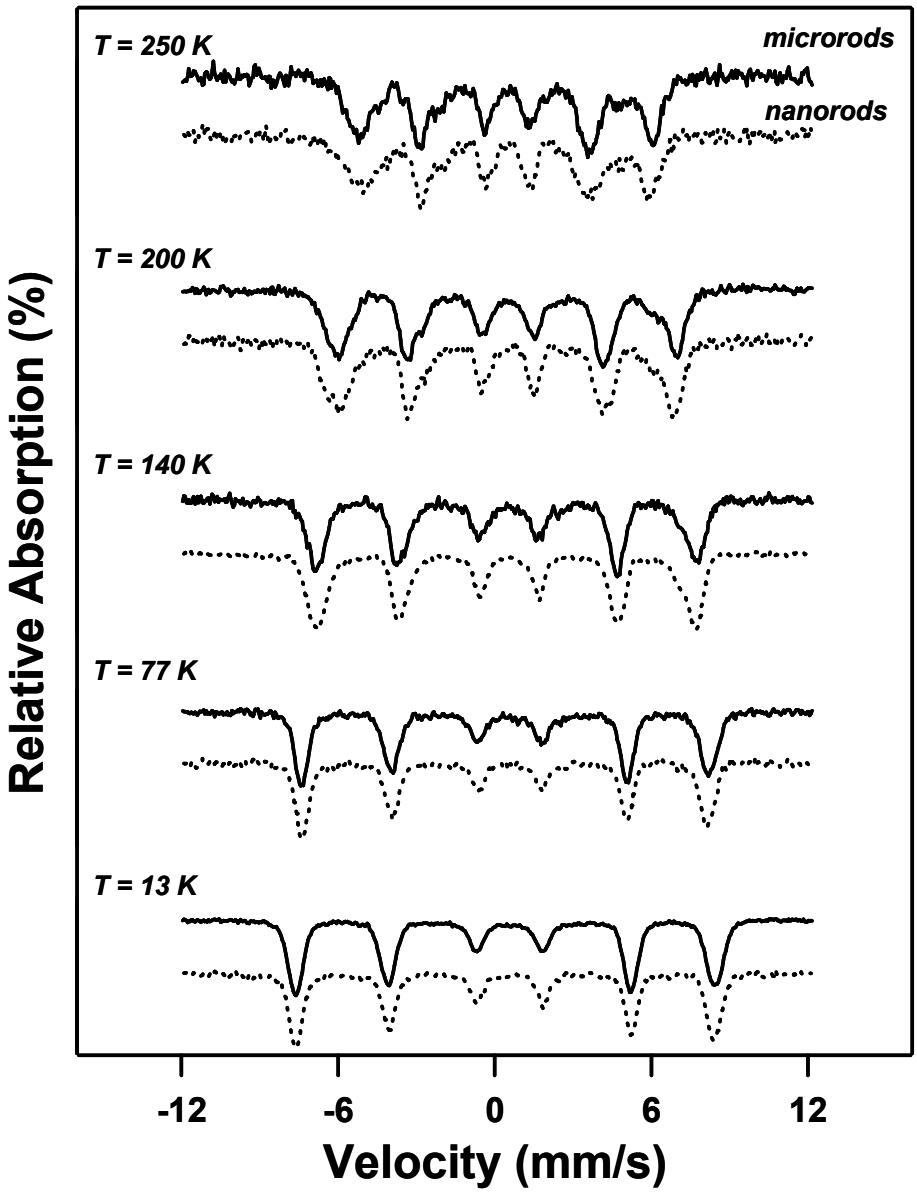

Figure 2.8 Temperature profiles of Mössbauer spectra for the reaction of aqueous phase ^{57}Fe(II) with isotopically enriched ^{56}Fe goethite nanorods (dashed lines) and microrods (solid lines). Reactions used an initial concentration of 25 mM ^{57}Fe(II) and 2 g/L goethite (30 mg into 15 mL) and were conducted at pH 7.5 (25 mM HEPES with 25 mM KBr). These conditions resulted in an equivalent concentration of sorbed ^{57}Fe (0.11 mmoles/g) in both nanorod and microrod suspensions.

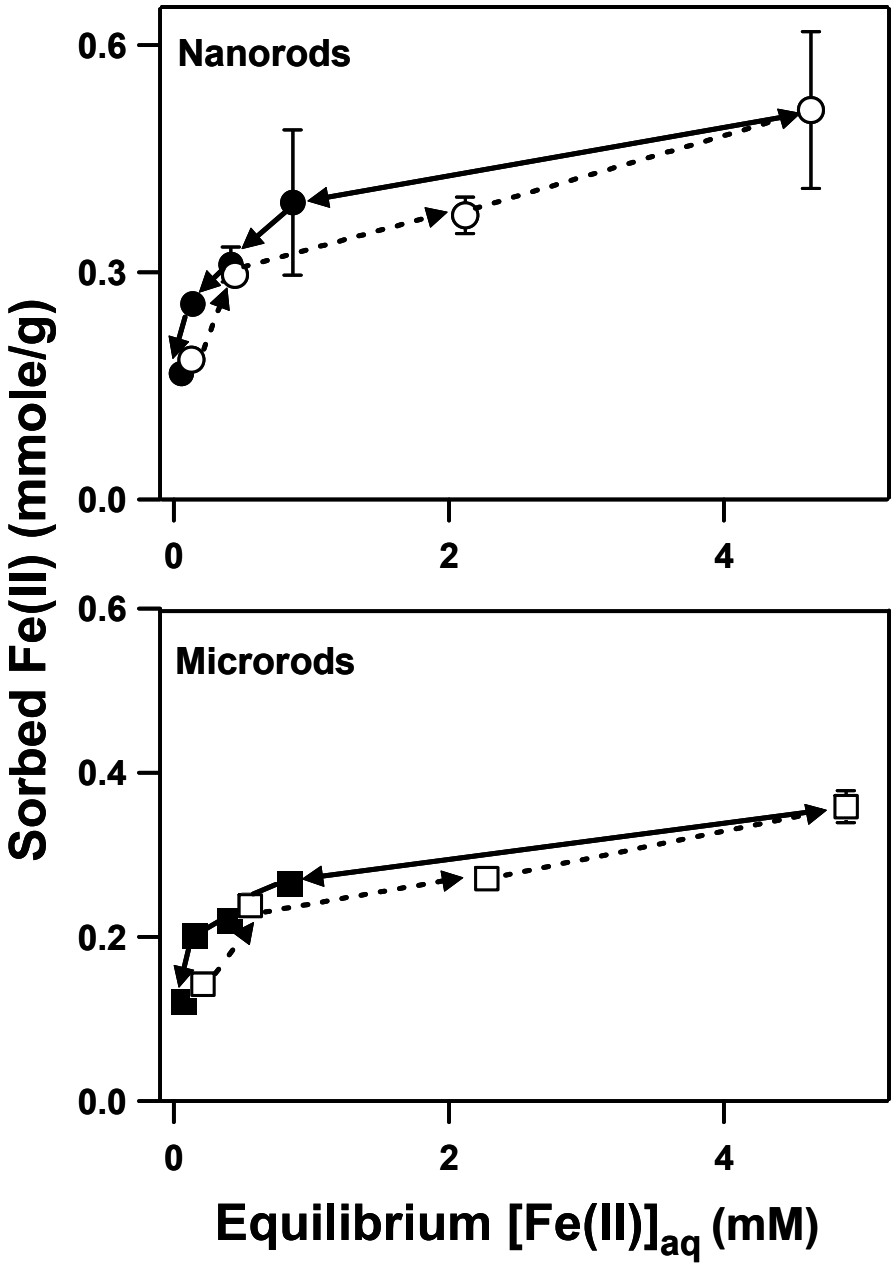

Figure 2.9 Results of Fe(II) recovery experiments. Open symbols correspond to the initial sorbed and aqueous Fe(II) concentrations in our experimental systems, whereas solid symbols represent the sorbed and aqueous Fe(II) concentrations after resuspension of the reacted goethite particles in more dilute Fe(II) solutions. Reactors contained 25 mM HEPES with 25 mM KBr at pH 7.5 and 2 g/L goethite (30 mg into 15 mL). Uncertainties represent one standard deviation determined from replicate experiments (n = 3).

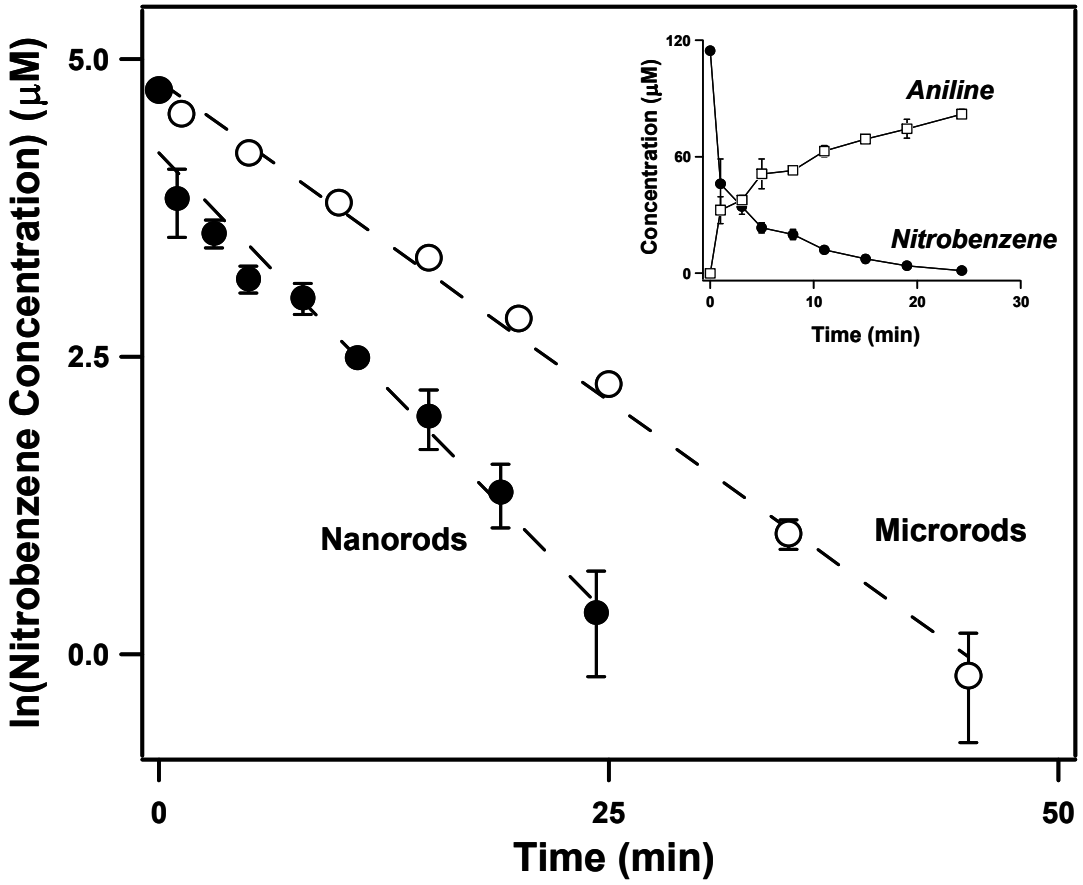

Figure 2.10 First-order plot of nitrobenzene concentration as a function of time in nanorod and microrod suspensions. Reactions were conducted at pH 7.5 (25 mM HEPES with 25 mM KBr) and contained an initial nitrobenzene concentration of approximately 100 μM, an initial aqueous Fe(II) concentration of 1 mM and 0.25 g/L goethite. Uncertainties represent one standard deviation determined from triplicate experiments. Dashed lines represent linear regression fits to the experimental data, from which k_{obs} values for nitrobenzene reduction were determined. The inset shows the concentration data as a function of time for nitrobenzene and aniline, the final product, in nanorod suspensions.

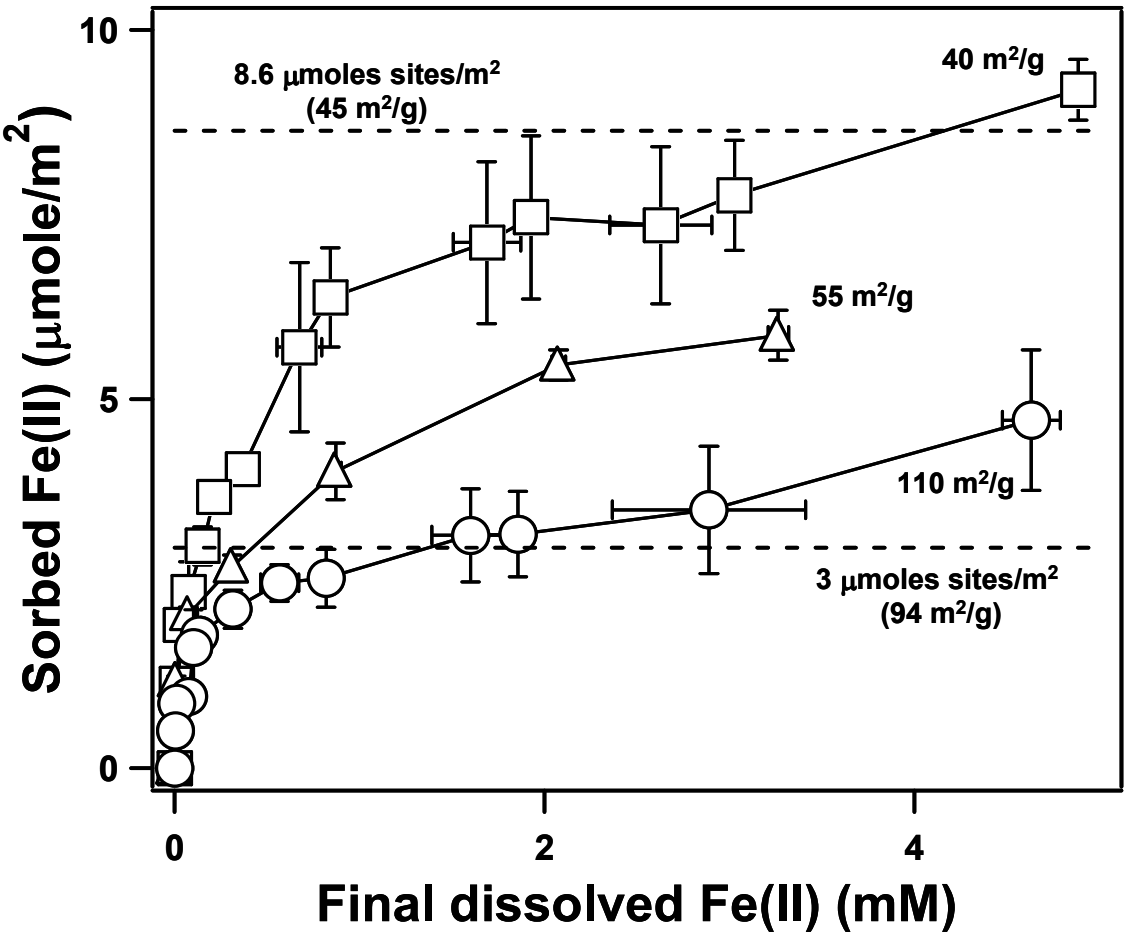

Figure 2.11 Isotherms in which sorbed Fe(II) concentrations are reported with units of µmole per square meter of goethite. Values were calculated using the sorption data in Figure 5 and measurements of N_2-BET specific surface area for each material. Dashed lines represent one monolayer of Fe(II) coverage estimated from surface site densities reported by Villalobos et al. (*77*), which were determined from proton and carbonate sorption studies performed with comparable sizes of synthetic goethite particles. The specific surface areas of the goethite particles investigated by Villalobos et al. (2003) are provided for comparison.

Table 2.1 Properties determined from the characterization of freeze-dried powders of the goethite particles synthesized in the current study.

	n^a	Length (nm)	Width (nm)^b	SA_{BET} (m^2/g)^c	SA_{TEM} (m^2/g)^d
Nanorods	530	80 ± 30^e	7 ± 2	110 ± 7^f	205
Nanorods (^{56}Fe)	100	85 ± 30	5.0 ± 1.3	90	264
Intermediate	240	330 ± 160	14 ± 4	55	92
Microrods	285	670 ± 370	25 ± 9	40 ± 3	52

[a] Number of unaggregated particles examined by TEM.

[b] Corresponds to the width of the 110 facet according to the convention of Anshutz and Penn (2005).

[c] Specific surface area determined from seven-point N_2-BET measurements.

[d] Specific surface area calculated assuming a rod geometry of a rhomboidal prism as in Anshutz and Penn (2005).

[e] Uncertainties on particle dimensions represent one standard deviation.

[f] When present, uncertainties on BET surface areas represent one standard deviation of triplicate measurements.

CHAPTER 3: ATOM EXCHANGE BETWEEN AQUEOUS FE(II) AND GOETHITE: AN FE ISOTOPE TRACER STUDY

Abstract

The reaction of aqueous Fe(II) with Fe(III) oxides is a complex process, comprised of sorption, electron transfer, and in some cases, reductive dissolution and transformation to secondary minerals. To better understand the dynamics of these reactions, we measured the extent and rate of Fe-isotope exchange between aqueous Fe(II) and goethite using a ^{57}Fe-isotope tracer approach. We observed near-complete exchange of Fe atoms between the aqueous phase and goethite nanorods over a thirty day time period. Despite direct isotopic evidence for extensive mixing between the aqueous and goethite Fe, no phase transformation was observed, nor did the size or shape of the goethite rods change appreciably. High-resolution TEM images, however, appear to indicate that some recrystallization of the goethite particles may have occurred. Near-complete exchange of Fe between aqueous Fe(II) and goethite, coupled with negligible change in the goethite mineralogy and morphology, suggests a mechanism of coupled growth (via sorption and electron transfer) and dissolution at separate crystallographic goethite sites. We propose that sorption and dissolution sites are linked via conduction through the bulk crystal, as was recently demonstrated for hematite. Extensive mixing between aqueous Fe(II) and goethite, a relatively stable iron oxide, has significant implications for heavy metal sequestration and release (e.g., arsenic and uranium), as well as reduction of soil and groundwater contaminants.

Handler, R. M.; Beard, B. L.; Johnson, C. M.; Scherer, M. M. Atom exchange between aqueous Fe(II) and goethite: An Fe isotope tracer study. *Environ. Sci. Technol.,* In Press

Introduction

The redox reactions of iron (Fe) influence a variety of global elemental cycles such as carbon and nitrogen through Fe-limited primary production (*80*). Redox transitions between soluble Fe(II) and solid Fe(III) phases are also suspected to play an important role in mobilization and transformation of a variety of trace heavy metals such as arsenic and lead (*81, 82*). A better understanding of these Fe redox processes is critical to our ability to predict and influence biogeochemical cycling of elements on a global and local level.

Microbial respiration of Fe(III) oxides results in significant quantities of reduced, soluble Fe(II) in subsurface environments (*83*). Reaction between aqueous Fe(II) and Fe(III) oxides has been studied extensively and these studies have revealed that the reaction is more complex than sorption alone. Experiments investigating reactions of Fe(II) with Fe oxides have often relied on solution phase measurements of Fe(II) after exposure to Fe oxides, attributing the loss of Fe(II) from solution to sorption. In some cases, Fe(II) lost from solution has not been completely recovered after lowering the solution pH (e.g., *84*), which has been interpreted as possible incorporation of Fe(II) within the Fe oxide surface structure or oxidation to Fe(III) (*85, 86*). We, as well as others, have used ^{57}Fe Mössbauer spectroscopy to show that after sorption, electron transfer occurs between sorbed Fe(II) and the Fe(III) oxide, forming an oxidized Fe surface layer (*11, 12, 87, 88*). Pedersen et al. used ^{55}Fe-labeled synthetic Fe oxides to show that aqueous Fe(II) can also catalyze reductive dissolution of Fe atoms originally bound within an Fe oxide (*14*). For the more unstable Fe(III) oxides, such as ferrihydrite and lepidocrocite, secondary mineralization to more stable Fe oxides such as goethite or magnetite has been observed (*10, 14, 58, 89*). Although sorption of Fe(II) to goethite and hematite occurs over a wide range of pH values (*84, 90*), and interfacial electron transfer has been demonstrated on these oxides (*12, 91*), no phase transformations have been observed, and little to no reductive dissolution of Fe(II) occurs after reaction of Fe(II)

with goethite or hematite, respectively (*14*). This leaves us with an unclear picture of the nature and extent of the reaction of Fe(II) with goethite, one of the most prevalent environmental Fe oxide phases.

A recent promising method for investigating the redox cycling of Fe involves selective use of Fe isotopes. There are four stable isotopes of Fe that differ widely in their natural abundance: ^{54}Fe (5.8%), ^{56}Fe (91.8%), ^{57}Fe (2.1%), and ^{58}Fe (0.3%) (*92*). Recent advancements in mass spectrometry (multi-collector inductively-coupled plasma mass spectrometry or MC-ICP-MS) allow us to distinguish between isotopes of heavy elements such as Fe with great precision (*93*). Stable isotope studies have been recently used to assess which biogeochemical processes might cause the variations in Fe isotope composition observed in nature (*28, 94-96*). For example, there have been several Fe isotope studies of Fe isotope fractionation caused by the interaction of aqueous Fe(II) with iron oxides. Icopini et al. (*97*) and Teutsch et al. (*98*) inferred that sorption of Fe(II) onto the iron oxide is an important process in controlling the Fe isotope composition of aqueous Fe, although these studies did not directly measure the sorbed Fe(II). Recent studies by Crosby et al. have shown that although sorption of Fe(II) onto iron oxides produces a measurable Fe isotope fractionation, the most significant control on the Fe isotope composition of aqueous Fe(II) is electron and isotope exchange with a reactive Fe(III) layer on the iron oxide substrate (*28, 99*).

In this study, we used a ^{57}Fe-enriched tracer to investigate atom exchange between aqueous Fe(II) and goethite. Importantly, the Fe isotope variations associated with this tracer approach are over 100 times greater than the mass-dependent Fe isotope fractionations that have been previously identified, allowing unambiguous identification of Fe isotope exchange. The approach used in this study is similar to that followed by Skulan et al. (*100*), Poulson et al (*101*), Welch et al. (*102*), and Shahar et al. (*103*) to identify isotope exchange between aqueous Fe(III) and hematite, aqueous Fe(III) and ferrihydrite, aqueous Fe(III) and Fe(II), and magnetite and fayalite, respectively. Here,

we react aqueous Fe(II) enriched in ^{57}Fe with goethite rods to identify isotope exchange between aqueous Fe(II) and goethite. We demonstrate that despite no obvious physical change in the goethite rods, the Fe isotopes become evenly dispersed between the aqueous phase and the solid Fe(III) lattice, which implies that near-complete mixing of Fe atoms has occurred.

Experimental Section

Goethite Synthesis and Characterization

The goethite solids used here are the same nanorod particles we synthesized and characterized in our previous work (*91*). Goethite rods had an average length and width of 81 ± 28 nm and 11 ± 4 nm, respectively and a specific surface area of 110 (± 7) m^2/g (*91*). XRD patterns and Mössbauer spectra were consistent with goethite (data not shown).

For solids characterization after mixing with or without aqueous Fe(II), XRD samples were prepared by combining filtered solids with a small amount of glycerol to create an oxide slurry to prevent oxidation of Fe(II). TEM samples were prepared by rinsing filtered solids with a small amount of deionized water (>18 MΩ-cm) to remove buffer salts and aqueous Fe(II), then resuspending the solids in deionized water before placement on a carbon-coated Cu grid. High-resolution TEM (HR-TEM) samples were prepared to examine variations in the crystal structure of goethite particles after exposure to Fe(II). HR-TEM samples were rinsed and suspended in DI water, then resuspended in methanol to reduce particle aggregation before placement on a holey carbon grid. High-resolution images were taken on a JEOL 2100-F electron microscope.

^{57}Fe(II) Isotope Tracer Experiment

All experiments were carried out in an anoxic glovebox, with care taken to prevent O_2 intrusion into the reactors during centrifugation outside of the anoxic

environment. All chemicals were reagent grade, and solutions were made in deionized water. HCl acid used in experimental procedures was purified by sub-boiling distillation. A ^{57}Fe-enriched aqueous Fe(II) stock was prepared in 0.5 M HCl by dissolving enriched ^{57}Fe (Chemgas, 96% ^{57}Fe) and adding a small amount to an isotopically normal Fe(II) stock to provide an ~80% increase in ^{57}Fe/^{56}Fe ratio relative to "normal" Fe. Use of enriched ^{57}Fe does not effect the rate of exchange as demonstrated by similar rates of exchange measured for $Fe(II)_{aq}$-$Fe(III)_{aq}$ using both ^{55}Fe and ^{59}Fe (*104, 105*), nor does use of enriched isotopic tracers affect the approach to isotopic equilibrium because there is no evidence for changes in mechanism as a function of mass.

Batch reactors were prepared by adding 15 mL of pH 7.5 HEPES buffer (25 mM HEPES plus 25 mM KBr electrolyte) to a 20 mL glass vial and adding Fe(II) stock to reach an initial Fe(II) concentration of ~1 mM. Vials were counter-spiked with 0.5 M KOH prior to Fe(II) addition in order to keep the pH stable at 7.5. After 1 h of equilibration, the Fe(II)-HEPES solution was filtered through an 0.2-μm filter into a 30 mL Nalgene centrifuge tube and the Fe(II) concentration was measured. Goethite solids were added to the reactors in pre-weighed 30 mg portions (solids loading 2 g/L), which were placed on an end-over-end rotator and allowed to mix in the dark for times ranging from 10 min to 30 d. The solution pH did not deviate more than ± 0.1 for the duration of the experiment. Control reactors were included with aqueous Fe(II) alone and goethite alone.

Three reactors were sacrificed at each time point for isotopic and chemical analyses. After centrifugation at 30,000*g*, the reactor supernatant was decanted, filtered into a new vial, and acidified for aqueous Fe(II) and total Fe analyses. Remaining goethite solids in the reactor were resuspended for 10 min with 5 mL of 0.4 M HCl to remove solid-associated Fe(II). After centrifugation and removal of the 0.4 M HCl supernatant, two successive acid extractions of the remaining solids were performed (5 mL of 1 M HCl, 45 minutes at 60 º C) to remove any remaining Fe(II) and dissolve a

small portion (~ 5%) of the Fe(III) within the goethite. The remaining bulk solids were completely dissolved in 5 M HCl. Here, we report only on the results for aqueous Fe(II) and Fe(III) from the remaining bulk solids.

Chemical Fe Analyses

Fe(II) concentrations were measured for aqueous and acid-dissolved Fe extractions using the 1,10-phenanthroline method with fluoride added to remove interference from aqueous Fe(III) (*106*). Fe(III) content in each extraction was determined by the difference between measured Fe(II) concentrations and total Fe content, which was obtained through addition of hydroxylamine hydrochloride reductant to separate Fe analysis samples.

Fe Isotope Analyses

Prior to isotopic analysis, all Fe samples were oxidized with hydrogen peroxide. Samples were purified using anion exchange chromatography (Fe yields from ion exchange columns were > 95%), and Fe isotopes were analyzed using a Micromass *IsoProbe*, a single-focusing MC-ICP-MS, following the methods of Beard et al. (*93*), except we did not use desolvation nebulization in order to allow for rapid wash out between solutions that differed by up to 80% in their Fe isotope compositions. Instead, solutions (3 ppm) were aspirated at 100 μL/min using a concentric flow nebulizer and a cyclonic spray chamber that was cooled to 5 ^{o}C. We report Fe isotope compositions in delta notation, which has the form:

$$\delta^{57/56}Fe\,(‰) = \left(\frac{\frac{^{57}Fe}{^{56}Fe}_{sample} - \frac{^{57}Fe}{^{56}Fe}_{std}}{\frac{^{57}Fe}{^{56}Fe}_{std}} \right) \times 1000 \qquad (1)$$

where $^{57}Fe/^{56}Fe_{std}$ is the average isotopic ratio for bulk igneous rocks (*94*). Based on replicate analyses of 33 samples passed through the entire analytical process, the average

1-standard deviation is 0.13‰ in $^{57}Fe/^{56}Fe$. Analytical uncertainties are slightly higher using the cyclonic spray chamber, as compared to using desolvation nebulization. During the course of this study the measured $\delta^{57/56}Fe$ value of the IRMM-014 standard was -0.03 ± 0.05‰ (1-SD; n = 4). Accuracy of Fe isotope results was checked by 9 analyses of synthetic samples that contained 0.5 mM Fe of known Fe isotope composition in the same matrix as the aqueous Fe samples. These synthetic samples were processed in the same fashion as samples and the measured $\delta^{57/56}Fe$ value of these synthetic samples (+0.38 ± 0.08‰) exactly matched the Fe isotope composition of the pure Fe standard (+0.37 ± 0.09‰, n = 25), demonstrating that our analytical technique is free of matrix effects. Partial acid digestion of goethite crystals demonstrated that the goethite used in the experiments is not isotopically zoned; the $\delta^{57/56}Fe$ of a 6% partial dissolution of goethite is -0.04‰, which is analytically indistinguishable from the $\delta^{57/56}Fe$ value of the remaining residue, -0.16‰.

Results and Discussion

We used Fe isotopes to track the movement of Fe between the aqueous phase and goethite during a batch Fe(II) sorption experiment. Aqueous Fe(II) was enriched with ^{57}Fe to give distinctly different isotopic compositions for the two reservoirs of Fe, aqueous Fe(II) and Fe(III) within the goethite structure (Figure A7). The enriched aqueous Fe(II) contained roughly twice as many ^{57}Fe atoms as would be expected in nature ($\delta^{57/56}Fe$ = +840.43‰). Goethite rods were not enriched and had an initial $\delta^{57/56}Fe$ value of -0.12‰. Enriching the aqueous Fe(II) with ^{57}Fe allowed us to track the movement of Fe atoms between the aqueous phase and solid phase by measuring the $\delta^{57/56}Fe$ of each phase over time with MC-ICP-MS. The same kinetic results would be obtained if isotopically normal Fe(II) and ^{57}Fe-enriched goethite were used (e.g., *100*).

Over the course of thirty days, the $\delta^{57/56}Fe$ values of aqueous Fe(II) decreased from +840.43 to +39.94‰, indicating that some of the ^{57}Fe-enriched aqueous Fe had

been replaced with ^{56}Fe atoms (Figure 3.1). The $\delta^{57/56}$Fe values of the goethite solids rose sharply from -0.12 to +38.75‰, implying that isotopic exchange had occurred and the content of ^{57}Fe relative to ^{56}Fe had increased in the goethite solids. By the end of the experiment, the aqueous and goethite Fe reservoirs reached similar isotopic compositions of +39.94 ± 1.16‰ and +38.75 ± 0.72‰, respectively (± 1 std. dev.), demonstrating that significant mixing occurred between the two reservoirs. No significant changes in $\delta^{57/56}$Fe values of control reactors (goethite alone or aqueous Fe(II) alone) were detected (data not shown).

To evaluate the extent of mixing, we calculated a mass balance-weighted isotopic composition of the two-component system using:

$$\delta^{57/56}Fe_{sys} \times \left[Fe_{goethite} + Fe_{spike}\right] = \delta^{57/56}Fe_{goethite} \times \left[Fe_{goethite}\right] + \delta^{57/56}Fe_{spike} \times \left[Fe_{spike}\right] \quad (2)$$

where $\delta^{57/56}$Fe and [Fe] refer to the ^{57}Fe/^{56}Fe ratio in delta notation and molar amounts of the initial goethite and Fe(II) spike given in the first row of Table 3.1. If complete mixing occurred between the Fe atoms in goethite and the aqueous Fe(II) atoms, the homogenized Fe suspension would have a $\delta^{57/56}Fe_{sys}$ of +37.57 ± 1.15‰ (dashed line in Figure 3.1). The aqueous and goethite Fe(III) $\delta^{57/56}$Fe values of +39.94 and +38.75‰ measured at the end of the experiment are remarkably close to the $\delta^{57/56}Fe_{sys}$ of +37.57‰ calculated for the completely mixed isotopic composition and indicate that greater than 95% exchange occurred. Convergence of the aqueous and goethite $\delta^{57/56}$Fe values to the calculated value for complete mixing demonstrates that the Fe atoms in the aqueous phase and goethite solids have become nearly completely mixed over a period of thirty days.

Previous work has also provided evidence that atom exchange between Fe(III) oxides and aqueous Fe(II) occurs. Pedersen et al. incorporated ^{55}Fe into several different Fe oxides and observed the release of ^{55}Fe into solution upon exposure to aqueous Fe(II)

(*14*). Release of ^{55}Fe into solution was observed for lepidocrocite, ferrihydrite, and goethite, but not for hematite. With lepidocrocite and ferrihydrite, the amount of ^{55}Fe released into solution approached isotopic equilibrium and was accompanied by significant phase transformation. For goethite, however, they observed much less exchange with only 5 to 10% of the goethite atoms released into solution after 16 days, and no apparent phase transformation. Here, we observed significantly more atom exchange with most of the goethite atoms exchanged after thirty days. Relative to the experimental conditions of Pedersen et al., our goethite particles have a greater surface area (110 vs. 37 m^2/g), and we worked at a higher solution pH (7.5 vs. 6.5) and higher solids loading (2 g/L vs. ~50 mg/L). These differences, as well as other experimental variables, such as pH buffer and background electrolyte may have contributed to the differences in amount of Fe exchanged in the two goethite experiments. Despite differences in the extent of Fe atom exchange, both the isotope data here and the ^{55}Fe release observed by Pedersen et al. provide compelling evidence that significant atom exchange occurs between goethite and aqueous Fe(II).

Recent work by Jang et al. (*96*) has also investigated the interaction between Fe(II) and goethite using natural Fe isotope abundances. $\delta^{56/54}$Fe values were measured for aqueous Fe(II), as well as 0.5 M HCl-extractable Fe(II) using solution conditions analogous to those used here. Based on a mass-balance estimate, the authors concluded that isotope mixing between Fe(II) and goethite Fe(III) atoms occurs. Here, by using ^{57}Fe as a tracer in the aqueous phase, we were able to simultaneously track the aqueous and solid phase isotope ratios and demonstrate, by direct measurements, that atom exchange between Fe(II) and goethite does indeed occur and that it is extensive enough to reach isotopic equilibrium.

Despite the extensive Fe exchange observed in our isotope tracer experiment, the aqueous Fe(II) concentration remained relatively stable after initial Fe(II) uptake. Within minutes, the aqueous Fe(II) concentration decreased from 1.07 to 0.55 mM and remained

relatively constant over the remaining thirty days (Table 3.1 and Figure A8). A similar amount and rate of Fe(II) sorption was observed in our previous work with these particles resulting in an estimated surface coverage well below monolayer (i.e., about 30% assuming 4 sites/nm^2 and an idealized goethite geometry) (*91*). We do not see any evidence of the slower, gradual decrease following an initial rapid uptake that has been reported by several others and attributed to a transition between outer-sphere and inner sphere adsorption, or the formation of surface-associated Fe(II) structures (*9, 86, 90*). The average Fe(II) recovery over our entire experimental procedure was > 96% (calculated from the total of Fe(II) recoveries in each of the five sample extractions), indicating that losses of Fe(II) throughout the sampling procedures and acid extractions were minimal. Our observation that aqueous Fe(II) concentrations were relatively stable despite significant changes in the $\delta^{57/56}$Fe values suggests that the system was at steady-state conditions and that isotopic exchange occurred without significant net dissolution or precipitation occurring beyond the initial Fe(II) loss from solution.

In the solid phase, negligible change was observed in the mineralogy, shape, or size of the goethite particles before and after reaction with Fe(II). XRD patterns revealed no formation of secondary mineral phases and negligible increases in average crystallite size via the Scherrer equation (Figure A9). Lattice spacings from HR- TEM images are also consistent with goethite confirming that there was no significant formation of a secondary mineral phase (Figure A10). TEM images revealed little change in the size and shape of the goethite particles when exposed to 1 mM Fe(II) (Figure A11). A more quantitative assessment of the particle size distribution on the TEM images shows no change in the length (81 ± 28 nm to 82 ± 32 nm) or width (11 ± 4 nm to 11 ± 5 nm) of the goethite (Figure 3.2). Interestingly though, HR-TEM images suggest that some changes to the goethite particles may have occurred during Fe isotope exchange (Figure A10). After reaction with Fe(II) for thirty days, the rods appear to have become more

crystalline. The potential for re-crystallization after reaction with Fe(II) is an avenue we are currently exploring with additional HR-TEM work.

How such extensive Fe atom exchange can occur, as required by the isotopic data, with no significant morphological change is a fascinating question. Diffusion of Fe through the solid goethite structure is one potential explanation. Solid-state diffusion rates have been measured for Fe atoms in various solid Fe phases (*107-109*), but generally these studies are performed at temperatures ranging from ~700-1500 °C in order to generate Fe diffusion rates that were measurable on reasonable experimental time scales. Even if Fe atom diffusion were to occur solely along crystallite grain boundaries or defect sites, estimates of diffusion time of Fe at room temperature would exceed millions of years to move just a few nanometers through an Fe oxide lattice.

Although we can eliminate solid-state diffusion as a reasonable explanation for Fe isotope exchange, we cannot rule out the possibility of diffusion through micropores in the goethite structure. Diffusion through micropores has often been invoked to explain the gradual loss of ions from solution in the presence of iron oxides (*110, 111*). Recently, long-term rates of loss of a variety of metal cations (not Fe) from solution in the presence of goethite has been correlated with ionic radius, which has been interpreted as evidence for a micropore diffusion mechanism governing incorporation of these ions into goethite (*112*). Here, however, we see a stable aqueous Fe(II) concentration after the initial Fe(II) sorption, which suggests that gradual diffusion into goethite micropores is not a likely explanation for the Fe atom exchange we observe here.

Another potential mechanism to explain how all the Fe goethite atoms have become mixed with the Fe atoms in solution is coupling electron conduction through the bulk goethite with growth and dissolution. Yanina and Rosso recently demonstrated that a potential gradient can be measured between different crystal faces on hematite, and that conduction through the bulk oxide can result in growth and dissolution at separate crystal

faces (*13*). We propose that a similar mechanism may be associated with Fe(II)-goethite exchange.

From our previous studies utilizing Mössbauer spectroscopy, we know that sorption of Fe(II) onto goethite results in electron transfer between the sorbed Fe(II) and the structural Fe(III) in goethite (*11, 87*). We also know that oxidation of the sorbed Fe(II) results in growth of goethite on goethite (i.e., homoepitaxy) (*11*), as well as injection of an electron into the goethite structure. We do not know the exact fate of the electron, but from the ^{55}Fe dissolution and stable isotope work of others (*14, 96*), and our isotope data here, it is clear that some of the bulk Fe(III) goethite is reduced and released into solution. If the electron was transferred from sorbed Fe(II) through the Fe lattice by bulk conduction across a potential gradient, the goethite Fe(III) atom could be dissolving at a different location on the goethite surface. These newly-reduced Fe(III) atoms, now Fe(II), could then dissolve into the aqueous phase, exposing fresh Fe(III) atoms in goethite to the aqueous phase. Through a repeated series of these five steps of sorption–electron transfer–crystal growth–conduction–dissolution, a redox-driven conveyor belt could be established that would allow all of the goethite to be eventually exposed to the aqueous phase and exchanged (Figure 3.3). This surface-mediated exchange process would result in similar Fe isotope distributions in the aqueous phase and goethite particle as we have observed here. This mechanism is also consistent with a stable aqueous Fe(II) concentration if there were equal rates of goethite growth and dissolution - i.e., no net growth and dissolution beyond the initial Fe(II) uptake.

At this point, however, it is unclear if electron transport rates are fast enough in goethite for the conveyor belt model to explain the extensive atom exchange we observed over a few weeks. For electron transport to occur through the bulk goethite, a potential gradient needs to exist between different crystal sites and the goethite has to be sufficiently conductive. Goethite is about ten-fold less conductive than hematite (*113*). The limitations imposed by lower conductivity, however, are compensated by the much

shorter electron transport paths for the goethite rods (< 100 nm) compared to the hematite single crystal (1 mm) used by Yanina and Rosso (*13*). It therefore seems reasonable that the goethite nanorods could be sufficiently conductive at the nm scale to support a conveyor belt mechanism.

Because we see no net change in crystal shape of the goethite particles, it is more difficult to argue that a potential gradient exists between different crystal faces. Our analysis, however, is based on average length and width values obtained from TEM images. We could be missing subtler changes in the crystals, such as changes in crystal faces that parallel the *c*-axis or changes in the step density or surface roughness. There is some evidence that both of these changes occur on goethite particles in the presence of Fe(II). For example, a difference in growth rates for the (100) and (110) faces of goethite was reported when Fe(II) was oxidized by oxygen suggesting different reactivity for the (100) and (110) faces, which both run parallel to the *c*-axis (*114*). Chun and colleagues also observed preferred oxidation of Fe(II) and reduction of an organic contaminant at a specific crystal face, leading to growth along the *c*-axis and increased roughness of the goethite particle tips (*115*).

The environmental implications of complete atom exchange between Fe(II) and goethite observed are significant. Goethite and other stable Fe oxides are considered major sources and sinks of trace heavy metals, and formation and dissolution of Fe oxides can control metal availability in natural and engineered systems (*116, 117*). We have demonstrated here that despite an apparent phase stability in Fe(II)-goethite suspensions, there is actually a tremendous amount of Fe atom cycling occurring between phases and oxidation states. In the presence of aqueous Fe(II), heavy metals thought to be sequestered in bulk Fe oxides may actually become available on the particle surface or in the aqueous phase as a result of this exchange. Conversely, a larger than expected uptake of metals from the aqueous phase could occur as a result of the continuous reformation of the Fe oxide structure, exposing the entire crystal for equilibration and sequestration of

metals, rather than just the surface sites or porous cavities. Indeed, previous work has demonstrated that the addition of minute quantities of Fe(II) to a goethite suspension can induce measurable increases in sorption of other metal cations, despite the prevailing assumption that the Fe(II) would merely compete for goethite surface sites (*85*). The implications of such significant mixing between aqueous Fe(II) and Fe(III) oxides require further investigation, and subsequent predictive and modeling efforts should consider the effects of Fe exchange in the presence of aqueous Fe(II).

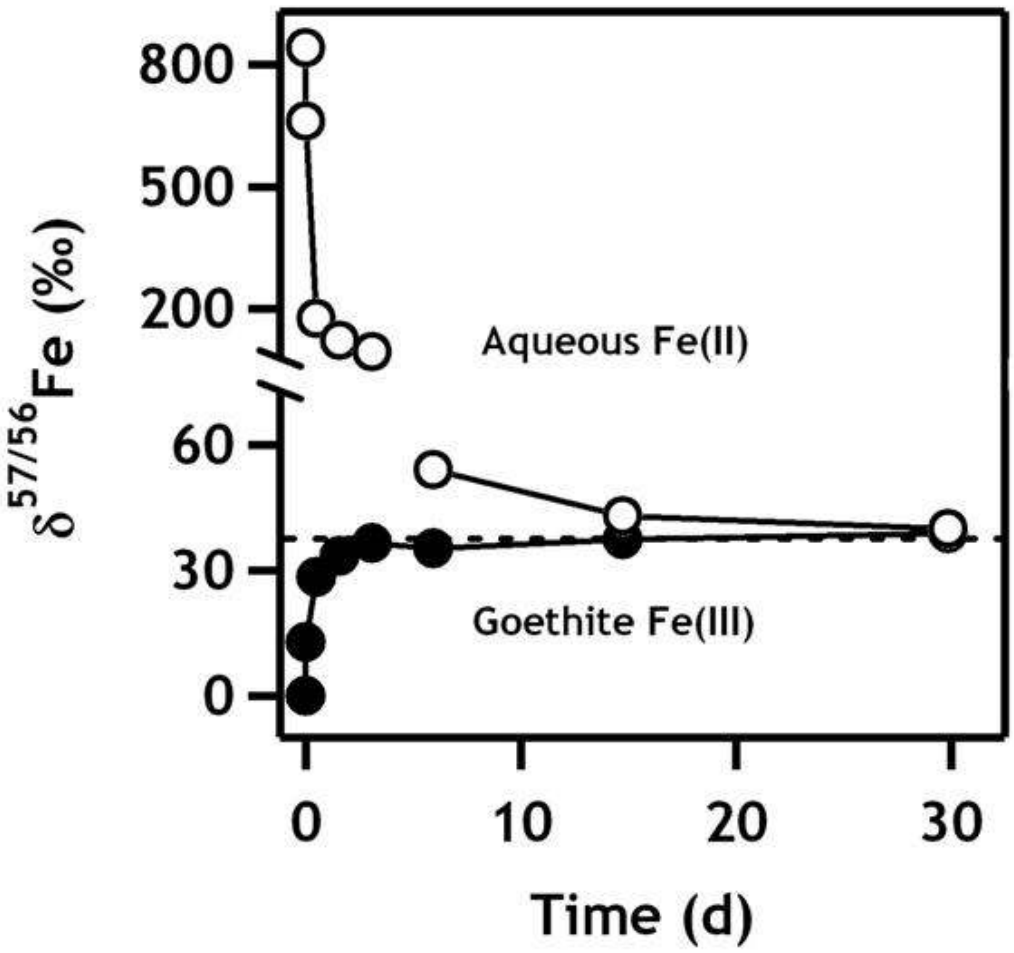

Figure 3.1 Measured $\delta^{57/56}$ values of aqueous (○) and goethite-Fe (●) over time. The dashed line is the calculated completely mixed $\delta^{57/56}$ Fe value of 37.57‰, calculated from eq. 2 in the text (i.e., $\delta^{57/56}Fe_{sys}$ = (15.85 × 840.43 + 337.66 × -0.12) / (15.85 + 337.66) = 37.57). Because the initial molar amount of aqueous Fe(II) was much smaller than the amount of Fe initially present within the goethite particles (15.85 μmol vs. 337.66 μmol, respectively), the completely mixed $\delta^{57/56}$ Fe value calculated using eq. 2 is much closer to the initial isotopic composition of the goethite solids than the aqueous Fe(II). Each data point represents the average of triplicate reactors. Standard deviations of replicates are contained within markers.

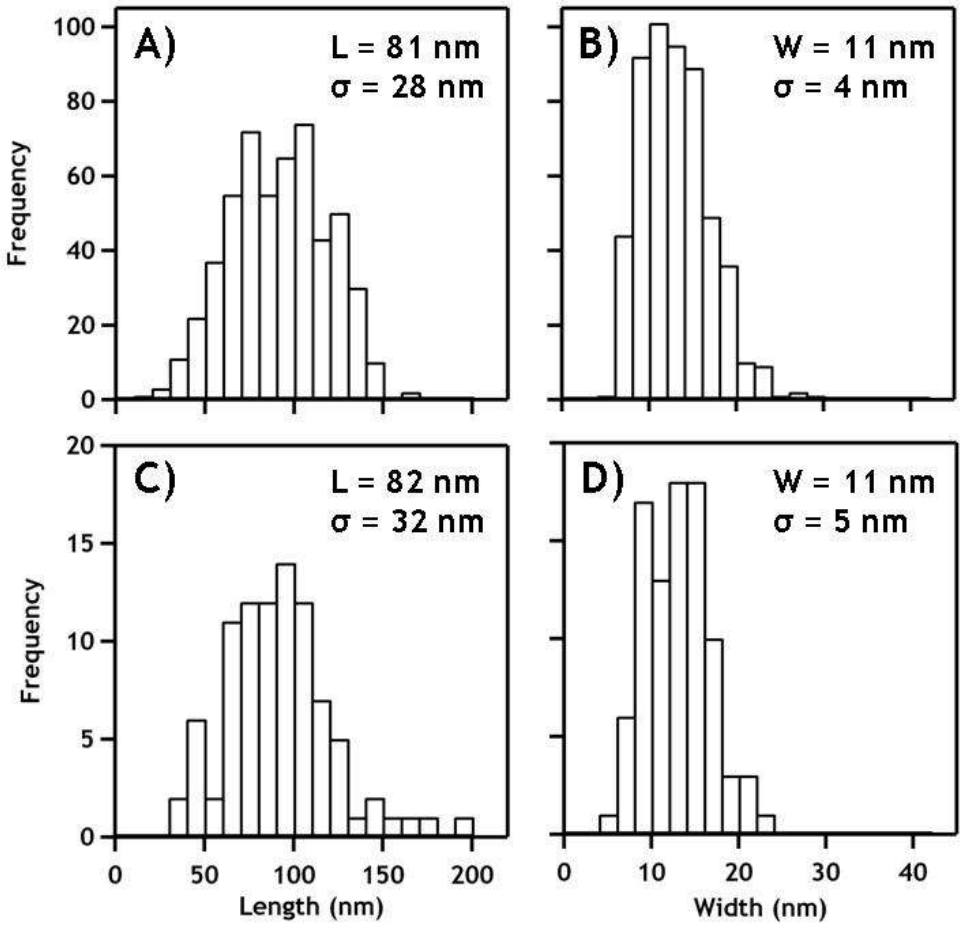

Figure 3.2 Particle size distributions for length and width of goethite particles before (A and B) and after reaction with Fe(II) (C and D). More particles were included in the analysis for untreated goethite rods than goethite reacted with Fe(II) (n = 530 vs. n = 91), resulting in greater frequency numbers in panels A and B. Average particle lengths or widths and 1-standard deviations are shown in panels.

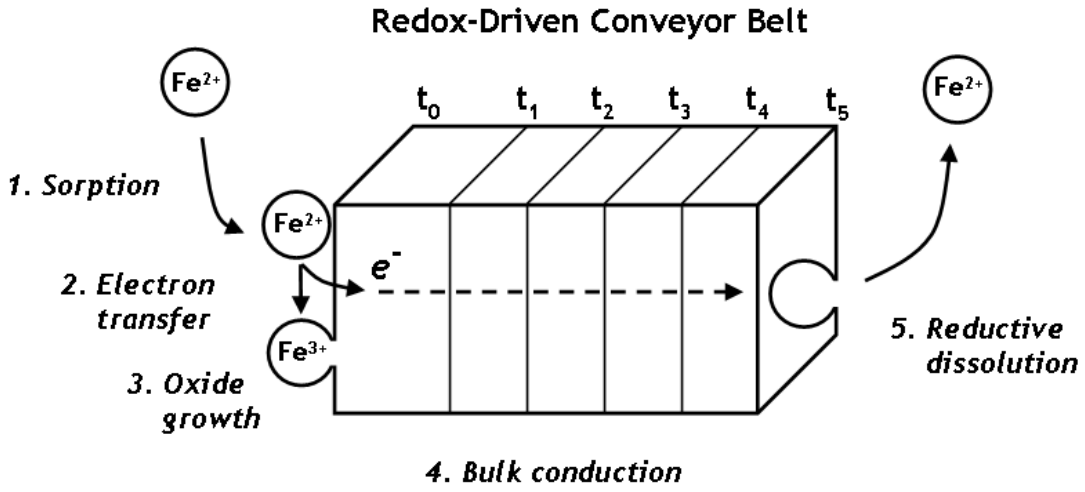

Figure 3.3 Conceptual model for the five steps associated with the redox-driven conveyor belt mechanism to explain how bulk goethite Fe(III) atoms and aqueous Fe(II) can become completely mixed via growth and dissolution at separate goethite surface sites. The left surface may be considered a reference plane in the original goethite crystal at the start of the process (t_0), and through growth on the left and dissolution on the right, this reference plane will migrate over time ($t_0 \rightarrow t_5$) until time t_5, at which point 100% atom exchange has occurred.

Table 3.1 Chemical and isotopic data during enriched Fe isotope tracer experiment.

	Aqueous Fe(II)			*Goethite* [a]	
Time	$Fe(II)_{aq}$ mM	$Fe(II)_{aq}$ µmol	$\delta^{57/56}Fe$ (‰)	$Fe(III)_s$ µmol	$\delta^{57/56}Fe$ (‰)
0	1.07 (0.03) [b]	15.85 (0.46)	840.43 (0.18)	337.66 (3.4) [c]	- 0.12 (0.02)
10 min	0.55 (0.01)	8.17 (0.17)	660.64 (13.21)	332.96 (17.99)	12.71 (0.16)
12 h	0.52 (0.00)	7.70 (0.06)	176.95 (10.60)	278.27 (8.37)	28.25 (0.19)
1.6 d	0.57 (0.01)	8.48 (0.12)	122.36 (2.50)	263.82 (8.47)	33.36 (0.26)
3.1 d	0.62 (0.01) [d]	9.14 (0.13)	94.72 (8.22)	275.24 (4.54)	36.47 (0.32)
5.9 d	0.54 (0.01)	8.02 (0.17)	54.00 (1.81)	301.88 (4.43)	35.13 (0.90)
14.8 d	0.52 (0.04)	7.78 (0.61)	43.01 (1.87)	297.35 (13.84)	37.38 (1.70)
30 d	0.54 (0.01)	8.05 (0.14)	39.94 (1.16)	309.30 (15.01)	38.75 (0.72)

[a] - Goethite measurements were collected on all remaining solids at the end of the sequential extraction procedure by completely dissolving solids in 5 M HCl at 60 ºC .

[b] - Numbers in parentheses represent one standard deviation based on triplicate reactors; this standard deviation does not reflect the analytical uncertainty of an Fe isotope measurement but rather the consistency of the entire experiment. The analytical uncertainty of a single $\delta^{57/56}Fe$ measurement is ± 0.13‰ based on replicate analysis of samples and standards, as reported in the text.

[c] - Differences in $Fe(III)_s$ recoveries are due to varying losses of goethite solids during decanting and filtration steps prior to complete dissolution of the remaining bulk goethite.

[d] - Samples sacrificed after t = 3.08 d were inadvertently spiked with a slightly higher initial Fe(II) concentration, hence the slightly higher aqueous Fe(II) concentration of 0.62 mM.

CHAPTER 4: REDOX-DRIVEN ATOM EXCHANGE BETWEEN FE(II) AND GOETHITE: EFFECT OF PARTICLE SIZE AND PH

Abstract

Using a ^{57}Fe-isotope tracer approach, we previously demonstrated that extensive mixing and exchange occurs between aqueous Fe(II) and goethite nanorods at pH 7.5. Here, we measured the influence of particle size and pH on the rate and extent of exchange in order to probe the mechanism of exchange. We observed little difference in the rate or extent of exchange between goethite nanorods (81 x 11 nm) and microrods (590 x 42 nm) at pH 7.5, suggesting that bulk conduction through primary particles was not limiting the rate of atom exchange. Similar rates of exchange for both nanorods and microrods are consistent with theoretical estimates of rapid electron conduction between Fe atoms in goethite particles of this size. At solution pH 5.0, negligible loss of Fe(II) from solution was observed, yet significant exchange still occurred. The rate of exchange, however, was much slower than observed at pH 7.5. Differences between goethite nanorods and microrod atom exchange rates do appear at pH 5.0, corresponding to differences in specific surface area between the two goethite samples, supporting our previous findings that aggregation of primary particles could be controlling macroscopic reactivity. At pH 7.5, measurements of sequential extractions of goethite-Fe(II) reactors indicated initial enrichment of ^{57}Fe in solid-associated Fe(II) and labile surface Fe(III) relative to bulk goethite before gradual convergence to the system-wide average $\delta^{57/56}$Fe value. ^{57}Fe enrichment in labile surface Fe(III) was more extensive at pH 5.0, due to slower overall atom exchange between Fe(II) and goethite or isolated exchange between aqueous Fe(II) and surface Fe(III) atoms. A mechanism of Fe(II) oxidation and Fe(II) reduction at spatially distinct sites, linked via conduction through the bulk crystal, can explain our experimental results, consistent with demonstrated mechanisms operating in Fe(II)-hematite systems. Rates of redox-driven atom exchange appear to be limited by

processes involving Fe(II) interactions with Fe oxides surface sites. Extensive mixing between aqueous Fe(II) and goethite, a relatively stable iron oxide, has significant implications for heavy metal sequestration and release (e.g., arsenic and uranium), as well as reduction of soil and groundwater contaminants.

Introduction

Redox transformations between reduced and oxidized iron (Fe) exert substantial influence on groundwater chemistry. Transformations of Fe between oxidation states and various mineral or aqueous species has been shown to impact nutrient availability, heavy metal cycling, and contaminant remediation (*3, 81, 118, 119*). Heterogeneous interactions between aqueous Fe(II) and Fe oxides or oxyhydroxides (hereafter collectively referred to as oxides) have not been adequately described using traditional models of cation association to a mineral surface. Recent experimental evidence has shown that neither associated Fe(II) or the solid phase Fe are static or unchanging species due to heterogeneous redox chemistry between sorbed Fe(II) and Fe(III) solids. Researchers have been unable to recover Fe(II) lost from solution in the presence of an Fe oxide, even when lowering solution pH to levels that should produce complete dissociation of a cation adsorbent. Resulting desorption hysteresis effects have been attributed to the ability of certain Fe oxides to trap electrons in ill-defined bulk interior regions, or to the formation of Fe(II):Fe(III) solid solutions on the solid surface (*62, 86*). Explanations of incomplete Fe(II) recoveries involving a stable Fe(II) component of the solid phase often invoke electron transfer between solid-associated Fe(II) and the participating Fe oxide. Direct spectroscopic evidence of electron transfer between aqueous Fe(II) and goethite, hematite and ferrihydrite was demonstrated by Williams and Scherer, who utilized ^{57}Fe Mössbauer spectroscopy coupled with selective use of Fe isotopes in aqueous and solid phases (*11*), a technique which has been used in further studies to indicate Fe(II)-Fe(III) electron transfer over a range of Fe(II) loadings and pH values (*12, 26, 87*).

It was also demonstrated by Williams and Scherer (*11*) that Fe(II) taken up from solution is not necessarily available for contaminant reduction, further suggesting that electrons transferred to the solid may be confined to an unreactive portion of the Fe(III) oxide. Additional research has shown that the net amount of Fe(II) taken up from solution during sorption to hydrous ferric oxide and goethite remained constant during oxidation of aqueous Fe(II) by molecular oxygen, and sorbed Fe(II) persisted long after all remaining aqueous Fe(II) had been removed from solution (*120*). Rates of Fe(II) oxidation, however, were dependent on both dissolved Fe(II) and sorbed Fe(II) concentrations. This observation was rationalized by invoking a mechanism involving separate sites of Fe(II) oxidation and O_2 reduction on the particle surface.

Further evidence for surface proximity effects in semiconductor materials has come from combined microscopy and modeling studies, indicating that chemical changes in one surface location can induce significant changes at distinct sites at the particle surface (*121*). The distance at which redox changes at a particular surface site, in this case due to Fe(II) sorption and electron transfer, could impact separate sites on the particle surface would be determined by the intrinsic conductivity of the material, as well as the presence of step or kink sites along the surface to provide minute differences in surface chemical properties.

Extensive interaction between aqueous Fe(II) and relatively unstable Fe oxides, such as ferrihydrite and lepidocrocite, has been demonstrated by observing changes in the solid phase. Secondary mineralization pathways in unstable Fe oxides have been demonstrated previously, demonstrating significant recrystallization of Fe phases to more stable Fe oxides (*10, 89, 122*). Pedersen et al. exposed a host of synthetic, ^{55}Fe-labeled Fe(III) oxides to aqueous Fe(II) and measured ^{55}Fe moving into the aqueous phase over time as evidence of reductive dissolution. Unstable Fe oxides such as ferrihydrite and lepidocrocite released significant amounts of ^{55}Fe into solution, providing a clear indication of Fe exchange between Fe(II) and Fe(III) oxides (*14*). Fe exchange in these

cases was coupled to extensive secondary mineralization, producing new Fe phases as determined by X-ray diffraction (XRD). The extent of interaction between aqueous Fe(II) and more stable Fe oxides due to a similar mechanism is not as evident, however, due to the absence of a noticeable mineral transformation in these systems. Previous work has demonstrated electron transfer between aqueous Fe(II) and stable oxides such as goethite and hematite (*11, 87, 91, Chapter 2*), and Pedersen and colleagues observed a minimal release of ^{55}Fe from radiolabeled goethite after exposure to aqueous Fe(II), but almost no release in hematite. These observations taken together indicate the presence of a redox interaction between Fe(II) and goethite or hematite, but the extent to which solid Fe(III) is redox-active was hard to characterize either quantitatively (how much Fe(III) is participating?) or spatially (what atomic locations in Fe oxides are open to exchange?).

Yanina and Rosso used a combination of potentiometry and microscopy to demonstrate electron conduction through the interior of hematite particles, building on previous modeling simulations of conduction in hematite (*123-125*). Fe(II) exposure to hematite at a solution pH of < 5 in the presence of oxalate resulted in hematite growth on (001) crystal faces coupled to hematite dissolution at (012) crystal faces, inducing a measurable electric potential between distinct hematite surfaces (*13*). Demonstration of a "chemically induced surface potential gradient" in hematite, as postulated by previous work, provides a potential mechanistic explanation for the extensive reworking of Fe oxide minerals upon Fe(II) exposure.

Indirect evidence of a similar mechanism controlling Fe(II)-goethite redox activity has recently been provided by studies measuring the isotope ratios of Fe atoms during Fe(II)-goethite mixing. Analysis of stable isotope ratios with great precision has become possible using multi-collector inductively-coupled plasma mass spectroscopy (MC-ICP-MS), permitting measurement of subtle shifts of Fe isotope ratios as indicators of a variety of biogeochemical processes (*95, 98, 99, 126*). Jang et al. mixed aqueous Fe(II) ($\delta^{56/54}Fe$ = -0.08‰) and goethite ($\delta^{56/54}Fe$ = -0.27‰) at pH 7.5, and measured

amounts and isotope ratios of aqueous and total acid-extractable Fe(II). Over the course of a week, aqueous Fe(II) became isotopically lighter, which implied, through mass-balance considerations, that the sorbed component of total acid-extractable Fe(II) was enriched in heavy isotopes. $\delta^{56/54}$Fe values for total acid-extractable Fe(II) also approached initial $\delta^{56/54}$Fe for goethite, which was interpreted as evidence for extensive Fe atom exchange between Fe(II) and goethite.

Our recent experimental work using enriched Fe(II) and isotopically-normal goethite demonstrates this effect through the use of an enriched ^{57}Fe(II) tracer to enhance the ability to detect shifts in the initial Fe(II) isotope signature (*127,Chapter 3*). We coupled this stable isotope tracer approach with direct isotope measurements of the Fe(III) solid, indicating that isotope ratios of both aqueous and solid Fe changed from very different starting conditions to approach the system-wide isotope distribution predicted by mass-balance of added Fe(II) and goethite. Despite near-complete atom exchange between aqueous Fe(II) and goethite over 30 d, we saw stable Fe(II) concentrations in the aqueous phase after a rapid attainment of a net sorption equilibrium, and no noticeable changes in Fe oxide morphology or mineralogy. In order to explain these seemingly incongruent observations, we invoked a similar mechanism of bulk electron conduction through goethite, linking spatially distinct sites of Fe(II) sorption-oxidation and Fe(III) reduction-release.

Our goal with this work is to probe the conduction mechanism implicated in Fe(II)-Fe oxide atom exchange by measuring the effect of particle size and pH on the rate and extent of exchange. In addition, we separated the goethite particles into operationally defined reservoirs used sequential acid extractions in order to track where the exchange was occurring and what portion of Fe(III) atoms were involved in Fe atom exchange.

Materials and Methods

Reagents

All reagents were ACS reagent grade or better and used as received, except for HCl which was further purified through sub-boiling distillation. Deionized water (> 18 MΩ-cm) was used to make all solutions, and was made anaerobic by sparging with N_2 gas. Ferric nitrate ($Fe(NO_3)_3 \cdot 9H_20$, Sigma-Aldrich), sodium bicarbonate ($NaHCO_3$, Sigma-Aldrich), and potassium hydroxide (KOH, Sigma-Aldrich) were used in goethite synthesis. Experimental buffer solutions were made from either 4-(2-hydroxyethyl)-1-piperazineethanesulfonic acid (HEPES, Sigma–Aldrich) and potassium bromide (KBr, Sigma–Aldrich) or acetic acid (Fisher). Aqueous Fe(II) stocks were prepared by dissolving ^{57}Fe metal (Chemgas, 96% ^{57}Fe) and isotopically-normal anhydrous ferrous chloride ($FeCl_2$, Sigma-Aldrich) in 0.5 M HCl, and combining separate stocks to yield a desired isotope distribution. Chemical reductive dissolution experiments were performed using L-ascorbic acid (Amresco). Reagents used in chemical Fe analyses were 1,10-phenanthroline (Sigma-Aldrich), hydroxylamine HCl (Sigma-Aldrich), ammonium acetate (Sigma-Aldrich), and ammonium fluoride (Acros).

Goethite Synthesis and Characterization

Synthesis procedures for goethite rods used in this study are described in Chapter 2. Briefly, the method of Burleson and Penn (*64*) was modified for preparation of goethite nanorods. $NaHCO_3$ (0.48 M, 500 mL) was added to 500 mL of 0.4 M $(Fe(NO_3)_3 \cdot 9H_20$ in a dropwise fashion to generate a ferrihydrite intermediate, which was microwaved to boiling and quickly cooled in an ice bath. After dialysis, the suspension pH was raised to 13 with 5 M NaOH and heated at 90 ºC for 24 hr to generate goethite nanorods. Goethite microrods were synthesized using the method of Cornell and Schwertmann, through quick addition of KOH to $Fe(NO_3)_3 \cdot 9H_20$ and heating for 60 hr at 60 ºC (*24*). These samples of goethite has been characterized and used in previous studies

(Chapters 2 and 3). X-ray diffraction (XRD) patterns of each sample did not display any peaks indicative of other Fe minerals. Specific surface areas as determined by N_2-BET measurements were 40 m^2/g and 110 m^2/g for goethite microrods and nanorods, respectively.

Fe Isotope Tracer Experiments

All experiments were carried out in an anaerobic glovebox equipped with multiple Pd-catalysts for oxygen scrubbing, and great care taken to prevent O_2 intrusion into the reactors during centrifugation. Glass vials and centrifuge tubes used for the tracer study were new and used as received. Fe(II) isotope tracer experiments were initiated using procedures described in Chapter 3. Briefly, 15 mL of a pH 7.5 HEPES or pH 5.0 acetic acid buffer solution was spiked to ~ 1 mM Fe(II) with an Fe(II) stock that had been enriched in ^{57}Fe ($\delta^{57/56}Fe$ = +840.43‰). After equilibrating for 1 hr, batch reactors were filtered with an 0.2-μm filter into a 30 mL Nalgene centrifuge tube and the initial Fe(II) concentration was measured. Goethite microrods or nanorods were added (30 mg, 2 g/L solids loading), and batch reactors were placed on an end-over-end rotator to mix in the dark for times ranging from 10 min – 30 d.

To sample ^{57}Fe(II) tracer experiments, reactors were sacrificed for separation into five operationally defined components. The ~15 mL aqueous phase of each batch reactor was separated by pelleting goethite solids through centrifugation at 30,000*g*, followed by decanting the supernatant into a syringe and filtering into a separate reactor before acidification. Proton-promoted dissolution of goethite is extremely slow at pH 5.0 and 7.5, so it was not surprising that mol fractions of Fe(II) in aqueous Fe extracts averaged 99% over the course of 30 d. Goethite solids were resuspended in 0.4 M HCl for 10 min to remove solid-associated Fe(II), and the centrifugation and filtration steps were repeated to isolate the aqueous phase, termed extract 1. Lowering solution pH in this manner should be sufficient to release all surface-associated Fe(II) back into the aqueous

phase without leaching much Fe(III) into solution (see footnotes, Tables 4.2 and 4.3). Successive acid extractions were performed in order to remove remaining Fe(II) and the most labile Fe(III) components, using different concentrations of HCl for nanorods and microrods (extractions 2 and 3, procedures listed in Table 4.1). Fe(II) recoveries were minor during these extractions, but did constitute a larger portion of total Fe recovered in microrod experiments because overall Fe recoveries were much smaller (see footnotes, Tables 4.2 and 4.3). The labile Fe(III) atoms recovered during extractions 2 and 3 could be surface Fe atoms, although we cannot say with certainty which goethite surfaces were more readily dissolved. Remaining goethite solids were completely dissolved in 4 M HCl.

Colorimetric Fe Measurements

Subsamples of aqueous solution and sequential extractions were analyzed for Fe(II) and Fe(III). Aqueous Fe(II) concentrations were determined using the phenanthroline method (*128*). Fluoride was added to remove potential interferences from aqueous Fe(III) (*106*). Fe(III) concentrations were determined by difference between aqueous Fe(II) samples and separate subsamples in which all aqueous Fe was reduced to Fe(II) with hydroxylamine HCl.

Fe Isotope Measurements

Prior to isotope analysis, all Fe samples were oxidized with hydrogen peroxide. Samples were purified using anion exchange chromatography and Fe isotopes were analyzed using a Micromass IsoProbe single focusing MC-ICP-MS according to previously established methods proven to be free of sample matrix effects (*93, Chapter 3*). Fe isotope compositions are expressed in delta notation:

$$\delta^{57/56}Fe\,(‰) = \left(\frac{\frac{^{57}Fe}{^{56}Fe}_{sample} - \frac{^{57}Fe}{^{56}Fe}_{std}}{\frac{^{57}Fe}{^{56}Fe}_{std}} \right) \times 1000 \qquad (1)$$

where $^{57}Fe/^{56}Fe_{std}$ is the average isotopic ratio for terrestrial igneous rocks (*92*). Based on replicate analyses of 33 samples passed through the entire analytical process, the average 1-standard deviation uncertainty is 0.13‰ in $^{57}Fe/^{56}Fe$.

Solids Characterization

Goethite solids had previously been characterized using x-ray diffraction (XRD), ^{57}Fe Mössbauer spectroscopy, and electron microscopy (Chapter 2). After reaction with aqueous Fe(II) for 30 d, selected reactors were sacrificed for solids characterization. Reactor contents were passed through a syringe filter housing equipped with a 0.45-µm removable filter disc, and solids were removed and rinsed with deionized water. For XRD analysis, solids were combined with a small amount of glycerol and the slurry was placed on a specimen holder and analyzed using a Rigaku Miniflex II equipped with a Co X-ray source. Separate samples were prepared for transmission electron microscopy (TEM) by placing rinsed solids on a carbon-coated Cu grid (Electron Microscopy Sciences). Images were collected using a JOEL JEM 1230 microscope and analysis of resulting images was performed with Image J software (http://rsbweb.nih.gov/ij/). Goethite samples intended for high-resolution electron microscopy (HR-TEM) were resuspended in ethanol to reduce particle aggregation and placed on a holey carbon grid (Electron Microscopy Sciences).

Reductive Dissolution Experiments

Procedures for reductive dissolution experiments were adapted from Postma (*129*). Goethite solids were mixed for 30 days in the presence or absence of 1 mM Fe(II) in accordance with the experimental protocol for isotope exchange experiments. Solids

were then collected and rinsed to remove residual aqueous Fe(II) through centrifugation and resuspension in HEPES buffer solution. To initiate dissolution experiments at pH 3, 10 mg of goethite solids were resuspended in 120 mL of 10 mM ascorbic acid (solids loading ~ 80 mg/L). Solution pH was adjusted to 3.0 ± 0.05 with dilute HCl, and crimp-sealed reactors were placed on an end-over-end rotator and covered with aluminum foil. Reductive dissolution experiments at pH 5.5 were started by adding 10 mg of goethite solids to 120 mL of 10 mM ascorbic acid plus 5 mM acetic acid, and adjusting solution pH with dilute HCl or NaOH. At periodic intervals, aliquots were withdrawn from reactors, filtered through 0.2-micron nylon filters, and analyzed for aqueous Fe(II). Experiments ran for roughly 100 hr to measure the initial rate of reductive dissolution.

Results and Discussion

Effect of Goethite Particle Size on Rate and Extent of Fe Atom Exchange

In our previous work with goethite nanorods (Chapter 3), we used Fe isotopes to track the movement of Fe between the aqueous phase and goethite microrods during a pH 7.5 batch Fe(II) sorption experiment. Aqueous Fe(II) was enriched with ^{57}Fe to give distinctly different isotopic compositions for the two reservoirs of Fe, aqueous Fe(II) and Fe(III) within the goethite structure. Enriched aqueous Fe(II) contained roughly twice as many ^{57}Fe atoms as would be expected in nature ($\delta^{57/56}Fe$ = +840.43‰). Goethite rods were not enriched and had an initial $\delta^{57/56}Fe$ value of -0.12‰. Enriching the aqueous Fe(II) with ^{57}Fe allowed us to track movement of Fe atoms between aqueous and solid phases by measuring the $\delta^{57/56}Fe$ of each phase over time with MC-ICP-MS.

To investigate whether goethite particle size influenced the rate and extent of atom exchange at pH 7.5, we conducted a similar isotope tracer experiment with larger goethite particles. Goethite microrods were ~ 4-7 times larger than the nanorods in length and width (Chapter 2), resulting in particles with ~ 100 times more interior volume than

goethite nanorods. The larger volume of microrods implies a longer average path-length for bulk conduction of electrons, which we suspected would impact rates of atom exchange if spatially distinct sites of Fe(II) oxidation and Fe(III) reduction were linked through a conduction mechanism.

Despite the significant increase in primary particle size, little difference in rate and amount of exchange was observed between goethite microrods and nanorods at pH 7.5 (Figure 4.1, top panel). At the onset of Fe isotope tracer experiments, each reactor contained roughly 354 micromoles of Fe distributed between the aqueous phase (≈ 16 μmoles) and solid phase (≈ 338 μmoles) (Tables 4.2 and 4.3). For complete exchange, an Fe isotope distribution can be calculated by summing the mass-balance weighted isotope distributions of initial aqueous Fe(II) and initial goethite Fe(III) added to the reactors, as follows.

$$\frac{[Fe_{aq,\,t=0}]x\ \delta^{57/56}Fe_{aq,\,t=0} + [Fe_{goeth,\,t=0}]x\ \delta^{57/56}Fe_{goeth,\,t=0}}{[Fe_{aq} + Fe_{goeth}]} = \delta^{57/56}Fe_{sys} \qquad (2)$$

$$\frac{15.85\ \mu mol\ x\ 840.43‰ + 337.66\ \mu mol\ x\ -0.12‰}{15.85\ \mu mol + 337.66\ \mu mol} = 37.57‰$$

As reported in our previous work, Fe isotope ratios for aqueous Fe(II) and goethite nanorods converged to similar values (39.94‰ and 38.75‰) after only 30 d of reaction at pH 7.5 suggesting that both reservoirs of Fe had become completely mixed (Table 4.2, Figure 4.1). Similar convergence was observed for the aqueous Fe(II) and goethite microrods, which reached 41.83‰ and 38.85‰ respectively (Table 4.3). Convergence of isotope ratios for aqueous Fe(II) and goethite microrods to a nearly uniform isotope distribution suggests that near-complete atoms exchange had also occurred between aqueous Fe(II) and goethite microrods (Table 4.3, Figure 4.1). There appeared to be little difference in the rates of atom exchange for the goethite nanorods and microrods, when comparing either aqueous phase or residual solids isotope ratios over time.

To quantify extent of atom exchange, we calculated percent exchange values based on progression of aqueous or residual samples towards the system-wide equilibrium $\delta^{57/56}Fe$ value (calculated in equation 2) (adapted from (*130*)):

$$\text{Percent Exchange (\%)} = \frac{100^* (\delta^{57/56}Fe_{meas} - \delta^{57/56}Fe_{initial})}{(\delta^{57/56}Fe_{sys} - \delta^{57/56}Fe_{initial})} \quad (3)$$

where $\delta^{57/56}Fe_{meas}$ represents observed isotope ratio in aqueous or residual extractions, $\delta^{57/56}Fe_{initial}$ is the starting isotope composition for aqueous Fe(II) or goethite Fe(III), and $\delta^{57/56}Fe_{sys}$ is the mass-balance weighted average isotope distribution calculated using equation 2. This method has been used to assess isotope exchange in a variety of systems (e.g., *131, 132*). At pH 7.5, both goethite nanorods and microrods rapidly approach 100% exchange over 30 d (Figure 4.2 and Table 4.4). Similar amounts of exchange values are estimated regardless of whether data from aqueous phase or residual goethite Fe(III) is used in equation 3. Similar to untreated isotope ratios in Figure 4.1, there appears to be little difference in the rates of atom exchange between goethite nanorods and microrods when plotted as percent exchanged.

At pH 7.5, both the extent and rate of atom exchange between aqueous Fe(II) and goethite do not appear to be significantly influence by the primary goethite particle size implying that bulk electron conduction is not limiting the rate of Fe exchange. Recent estimates of electron transfer rates in Fe oxides (*125*) which indicate bulk electron transfer between Fe oxide particles of this size would be much more rapid than our experimental timescales of days or weeks. Molecular simulations of electron transfer in hematite are more prominent in the literature, but bulk conductivity of hematite and goethite has been demonstrated to be reasonably similar (*113*). Larger goethite microrods, despite a 100-fold increase in internal volume, could still facilitate conduction through every single solid phase Fe atom in timescales that would be indistinguishable from nanorod conduction rates, using our experimental approach.

If electron conduction through bulk Fe oxides is not limiting rates of Fe atom exchange, another process must be controlling overall reactivity. When we consider the entire mechanism to be a multi-step reaction comprised of Fe(II) sorption-Fe(II) oxidation-electron transfer-Fe(II) dissolution, some of these individual processes occur at the oxide-water interface. Behaviors involving reactive surface area accessible to the aqueous phase, such as particle aggregation, could be important controlling factors when considering macroscopic atom exchange data. In previous work with these goethite particles, it was noted that observed net interactions with Fe(II), such as Fe(II) sorption isotherms, were more similar than might be predicted due to their large difference in size and BET-specific surface areas. Overall similarities in observed reactivity with Fe(II) were explained by increased aggregation of goethite nanorods at pH 7.5, such that the active surface areas of the two goethite size fractions at pH 7.5 were more similar than predicted by dry powder BET surface area measurements (Chapter 2). At pH 7.5, roughly 50% of the initial aqueous Fe(II) was removed from solution when exposed to goethite nanorods (from 15.85 μmol initially to ~ 8 μmol, Table 4.2), while only 30% of initial Fe(II) (15.84 to ~11 μmoles remaining in solution, Table 4.3) was removed by microrods. This difference of 50%/30% = 1.7 is less than would be expected, based upon the surface area difference of 110 m^2g^{-1} / 40 m^2g^{-1} = 2.75 for nanorods and microrods, respectively. It is reasonable to expect that aggregation could also influence atom exchange between aqueous Fe(II) and goethite, since electron transfer between solid-associated Fe(II) and accessible Fe(III) or Fe(II) detachment from surface sites are surface-mediated processes.

Goethite solids were also examined after reaction with aqueous Fe(II) in order to determine if any noticeable changes to the solid phase could be detected as a result of atom exchange between aqueous Fe(II) and solid Fe(III). XRD patterns indicate no formation of secondary Fe phases after reaction of Fe(II) for both nanorods and microrods (Chapter 3 and Figure 4.3). ^{57}Fe Mössbauer spectroscopy also indicated that goethite was the only Fe phase present before and after reaction with Fe(II) (Figure 4.4).

In a similar experiment using isotopically normal goethite and aqueous Fe(II) enriched in ^{57}Fe, we observed slight differences in the magnetic ordering of goethite before and after reaction with Fe(II). Microrods reacted with Fe(II) appear to show less inner-line broadening characteristic of disordered crystallinity. Potential morphology changes as a result of Fe atom exchange were examined with TEM. In Chapter 3, we observed no noticeable changes in shape or size of in nanorod particle before and after reaction with Fe(II). Microrods behaved similarly, with no statistically significant difference in observed particle dimensions after 30 d of reaction with 1 mM Fe(II) , as determined by the student's t-test. ($p = 0.297$ or 0.260 for length and width, respectively) (Figure 4.5 and Table 4.6). Based on initial HR-TEM images, we speculated in Chapter 3 that reaction with aqueous Fe(II) may have made the goethite rods more crystalline. More extensive HR-TEM imaging of goethite rods, however, has revealed no consistent differences in crystallinity before or after reaction with aqueous Fe(II). Different crystal faces were observed in different particles, but the proportion of visible (110) surfaces or (301) surfaces was similar in unreacted and Fe(II)-reacted goethite samples and no indications of preferential growth or dissolution at a specific crystal faces was observed.

To test whether goethite particles were more crystalline before or after reaction with Fe(II), we compared rates of goethite dissolution. Rates of chemical reductive dissolution by ascorbic acid at pH 3.0 were nearly identical for goethite particles that had been mixed for 30 d in the presence or absence of Fe(II) (Table 4.5). Goethite nanorods dissolved faster than goethite microrods, but the 2.74-fold increase in rate can be attributed to the difference in specific surface areas (110 m^2/g and 40 m^2/g) between the two goethite particle sizes. At pH 3.0, it is reasonable to expect goethite nanorods to exist primarily as individual particles, based on our previous electron microscopy, and dynamic light scattering results studies with these particles conducted at pH 2.0 (Chapter 2), so accounting for surface effects in aqueous systems by incorporating dry-powder BET values would seem to be an appropriate evaluation in this case.

No observable differences in solid-phase characterization could be detected between goethite reacted with aqueous Fe(II) for 30 d and unreacted goethite, despite evidence from isotope tracer studies suggesting that extensive exchange had occurred in reacted samples. This general observation agrees with our previous work demonstrating homoepitaxy after reaction of Fe(II) with goethite (*11, Chapter 2*). Goethite nanorods and microrods both exchanged a majority of their initial Fe(III) atoms with aqueous Fe(II), as measured by stable Fe isotope data, but this result was achieved in a manner that preserved the initial solid phase morphology, such that nanorods remained nanorods and microrods remained microrods (Table 4.6). A surface-mediated process linking separate sites of Fe(II) oxidation and Fe(II) dissolution with bulk electron conduction may explain these observations.

Recent studies with hematite have observed preferential growth and dissolution at specific crystal faces, providing clear visual evidence for a bulk conduction pathway. These hematite surfaces were relatively large, well-ordered and free of surface detects, which would allow crystal face observations to be clearly expressed in solid phase characterization. The same traits cannot be attributed to either sample of goethite we used in this study – relatively small particles that were prepared without surface-cleaning annealing steps. We reason that on particles of this scale, surface disorder could provide enough difference between Fe surface sites to drive bulk conduction between spatially distinct surface sites. Recent modeling simulations of electron transfer in hematite predict significantly different rates of Fe(II)-Fe(III) electron transfer depending on the local environment and coordination of Fe atoms, which are can be expressed in differences between crystal faces, or edge and surface defects (*125*). Electrons are conducted more efficiently between well-coordinated atoms and are more likely to be "trapped" at less-coordinated corner or defect sites. Although we cannot probe atomic-scale surface changes in individual goethite, it is reasonable to expect that a variety of surface sites exist on our goethite rods. Preferential electron transfer at certain sites would lead to

oxide growth, and electron trapping sites could be prone to Fe(II) detachment, creating a scenario in which constantly changing surface characteristics stimulate electron conduction between momentary potential gradients existing between surface sites.

Influence of Solution pH on Atom Exchange

Experiments at pH 5.0 display different behavior with regards to net Fe(II) sorption. At pH 5.0, no net sorption of Fe(II) is observed over 30 d, regardless of goethite particle size (Tables 2 and 3). This observation is consistent with previous work, and is typical of pH-dependent association of cations with oxide surfaces (Chapter 2, e.g., *133*). Despite no measurable uptake of aqueous Fe(II) in the presence of goethite, isotope ratios for aqueous Fe(II) changed significantly over the course of the experiment, as did $\delta^{57/56}$Fe values for residual goethite solids (Figure 4.1, lower panel and Tables 4.2 and 4.3). $\delta^{57/56}$Fe values for the aqueous phase dropped from the initial starting value of 840.43‰ to 338.99‰ and 597.15‰ for nanorods and microrods, respectively, which indicates that aqueous phase Fe became less enriched in ^{57}Fe after 30 d. Conversely, isotope ratios increased from ~ 0 to 20.01‰ and 10.76‰ for nanorods and microrods, respectively, indicating accumulation of ^{57}Fe in the solid phase. Changes in goethite Fe(III) isotope ratios are less drastic than aqueous phase isotope ratios because aqueous Fe(II) is the minor phase on a mass-basis, and was consequently furthest from the system-wide equilibrium value of ~37.6‰.

When experimental isotope data at pH 5.0 are viewed in terms of their progression towards complete isotope exchange using equation 3, calculated % exchange values for aqueous phase Fe(II) or residual Fe(III) solids are quite similar, despite the large differences in absolute movement of $\delta^{57/56}$Fe values in each of the two extractions (Figure 4.2, bottom panel and Table 4.4). Using equation 3, goethite nanorods appear to have achieved ~ 60 % isotopic equilibration with enriched ^{57}Fe(II), while goethite microrods are closer to 30% equilibration after 30 d.

The extent of change in measured $^{57}Fe/^{56}Fe$ isotope ratios in aqueous and solid-phase Fe at a solution pH of 5.0 was surprising, given that no measureable uptake of Fe(II) was observed. Aqueous Fe(II) cations could still be interacting at the mineral surface, however, donating electrons into the bulk Fe(III) oxide, and eventually producing reduced Fe(II) at another surface site, where Fe(II) detachment would be strongly favored due to surface protonation at pH 5.0. In this manner, atom exchange could occur in a fashion that is rapid enough to produce no net loss of aqueous Fe(II) from solution. Rates of exchange would then be controlled by the probability of Fe(II) interaction with the Fe oxide surface, which is understandably lower at pH 5.0.

Considering either untreated $\delta^{57/56}Fe$ values or their translation into % equilibration values through equation 2, it is apparent that at pH 5.0, noticeable differences exist in the rates of atom exchange observed in the nanorod and microrod systems. This is most easily seen in aqueous phase $\delta^{57/56}Fe$ measurements, which are much lower after 30 d of reaction with goethite nanorods than goethite microrods. If we reason that bulk electron conduction is much too fast to be rate-limiting in these systems, we must think about potential reasons for observed differences in rates of atom exchange between nanorods and microrods at pH 5.0. As mentioned previously, perhaps surface-dependent components of redox-driven atom exchange may explain our results.

We have previously shown that macroscopic Fe(II) uptake in these two goethite samples can be explained by aggregation effects at pH 7.5. Goethite nanorods aggregate more thoroughly at pH 7.5, resulting in particle complexes with sizes comparable to clusters produced by goethite microrods (Chapter 2). At a much lower solution pH of 2.0, particles remain unaggregated. At a solution pH of 5.0, it is reasonable to think goethite nanorods exist somewhere in the middle of the continuum between tightly bound aggregates and free primary particles, which would diminish effects of aggregation on our experiments. Although measurements were not made on these goethite particles, a majority of synthetic goethites have reported point of zero charge (pzc) values between

pH 7 and 8.5 (*134*), which would suggests that a 2.5 unit pH shift from 7.5 to 5.0 could be enough to stabilize primary particles in solution.

Interestingly, if the approach to 100 % exchange in seen Figure 4.2 is fit with a first-order exponential, the average rate constant of exchange (averaging the rate calculated from aqueous phase data and goethite Fe(III) data) is 0.0343 ± 0.009 d^{-1} for nanorods and 0.0126 ± 0.001 d^{-1} for microrods. This represents a ~ 2.73-fold increase in the measured equilibration rate for the nanorods compared to the microrods, which is almost identical to the 2.75-fold increase in BET surface areas (110 m^2/g and 40 m^2/g) between the two particle sizes. This observation suggests that reactive particle surface area is an important consideration in atom exchange between Fe(II) and goethite. At a solution pH of 5.0, aggregation effects are not as important in accounting for the behavior of our goethite particles. Rates of redox-driven atom exchange between Fe(II) and goethite could be different at pH 5.0 for goethites with a different primary particle size, because the surface-mediated rate-controlling steps in this process (Fe(II) oxidation, Fe(II) detachment) are not inhibited by particle aggregation.

Atom Exchange in Different Fe Components

To gain additional insights into the interaction of aqueous Fe(II) with goethite Fe(III), we sequentially extracted each reactor during sampling. Extraction procedures separated the Fe(II)-goethite suspension into five operationally defined components: aqueous Fe(II), solid-associated Fe(II) (extract 1), two extractions of labile Fe(III) (extracts 2 and 3), and Fe(III) from bulk goethite solids. For pH 7.5 trials, a majority of Fe(II) lost from solution during net Fe(II) sorption was recovered during extraction #1. No net Fe(II) uptake was observed at pH 5.0; as a result, extract #1 recovered only trace levels of Fe in reactors buffered at pH 5.0. Despite using a lower HCl concentration to extract labile Fe(III)from the nanorods than microrods (1 M vs. 1.75 M respectively), Fe(III) recoveries were usually an order of magnitude higher for the nanorods (Tables 2

and 3). Fe(III) recoveries in extracts 2 and 3 would still amount to less than one complete monolayer of surface Fe in either case, assuming simple geometric approximations of a goethite rod and an average Fe-Fe distance of 0.33 nm in the goethite structure (*24*).

Isotope ratios of the five operationally defined sequential extractions reveal interesting behavior (Figure 4.6). At pH 7.5, all five sequential extractions trend towards the system-wide $\delta^{57/56}$Fe value of 37.57‰ or 37.77‰ for nanorods or microrods over the course of 30 d (Tables 2 and 3). Extract 1, containing primarily solid-associated Fe(II), had isotope ratios much lower than aqueous phase Fe(II) after 10 min of reaction, but $\delta^{57/56}$Fe values for aqueous Fe(II) and extract 1 were similar after a few hours and remained similar for the duration of the experiment. In the first few days of reaction, extracts 2 and 3 were also enriched in ^{57}Fe, actually rising above the predicted system wide $\delta^{57/56}$Fe value before decreasing towards that endpoint with the other extracts (Figure 4.6, top row).

Reactors buffered at pH 5.0 show somewhat different trends in sequential extraction data. As mentioned before, extract 1 was designed to remove sorbed Fe(II), and therefore was almost devoid of Fe in these experiments, which saw no net Fe(II) sorption. Extracts 2 and 3 become enriched in ^{57}Fe to an extent exceeding system-wide mass balance averages of ~ 37.6‰, as was the case at pH 7.5. However, extracts 2 and 3 are even more enriched in ^{57}Fe than comparable data points at pH 7.5, and appear to be increasing in ^{57}Fe content even after 30 d (Figure 4.6, bottom row). Goethite microrods have labile Fe(III) that is significantly more enriched in ^{57}Fe than goethite nanorods, despite aqueous Fe(II) and residual solids data indicating that overall, goethite nanorods had achieved a higher % equilibration with aqueous Fe(II) after 30 d (Figure 4.2, bottom panel)

A qualitative comparison of sequential extraction data, coupled with our existing knowledge of the redox-driven atom exchange mechanism, can provide insights about

relative rates of individual processes. We can envision 5 general processes contributing to redox-driven atom exchange between aqueous Fe(II) and Fe oxides.

Fe(II) sorption: $$*Fe(II)_{aq} \xrightarrow[K2]{K1} *Fe(II)_{sf} \quad \text{(R1)}$$

Interfacial electron transfer: $$*Fe(II)_{sf} + Fe(III)_{sf} \xrightarrow[K3]{} *Fe(III)_{sf} + Fe(II)_{sf} \quad \text{(R2)}$$

Electron transfer into bulk: $$Fe(II)_{sf} + Fe(III)_{bk} \xrightarrow[K4]{} Fe(III)_{sf} + Fe(II)_{bk} \quad \text{(R3)}$$

Conduction to surface site: $$Fe(II)_{bk} + Fe(III)_{sf} \xrightarrow[K5]{} Fe(III)_{bk} + Fe(II)_{sf} \quad \text{(R4)}$$

Fe(II) detachment: $$Fe(II)_{sf} \rightarrow Fe(II)_{aq} \quad \text{(R5)}$$

In reactions R1-R5, "^{57}Fe" denotes atoms initially from the enriched ^{57}Fe aqueous phase, as opposed to Fe atoms initially from within goethite. In this manner, we can distinguish four main subcomponents of the Fe(II)-goethite system – aqueous Fe(II) ($Fe(II)_{aq}$), surface associated Fe(II) ($Fe(II)_{sf}$), surface Fe(III) ($Fe(III)_{sf}$), and bulk Fe(III) ($Fe(III)_{bk}$), although each "reservoir' of Fe will eventually be composed of Fe atoms from both of the initial starting fractions – enriched ^{57}Fe(II) spike, and goethite solids. Bulk Fe(II) ($Fe(II)_{bk}$) will be considered a transient species due to inability to detect Fe(II) within bulk solids, and due to rapid rates of bulk electron conduction as described previously (*125*). Each of the five expressions listed would proceed with an individual overall rate constant K1-K5. We can examine our experimental data in this context in order to determine relative rates contributing to the overall process of atom exchange in goethite.

At a solution pH of 7.5, net Fe(II) uptake from solution is already complete at the 10 min sampling time, resulting in a stable surface associated Fe(II) ($Fe(II)_{sf}$) population. For this reason, net Fe(II) sorption is assumed to proceed very rapidly, and we will begin our analysis by considering an already stable $Fe(II)_{sf}$ concentration. To preserve stable amounts of $Fe(II)_{sf}$ and $Fe(II)_{aq}$ over our 30 d timecourse, rates of Fe(II) sorption and detachment (K1 and K5) must be very similar. After 10 min of interaction, $Fe(II)_{sf}$ – as measured by extract 1 – contains a nearly equivalent distribution of Fe atoms initially

from goethite and from the enriched Fe(II) spike, based on $\delta^{57/56}$Fe values ~ 350‰ for nanorods and microrods. Two potential avenues for generation of $Fe(II)_{sf}$ exist, according to this reaction scheme. Interfacial electron transfer, as governed by equation R2, could have achieved ~ 50% completion after 10 min, generating a sizable population of $Fe(II)_{sf}$ from goethite Fe atoms. If electron transfer from $Fe(II)_{sf}$ to bulk Fe(III) (i.e., equation R3 and reaction rate K3) was significantly slower than interfacial electron transfer (K2), this would result in a stable $Fe(II)_{sf}$ population. A similar effect has been proposed to occur between surface and bulk layers of hematite (*125*). Equation R2 is not the only potential source of $Fe(II)_{sf}$, however, as bulk conduction through the oxide (R4) also generates $Fe(II)_{sf}$ atoms. If equation R3 were *faster* than equation R2, $Fe(II)_{sf}$ could be stabilized after bulk conduction (R4), which will generate $Fe(II)_{sf}$ as rapidly as reactants for R4 are established. Experimental data from extracts 2 and 3 can provide guidance in assessing relative magnitudes of rate constants K2 and K3. Fe(III) recovered in these extracts suggests an accumulation in enriched ^{57}Fe(III) over timescales of a few days. In order for $^{57}Fe(III)_{sf}$ to increase in our reaction scheme, interfacial electron transfer (R2) must initially be faster than electron transfer into the bulk (R3), since R3 simply regenerates isotopically-normal $Fe(III)_{sf}$.

Evidence based on aggregation of primary particles suggests that reactions R1 and R5 could be rate-limiting at pH 7.5, due to their dependence on exposed surface area. Additional data considering overall Fe flux rates from goethite solids also points to Fe(II) detachment as a rate-limiting consideration. Adopting the method of Jang and Brantley (*135*) we characterized our data in term of Fe flux rates from the mineral surface. In order for complete atom exchange to occur over 30 d, an Fe mass equivalent to the original Fe(III) content of a primary particle must have moved through the particle surface area, for "complete turnover" of Fe atoms in our system. Deriving Fe flux rates from these considerations, we find that Fe(II)-dependent atom exchange at pH 7.5 involves Fe flux rates quite similar to the maximum Fe flux rate assumed possible at these solution

conditions (Figure 4.7). Maximum theoretical flux rates were estimated by analyzing wustite dissolution over a range of solution conditions, which was more rapid than an extensive survey of Fe oxide flux rates from a variety of dissolution studies, and was determined to be limited by Fe(II) detachment from mineral surfaces. If calculated Fe flux rates in our experimental system correspond to maximum Fe flux rates, limited by Fe(II) detachment, Fe(II) detachment (R5 and rate K5) may be limiting Fe(II)-Fe(III) atom exchange as well. Because K5 and K1 should be equivalent in order to preserve stable Fe(II) concentrations, our analysis of relative reaction rates at pH 7.5 indicates that K4 > K2 > K3 > K1 = K5.

At pH 5.0, important differences in experimental Fe isotope data can guide our rate comparison. An important constraint in this system is the absence of net Fe(II) uptake from solution, which implies no net accumulation of Fe(II) at the mineral surface. Isotope measurements of aqueous Fe and residual goethite indicate Fe(II)-goethite atom exchange is proceeding more slowly than at pH 7.5, but redox transformations are still occurring between Fe reservoirs. Extracts 2 and 3 at pH 5.0 suggest that labile Fe(III) is becoming more enriched in ^{57}Fe than at pH 7.5, despite the overall slowdown in exchange. Taken together, these observations must be the result of a change in relative rates of reaction for individual processes R1-R5. Interfacial electron transfer must still be occurring, but processes removing Fe(II) from surface or solid Fe reservoirs must be relatively rapid overall, in order for surface-bound Fe(II) to exist only as a transient species. $^{57}Fe(III)_{sf}$ is still accumulating after 30 d, suggesting that K2 is still larger than K3 at pH 5.0. Reaction R2 also produces $Fe(II)_{sf}$ species, which suggests that accumulation of Fe(II) at this stage could be slowed by a marked decrease in K1. In this manner, ^{57}Fe(III) would still be produced, but any $Fe(II)_{sf}$ generated would be shuttled through subsequent R3-R5 reactions at a rate that would eject Fe(II) from the solid structure much larger than Fe(II) could be incorporated through R1. Alternatively, $Fe(II)_{sf}$

produce during reaction R2 could immediately be detached from the particle surface, "short-circuiting" the 5-step reaction mechanism.

Intrinsic effects of decreased solution pH in this case (different buffer system, increased surface protonation, etc.) could also alter R2, R3 and R5 in ways that could alter their absolute and relative rates. For instance, increased surface protonation could make Fe(II) detachment R5 favorable relative to bulk electron injection (R3), or it could increase the rates of both reactions. Electron transfer between bulk Fe atoms would not seem to be affected by changing solution conditions, but the endpoint of R4 (an electron becoming "trapped" at a new surface Fe site) could have an increased driving force due to relative thermodynamic stability of Fe(II) at lower coordination surface sites (*24*). Additional molecular simulation studies are required to quantify these more subtle effects of changing solutions conditions. Regardless of these effects, it appears Fe(II) attachment as described by reaction R1 is rate-limiting in this case, due to lowered overall atom exchange and absence of surface-associated Fe(II). Fe(II) impingement upon the goethite surface could certainly be lower at pH 5.0 than at pH 7.5, as surface protonation will create less desirable binding sites for aqueous Fe(II). Whether the overall reaction proceeds through the 5-step mechanism or the "short-circuit" mechanism of Fe(II) attachment-interfacial electron transfer-Fe(II) detachment is still open to debate, and is currently being explored with additional Fe isotope tracer experiments conducted over long experimental time scales.

Considerations of Fe flux at pH 5.0 were performed by using first order rate coefficients for % atom exchange data detailed previously in section 3.2. Fe flux estimates at pH 5.0 indicate a similar trend in flux capacity for Fe(II)-goethite atom exchange at pH 5.0 as conventional chemical reductive dissolution (Figure 4.7), falling in line with chemical reductive dissolution fluxes calculated from ascorbic acid dissolution at pH 3.0 and 5.5. This data is in contrast to calculated Fe flux capacity at pH 7.5, which increases to an extent not predicted by normal typical reductive dissolution mechanisms.

This suggests that in the presence of aqueous Fe(II), increasing solution pH, resulting in greater net Fe(II) association with the oxide surface, will stimulate levels of Fe cycling far greater than expected from considerations of typical reductive dissolution.

Conclusions

We have taken important experimental steps to probe the mechanism of Fe(II)-goethite atom exchange, expanding on a stable Fe isotope tracer approach that has proven useful in previous studies. By varying goethite particle size and solution pH and observing shifts in isotope ratios in several operationally-defined Fe components over the course of 30 d, we have improved our understanding of how individual Fe-Fe interactions my contribute to redox-driven atom exchange between Fe(II) and goethite. It appears as though Fe(II) association to the goethite surface is rate-limiting, and is influenced by macroscopic processes controlling reactive surface area in aqueous media. At pH 7.5, complete atom exchange is observed between Fe(II) and goethite microrods or nanorods, and Fe flux rates measured with stable isotope analysis are comparable to maximum Fe flux rates for Fe solids. As noted in Chapter 2, such extensive Fe cycling could not be observed with traditional methods of aqueous or solid phase characterization. Increased Fe cycling has the potential to impact several important processes, including heavy metal mobilization from co-precipitated Fe oxide deposits and labile Fe availability as a nutrient in biological systems. Studies examining redox-driven Fe atom exchange in a variety of systems, and subsequent impacts on key biogeochemical processes, should be performed to assess the importance of this mechanism in natural settings.

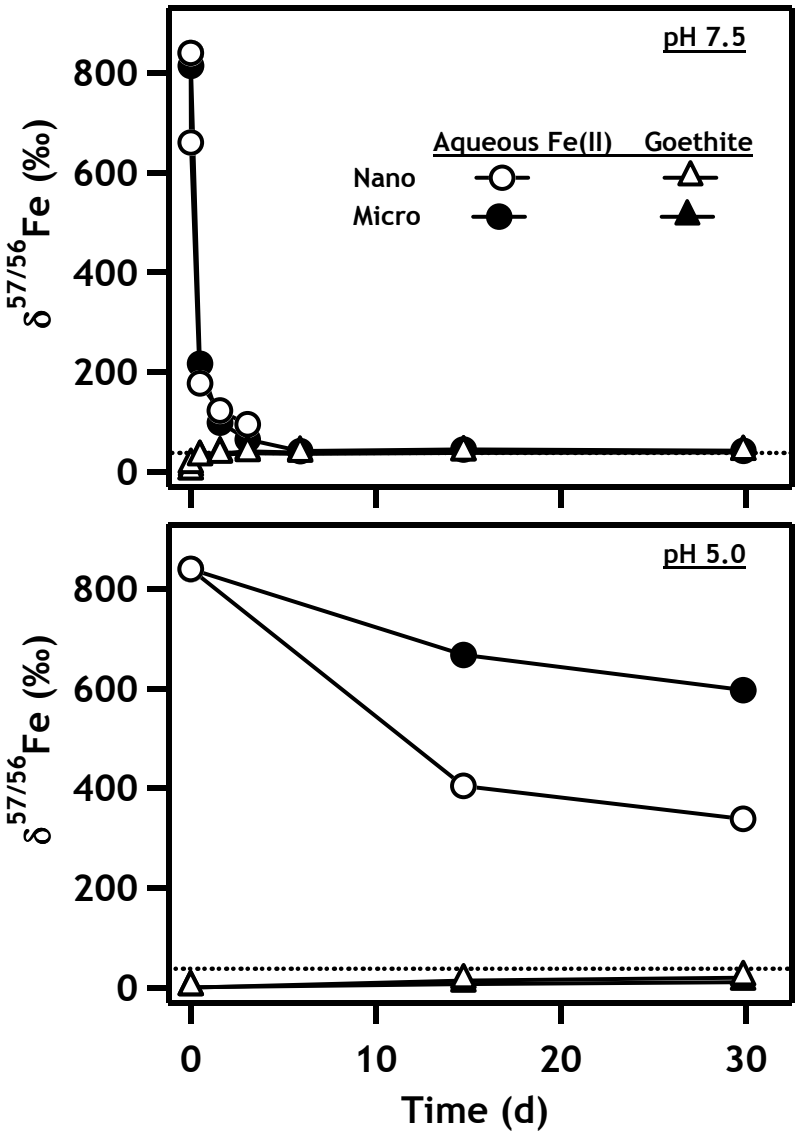

Figure 4.1 Measured $\delta^{57/56}$Fe values for aqueous Fe(II) and Fe(III) in residual goethite nanorods and microrods, in pH 7.5 and 5.0 suspensions over 30 d. Dashed lines in each panel represent the delta value predicted by complete isotopic exchange. 1-standard deviations of isotope ratios are contained within the margins of data markers.

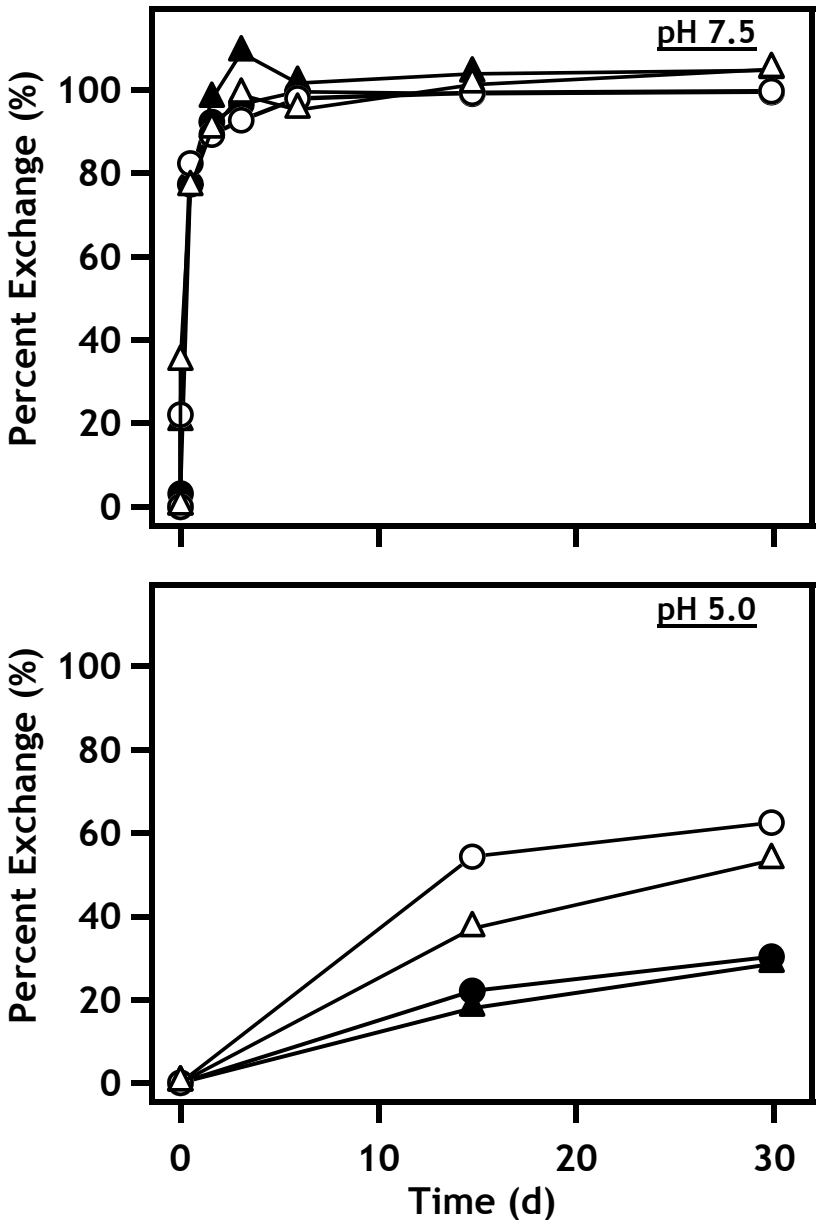

Figure 4.2 Percent Fe atom exchange for aqueous Fe(II) and residual goethite solids over the course of thirty days. Markers reflect Fe fractions as listed in Figure 4.1 (nanorods as open markers, microrods as filled markers). Error bars reflect 1-standard deviations of duplicate or triplicate reactors, and are contained within the margins of data markers when not visible. Percent exchange was calculated from equation 3 in the text.

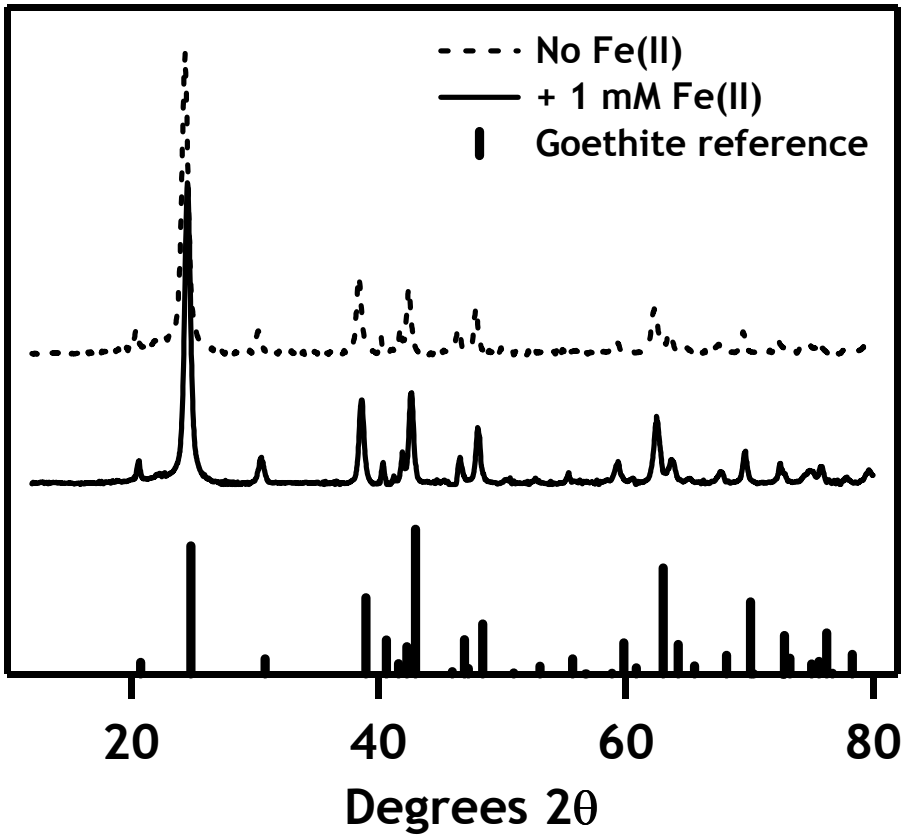

Figure 4.3 X-ray diffraction patterns for goethite microrods mixed for 30 d in the presence (——) or absence (- - - -) of 1 mM Fe(II). Goethite reference XRD pattern is displayed below experimental patterns.

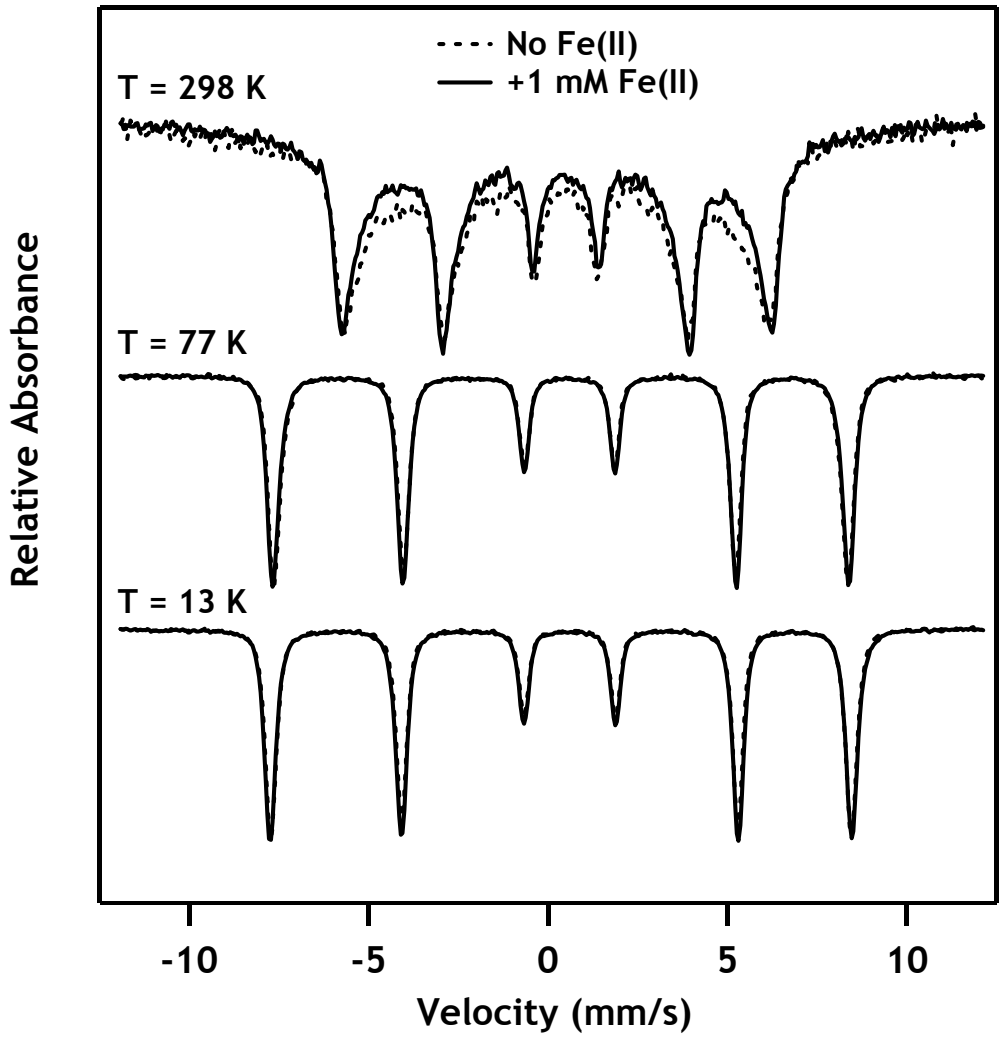

Figure 4.4 ^{57}Fe Mössbauer spectra of goethite microrods mixed for 30 d at pH 7.5 in the presence (——) and absence (-----) of 1 mM aqueous Fe(II). Spectra were collected at room temperature (298 K), 77 K, and 13 K. Spectral intensities were normalized using the absorbance at the leftmost peak in order to compare relative changes in absorbance between the two reaction conditions. Spectral fitting of 13 K data confirms the presence of goethite as the sole Fe phase in each case (center shift = 0.49 mm/s, quadrupole □□□□□□□□□□□□□□□□□□□□Ī□□□ hyperfine field = 50.3 T).

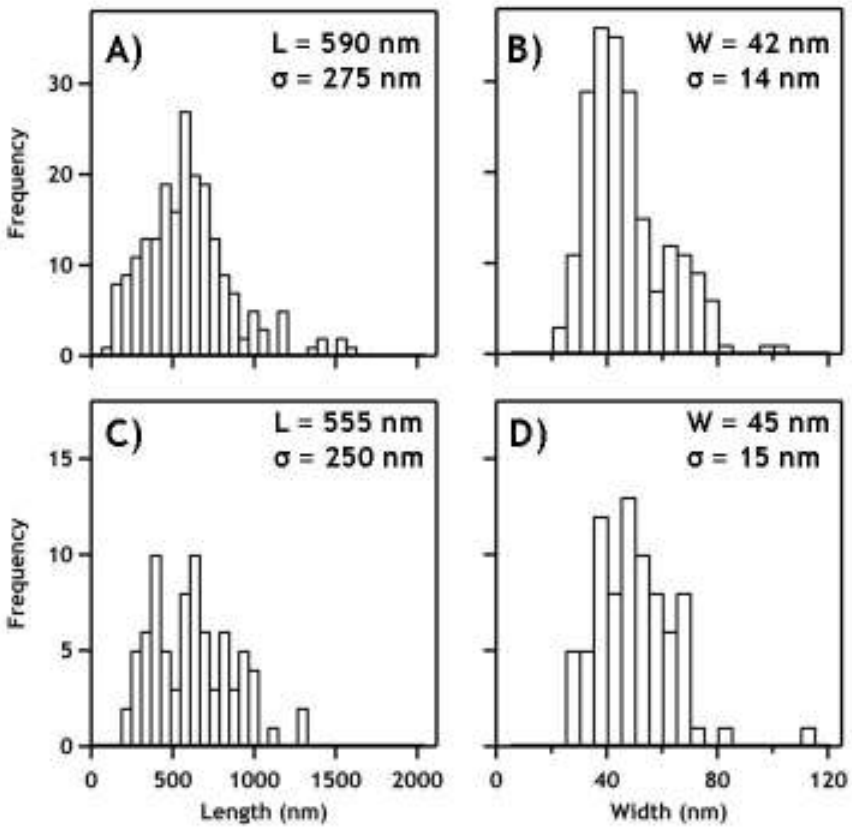

Figure 4.5 Histograms of observed particle length (L) and width (W) for goethite microrods before and after reaction with 1 mM Fe(II). Average measurements are included in each panel, along with 1-standard deviations (σ) for each distribution. A greater number of particles were included in the analysis of unreacted microrods (Panels A and B) than for particles reacted for 30 d with 1 mM Fe(II) (C and D), due to the fact that particle aggregation made it more difficult to find unobstructed rods. Unreacted goethite microrod histograms were compiled using data from TEM images only, which resulted in different average particle lengths as compared to Chapter 2, which used a combination of TEM and SEM images.

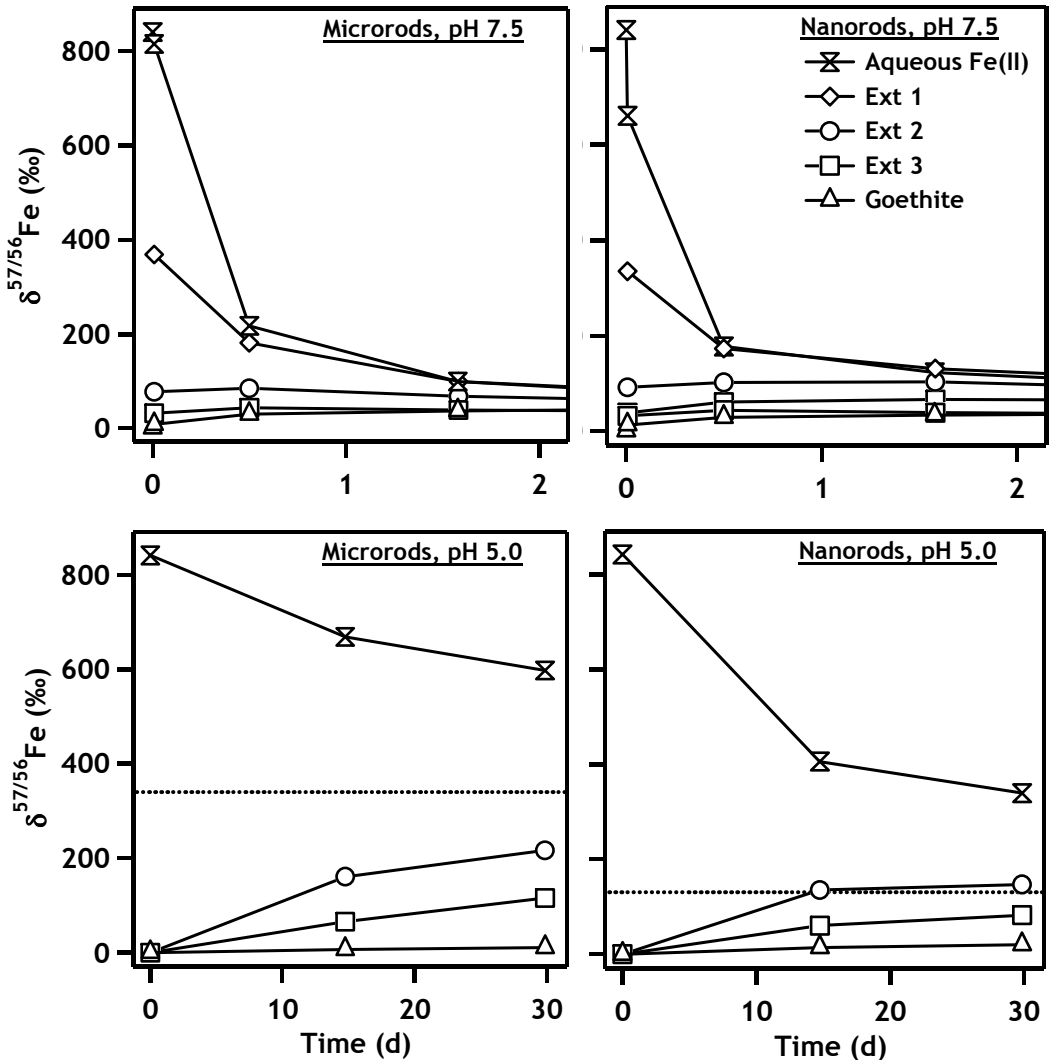

Figure 4.6 Measured $\delta^{57/56}$Fe values of sequential extractions performed on goethite solids after removal of aqueous Fe(II). Data collected at pH 7.5 (top row) is only displayed for the first 2 d to illustrate the initial gradient of ^{57}Fe that is observed in the experiment, showing a progression in $\delta^{57/56}$Fe of Aqueous Fe(II) > Ext 1 > Ext 2 > Ext 3 > Residual goethite solids. Extract 1 contained primarily sorbed Fe(II), and therefore was not applicable in the pH 5.0 trials (bottom row). Dashed lines (bottom row) indicate alternate equilibrium mixing lines for surface Fe(III) atoms (as opposed to all Fe(III) atoms) and aqueous Fe(II), which could explain observed data trends at pH 5.0 (see discussion in text).

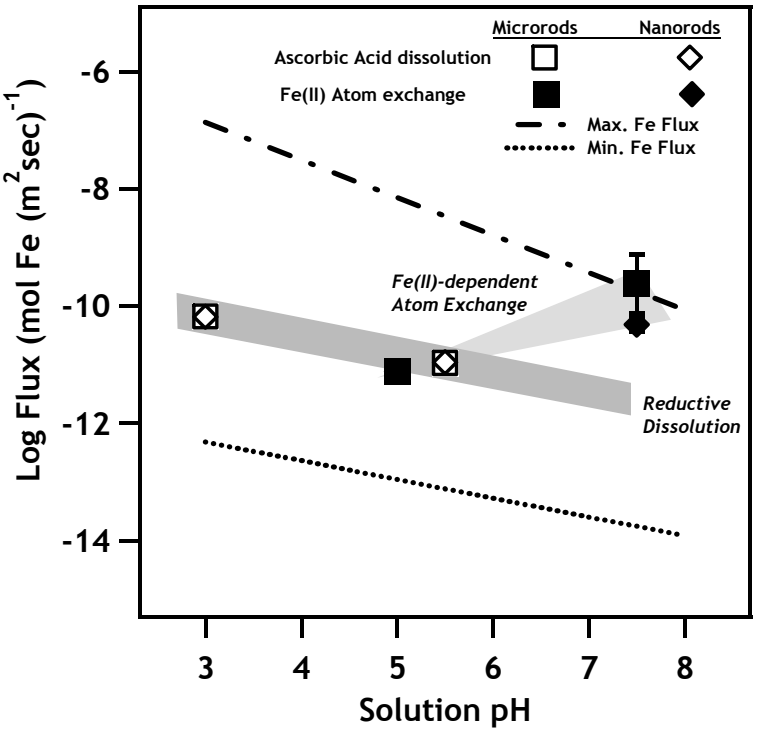

Figure 4.7 Measured Fe fluxes in goethite experiments at different solution conditions during the present study. Dashed lines represent the theoretical maximum and minimum Fe flux rates, described by wustite (FeO) dissolution and proton-promoted dissolution, respectively, as outlined in Brantley (2009). Open data markers indicate results of ascorbic acid dissolution trials at pH 3.0 and 5.5, while dark markers indicate Fe flux rates derived from isotope exchange measurements at pH 5.0 and 7.5.

Table 4.1 Summary of Fe extraction procedures for ^{57}Fe(II) isotope tracer study.

Sample	Extraction 1	Extraction 2	Extraction 3	Residual Solids[a]
Nanorods	0.4 M HCl 10 min, RT[b]	1 M HCl 45 min, 60 ºC	1 M HCl 45 min, 60 ºC	4 M HCl 4+ hr, 60 ºC
Microrods	0.4 M HCl 10 min, RT	1.75 M HCl 45 min, 60 ºC	1.75 M HCl 45 min, 60 ºC	4 M HCl 4+ hr, 60 ºC

[a]- All remaining goethite solids were completely dissolved in the final extraction.

[b]- Room temperature (RT).

Table 4.2 Chemical and isotopic data during enriched Fe(II) isotope tracer experiment with goethite nanorods.

	Aqueous Fe(II)		*Residual Fe(III)*		*Extract 1*		*Extract 2*		*Extract 3*	
Time (d)	Fe content (µmol)	$\delta^{57/56}$Fe (‰)	Fe content[c] (µmol)	$\delta^{57/56}$Fe (‰)	Fe content[d] (µmol)	$\delta^{57/56}$Fe (‰)	Fe content[e] (µmol)	$\delta^{57/56}$Fe (‰)	Fe content[f] (µmol)	$\delta^{57/56}$Fe (‰)
pH 7.5										
0.00	15.85 (0.46)[a]	840.43 (0.18)	337.66 (3.4)	-0.12 (0.02)						
0.007	8.17 (0.17)	660.64 (13.21)	332.96 (0.18)	12.71 (0.16)	7.84 (0.11)	334.65 (13.59)	10.32 (1.48)	91.55 (7.37)	10.83 (0.81)	38.25 (1.83)
0.50	7.70 (0.06)	176.95 (10.60)	278.27 (8.37)	28.25 (0.19)	7.84 (0.13)	172.94 (9.29)	9.20 (1.32)	101.76 (6.95)	10.71 (0.36)	60.61 (3.20)
1.58	8.48 (0.12)	122.36 (2.50)	263.82 (8.47)	33.36 (0.26)	7.28 (0.13)	130.60 (2.91)	6.76 (0.90)	102.98 (4.75)	10.91 (0.89)	65.59 (3.70)
3.08[b]	9.14 (0.13)	94.72 (8.22)	275.24 (4.54)	36.47 (0.32)	7.73 (0.01)	103.07 (5.28)	9.20 (0.93)	86.80 (6.17)	9.41 (0.81)	65.41 (1.23)
5.92	8.02 (0.17)	54.00 (1.81)	301.88 (4.43)	35.13 (0.90)	7.44 (0.20)	66.90 (1.46)	9.57 (0.62)	70.95 (0.75)	10.89 (0.60)	56.91 (0.85)
14.75	7.78 (0.61)	43.01 (1.87)	297.35 (13.85)	37.38 (1.70)	7.59 (0.24)	53.04 (1.42)	7.55 (0.72)	63.40 (2.72)	8.47 (0.81)	57.55 (2.73)
29.88	8.05 (0.14)	39.94 (1.16)	309.30 (15.01)	38.75 (0.72)	7.46 (0.20)	47.82 (1.52)	6.53 (0.90)	59.41 (0.40)	7.44 (0.49)	56.49 (0.58)
pH 5.0										
0.00	16.04 (0.10)	840.43 (0.18)	337.66 (3.4)	-0.12 (0.02)	NA	NA	NA	NA	NA	NA
14.75	15.88 (0.04)	404.53 (0.91)[g]	259.93 (1.58)	13.84 (0.08)	NA	NA	10.75 (0.48)	134.82 (6.98)	12.92 (0.67)	60.07 (0.16)
29.88	16.13 (0.10)	338.99 (0.58)	297.27 (5.55)	20.01 (0.55)	NA	NA	7.61 (0.06)	146.63 (0.17)	10.04 (0.38)	82.04 (2.28)

[a]- Values within parentheses indicate 1-standard deviation of replicate samples, and do not reflect instrumental precision of the MC- ICP-MS analytical method, which was determined to be ± 0.02‰.

Table 4.2 Continued

[b]- Reactors for t = 3.08 d were inadvertently spiked with a slightly higher initial Fe(II) concentration, which is reflected in slightly higher aqueous Fe(II) masses.

[c]- Variable Fe(III) contents in the residual solids fraction are indicative of solids losses throughout the experimental procedure during centrifugation, decanting, and filtrations.

[d]- Average percentages of Fe(II) in extract 1 were 95% of total Fe content.

[e]- Average percentages of Fe(II) in extract 2 were 3.7% of total Fe content.

[f]- Average percentages of Fe(II) in extract 3 were 0.8% of total Fe content.

[g]- A different enriched ^{57}Fe(II) stock was used in this time point, with a $\delta^{57/56}$Fe value of 767.90‰. Aqueous $\delta^{57/56}$Fe values have been scaled to reflect a consistent initial $\delta^{57/56}$Fe value, using the measured data multiplied by a scaling factor of (840.43/767.90).

Table 4.3 Chemical and isotopic data during enriched Fe(II) isotope tracer experiment with goethite microrods.

	Aqueous Fe(II)		*Residual Fe(III)*		*Extract 1*		*Extract 2*		*Extract 3*	
Time (d)	Fe content (µmol)	$\delta^{57/56}$Fe (‰)	Fe content[c] (µmol)	$\delta^{57/56}$Fe (‰)	Fe content[d] (µmol)	$\delta^{57/56}$Fe (‰)	Fe content[e] (µmol)	$\delta^{57/56}$Fe (‰)	Fe content[f] (µmol)	$\delta^{57/56}$Fe (‰)
pH 7.5										
0.00	15.85 (0.46)	840.43 (0.18)	337.66 (3.4)	0.08 (0.03)						
0.007	11.19 (0.06)	814.88 (1.15)	323.23 (24.34)	7.56 (0.14)	4.63 (0.05)	368.18 (16.64)	1.80 (0.01)	76.65 (3.89)	1.38 (0.31)	31.52 (0.76)
0.50	10.52 (0.15)	216.59 (21.94)	306.73 (7.96)	29.29 (0.73)	4.68 (0.07)	180.97 (11.21)	1.71 (0.14)	84.20 (4.22)	1.41 (0.10)	43.16 (2.01)
1.58	11.25 (0.10)	98.30 (12.90)	297.54 (6.92)	36.29 (0.50)	4.33 (0.01)	98.97 (11.79)	1.72 (0.16)	67.21 (3.67)	1.16 (0.07)	38.33 (2.60)
3.08[b]	12.33 (0.58)	64.83 (9.39)	293.25 (3.79)	40.40 (0.97)	4.03 (0.16)	69.24 (8.54)	2.22 (0.43)	54.98 (7.75)	1.31 (0.19)	34.67 (1.18)
5.92	11.08 (0.12)	41.18 (1.24)	332.07 (16.93)	37.73 (0.56)	3.45 (0.02)	46.01 (1.88)	2.74 (0.92)	39.92 (1.52)	1.56 (0.39)	32.55 (1.62)
14.75	11.11 (0.18)	44.70 (2.51)	299.33 (4.62)	38.54 (0.59)	3.39 (0.12)	48.38 (4.75)	2.02 (0.17)	43.11 (4.20)	1.79 (0.24)	30.47 (0.57)
29.88	11.19 (0.08)	41.83 (1.46)	315.83 (19.86)	38.85 (0.65)	3.24 (0.10)	44.57 (2.63)	2.22 (0.25)	37.49 (2.55)	1.70 (0.45)	30.26 (0.25)
pH 5.0										
0.00	16.04 (0.10)	840.43 (0.18)	337.66 (3.4)	0.08 (0.03)	NA	NA	NA	NA	NA	NA
14.75	15.93 (0.03)	663.10 (1.52)[g]	289.02 (14.24)	6.80 (0.02)	NA	NA	2.20 (0.24)	160.59 (4.00)	1.64 (0.08)	65.45 (13.14)
29.88	16.29 (0.10)	597.15 (7.68)	313.74 (2.22)	10.76 (0.43)	NA	NA	1.65 (0.66)	216.29 (65.78)	1.35 (0.46)	115.63 (31.74)

[a]- Values within parentheses indicate 1 standard deviation of replicate samples, and do not reflect instrumental precision of the MC-ICP-MS analytical method, which was determined to be ± 0.02‰.

[b]- Reactors for t = 3.08 d were inadvertently spiked with a slightly higher initial Fe(II) concentration, which is reflected in slightly higher aqueous Fe(II) masses.

Table 4.3 Continued

[c]- Variable Fe(III) contents in the residual solids fraction are indicative of solids losses throughout the experimental procedure during centrifugation, decanting, and filtrations.

[d]- Average percentages of Fe(II) in extract 1 were 98% of total Fe content.

[e]- Average percentages of Fe(II) in extract 2 were 18% of total Fe content.

[f]- Average percentages of Fe(II) in extract 3 were 5.5% of total Fe content.

[g]- A different enriched ^{57}Fe(II) stock was used in this time point, with a $\delta^{57/56}$Fe value of 767.90‰. Aqueous $\delta^{57/56}$Fe values have been scaled to reflect a consistent initial $\delta^{57/56}$Fe value, using the measured data multiplied by a scaling factor of (840.43/767.90).

Table 4.4 Percent Fe exchanged during Fe isotope tracer experiment (%).

	Nanorods		*Microrods*	
Time (d)	Aqueous Fe(II)	Goethite Fe(III)	Aqueous Fe(II)	Goethite Fe(III)
pH 7.5				
0.007	22.39[a] (7.35)[b]	34.04 (1.23)	3.18 (4.55)	19.97 (1.85)
0.50	82.64 (1.60)	75.28 (0.70)	77.70 (3.52)	77.90 (2.52)
1.58	89.44 (0.35)	88.82 (0.78)	92.44 (1.74)	96.58 (1.42)
3.08	92.88 (1.10)	97.07 (0.88)	96.60 (1.21)	107.55 (2.43)
5.92	97.95 (0.23)	93.53 (2.55)	99.55 (0.16)	100.42 (1.53)
14.75	99.32 (0.24)	99.49 (4.54)	99.11 (0.32)	102.58 (1.57)
29.88	99.71 (0.15)	103.13 (1.87)	99.47 (0.19)	103.39 (1.70)
pH 5.0				
14.75	54.29 (0.21)	37.05 (0.61)	22.09 (0.86)	17.93 (0.62)
29.88	62.46 (0.12)	53.40 (2.73)	30.30 (3.16)	28.50 (4.01)

[a]- Percent exchanged values were calculated with equation 3 in the text.

[b]- Values within parentheses indicate 1-standard deviation of replicate samples.

Table 4.5 Summary of ascorbic acid dissolution data at pH 3 and 5.5.

	pH 3.0				*pH 5.5*	
	Nanorods		Microrods		Nanorods	Microrods
Pre-treatment	Unreacted	+ Fe(II)	Unreacted	+ 1 Fe(II)	Unreacted	Unreacted
Dissolution Rate (μmol Fe(II)/hr)	0.262	0.255	0.096	0.095	0.043	0.015
SA-Normalized Flux[a] (mol Fe(II)/(m^2-sec) x 10^{11}	6.62	6.45	6.64	6.61	1.09	1.07
Log Flux[b] (mol Fe/(m^2-sec)	-10.18	-10.19	-10.18	10.18	-10.96	-10.97

[a]- Dissolution rates were normalized using specific surface areas collected for dry goethite powders – 110 m^2/g and 40 m^2/g for nanorods and microrods, respectively.

[b]- Flux rate units adopted from Brantley et al (2009) (see text).

Table 4.6 Goethite particle size comparison before and after reaction with aqueous Fe(II).

Sample	N =	Length (nm)	Width (nm)	Ref
Microrods	206	590 (275)[a]	42 (14)	Chapter 2[b]
Microrods + Fe(II)	78	555 (250)	45 (15)	This work
Nanorods	530	81 (28)	11 (4)	Chapter 2
Nanorods + Fe(II)	91	82 (32)	11 (5)	Chapter 3

[a]- Parentheses indicate 1-standard deviation.

[b]- A different average length is reported here because only TEM images were used in the histogram analysis, as opposed to the combination of TEM and SEM images used in Chapter 2. SEM images tended to contain only large particles, which skewed the distribution. Since particle size analysis of reacted microrods was performed using TEM, we felt it was more appropriate to compare goethite microrods before and after reaction with aqueous Fe(II) using identical characterization techniques.

CHAPTER 5: EVOLUTION OF MN OXIDE REDOX ACTIVITY AFTER REACTION WITH AQUEOUS FE(II)

Abstract:

Fe and Mn are both common redox-active metals in environmental systems, and Fe-Mn redox chemistry is an important consideration when predicting fate and transport of contaminants. Reactions of aqueous Fe(II) with pyrolusite (β-MnO_2) were assessed using electron microscopy, X-ray diffraction, aqueous Fe and Mn analyses, and ^{57}Fe Mössbauer spectroscopy. Pyrolusite solids were exposed to successive reactions with 3 mM Fe(II) at pH 7.5 in order to assess evolving reactivity of Mn/Fe solids. In addition, we have extended our selective use of Fe isotopes in conjunction with Mössbauer spectroscopy by using enriched ^{56}Fe(II) or ^{57}Fe(II), which were varied in their order of exposure to Mn solids, allowing us to probe marginal Fe(II) reactivity after preliminary Fe(II) oxidation or continuing redox reactions with initial Fe(III) precipitates. Using these complementary techniques, we determined that lepidocrocite was initially the predominant Fe oxidation product of Fe(II), and additional Fe(II) exposures resulting in an increasing proportion of magnetite on the pyrolusite surface. Over a series of nine 3 mM Fe(II) additions, Fe(II) was still always oxidized by Mn/Fe particles, implying that Mn phases can still be important redox active phases after extensive surface coverage with Fe(III) oxides. Initial Fe(III) oxide precipitates were also further reduced by additional Fe(II), and additional Mn was released into solution as additional Fe(II) was oxidized, indicating that Fe and Mn chemistry is influenced by subsequent reactions of Mn/Fe oxides.

Introduction

Iron (Fe) and manganese (Mn) are the two most common redox-active elements in the Earth's crust (*1*). Reactions between Fe and Mn species, as well as with other common groundwater constituents have significant impacts on mineral formation and

dissolution (*10*), trace metal sequestration (*3*), and contaminant transformations (*90, 136*). The present study focuses on redox reactions of ferrous iron (Fe(II)) with oxidized Mn(IV) solids. Thermodynamic considerations would predict that in the presence of Fe(II), all manganese species would exist as reduced manganese Mn(II) as opposed to oxidized Mn (IV). Complex environmental systems, however, do not always adhere to the compositions implied by thermodynamic constraints. Microorganisms have been shown to significantly impact the speciation of Fe and Mn between reduced and oxidized forms. (e.g., *137, 138*). Bacterial action can result in large local concentrations of dissolved Fe(II) or Mn(IV) solids that form and persist in transient but important time scales.

Certain geochemical conditions (low pH, anaerobic zones, presence of organic matter) can stabilize aqueous Fe(II), allowing reduced Fe to travel significant distances and interact with a variety of mineral species. Examples of scenarios where geochemical and kinetic effects dictate the redox interactions observed in field settings are widespread. Studies of both freshwater and marine porewater constituents have observed dissolved Fe(II) in the presence of Mn oxides (*139*) and implicated Mn oxides as the relevant oxidants of Fe(II) in porewaters (*140*). Interactions between Fe(II) and Mn oxides has been studied previously under several model geochemical settings, including acid mine drainage (*19, 141, 142*) and marine systems (*140*). Reaction of Fe(II) with Mn(IV) oxides has previously been described by the reaction:

$$2Fe^{2+} + MnO_2 + 2H_2O \rightarrow 2FeOOH + Mn^{2+} + 2H^+ \qquad (1)$$

in order to explain locally high concentrations of manganese oxides in sediments (*15*). Redox reactions of Fe(II) with Mn(IV) oxides would also result in an oxidized Fe species, which often occurs as a surface coating on the underlying Mn oxide substrate. Composition of resulting Fe oxides has previously been difficult to ascertain with traditional methods of solid-phase analysis such as x-ray diffraction (XRD) or electron

microscopy. Postma (1985) was unable to clearly define the Fe oxide coating that occurred on birnessite (δ-MnO_2) particles reacted with Fe(II), and in later studies chose to model the resulting Fe(III) oxide phase as an amorphous $Fe(OH)_3$ species (*143*). Krishnamurti and co-workers used a combination of infrared spectroscopy, XRD, and transmission electron microscopy (TEM) to determine that Fe(II) in contact with different Mn oxide substrates (e.g., cryptomelane, hausmannite, and pyrolusite) will react to form different Fe oxide layers, depending on experimental solution conditions (*144*).

Formation of an Fe(III) surface coating on Mn oxide solids may impact the rate or overall ability of Mn oxides to remain redox-active phases in environmental systems. In simulated acid-mine drainage systems, Mn(II) production from Mn oxides reacted with Fe(II) decreases with time, suggesting that evolution of a new Fe oxide surface interferes with the ability of underlying Mn oxides to accept electrons from aqueous Fe(II) (*142*). Further studies in this experimental system attributed changing rates of Fe(II) loss and Mn(II) production from batch reactors to Langmuir-type blocking of Mn(IV) surface sites by Fe(III) oxide precipitates using a model simulations (*19*). In these studies, it was also difficult to concretely ascertain the composition of resulting Fe(III) reaction products. Fe(II)/Mn(IV) redox activity may also negatively impact future oxidation capacity of Mn oxides, which have been demonstrated to be important oxidants for a variety of important environmental remediation processes (*21, 145*). Formation of an amorphous Fe(III) precipitate was shown to inhibit Cr(III) oxidation by birnessite at pH 5.5 (*18*).

In this study we wished to evaluate the effect of aqueous Fe(II) on electron transfer reactions at Mn oxide surfaces. Mn oxide particles were reacted with successive exposures of Fe(II) at pH 7.5. Most investigations involving Fe(II) and Mn oxides have occurred at lower solution pH values between 3-6 in order to simulate acid mine drainage. Evaluation of Fe/Mn redox chemistry at circum-neutral pH values is also important, as anoxic Fe(II) plumes may persist in neutral pH environments in the presence of Mn oxides (*146*).

Alongside traditional methods of analysis (XRD, microscopy, chemical Fe and Mn analyses), we utilized ^{57}Fe Mössbauer spectroscopy in conjunction with isotopically enriched ^{57}Fe(II) in order to increase the Fe signal (natural Fe contains roughly 2% ^{57}Fe). To further examine Fe(III) surface precipitate morphology and what effect this phase has on further redox reactions with Fe(II), we exposed Mn oxide particles to a series of solutions buffered at pH 7.5 which contained either ^{57}Fe(II) (Mössbauer-active) or ^{56}Fe(II) (Mössbauer-inactive). In this manner, we could submit Mn oxide solids to a series of Fe(II) exposures, but only a particular "pulse" of Fe(II) would be visible with Mössbauer spectroscopy throughout the experiment. This procedure allowed us to track the chemical changes that occurred to a specific set of Fe atoms, even as more Fe(II) is introduced to the particle surface. Evolving redox capacity of Mn oxides was assessed through measurements of aqueous Mn and X-ray photoelectron spectroscopy.

Materials and Methods

Mn Oxide Solids Characterization

Commercially available MnO_2 (Sigma-Aldrich) was used for the entirety of the present study. Mn oxides were ground with a mortar and pestle before sieving (150-micron mesh) to achieve a uniform particle size. XRD was performed on solids using a Rigaku Miniflex II equipped with a Co X-ray source. Initial characterization with XRD indicated pyrolusite (β-MnO_2) was the sole Mn oxide phase, and no diffraction peaks indicative of impurities could be detected (Figure 5.2). Surface area measurements on sieved Mn oxide powders were made with a Quantachrome BET Nova surface area analyzer using a multipoint measurement and consistently resulted in low specific surface areas, ~ 1-2 m^2/g.

Sequential Batch Experiments with Isotopically-Enriched Aqueous Fe(II)

All reagents were used as received. Experiments were performed in an anaerobic chamber with multiple palladium catalysts to scavenge trace O_2, and all solutions were made with deionized water that had been deoxygenated through N_2 sparging. Aqueous Fe(II) stock solutions were prepared by dissolving enriched ^{56}Fe or ^{57}Fe metal (Chemgas, 99% and 96%, respectively) in 0.5 M HCl. To initiate Fe(II) redox experiments, 18 mL of a pH 7.5 buffer solution (25 mM 4-(2-hydroxyethyl)-1-piperazineethanesulfonic acid (HEPES) + 25 mM KBr) was spiked with either a ^{57}Fe or ^{56}Fe stock solution to yield an initial aqueous Fe concentration of roughly 3 mM. Prior to Fe addition, reactors were counter-spiked with 0.5 M NaOH to maintain initial pH. Reactors were equilibrated for 1 hr before filtering through a 0.2-micron syringe filter to remove any potential Fe precipitates. Initial Fe(II) concentration was measured, and 18 mg of Mn oxide powder was added to initiate the timecourse (solids loading 1 g/L, Fe/Mn molar ratio 0.26). Reactors were placed on an end-over-end rotator and mixed in the dark. Periodically, small aliquots (~150 uL) of solution were withdrawn, filtered with 0.2-micron nylon syringe filters, and used for chemical Fe and Mn analyses. Fe(II) redox experiments were typically allowed to run for ~ 90 min. If solids for a particular experiment were scheduled to receive more than 1 treatment in an aqueous solution, experimental reactors were allowed to stand for a short amount of time to allow dense Mn solids to settle, where they could be easily removed with a pipette. Solids were placed in a microcentrifuge tube and centrifuged to pellet solids and facilitate easy removal of the residual aqueous supernatant. Mn solids were then resuspended in a new buffer solution containing 3 mM $^{57}Fe(II)$, $^{56}Fe(II)$, or no Fe, depending on the particular experiment, and a new timecourse was performed to investigate the movement of aqueous Fe and Mn into or out of solution. Solids resuspension in new buffer solutions with or without additional aqueous Fe(II) was repeated anywhere from 1-9 times.

Acid Extractions

In an attempt to reconcile the amount of Fe(II) lost from solution with the production of Mn(II) into solution, acid extractions were performed on recovered solids to remove surface precipitates of Fe and any adsorbed Fe or Mn species. Control reactors with an identical buffer system, Mn solids loading, and Fe/Mn ratio were mixed for 90 min before solids were collected and resuspended in deionized water. Varying amounts of 5 M HCl were added to different reactors to obtain a distribution of pH values between ~ 1- 2. Extraction reactors were allowed to mix for ~ 150-300 hours, periodically removing samples for Fe and Mn analyses.

Chemical Analyses

Aqueous Fe(II) was measured colorimetrically using 1,10-phenanthroline at 510 nm (*128*). Fluoride was used to remove interferences from aqueous Fe(III) when present in samples (*106*). The amount of Fe(III) in solution was determined by the difference of measured Fe(II) content and the Fe concentration of a sample that had been completely reduced from the addition of hydroxylamine HCl. Aqueous Mn was determined by modifying the formaldoxime method outlined in Morgan and Stumm (*17*) and Abel (*147*), using phenanthroline to complex interfering aqueous Fe.

Post-Reaction Solids Characterization

After the final timecourse in the presence or absence of aqueous Fe(II), solids were captured by filtration through a syringe filter with a removable 0.45-micron filter disc. A small portion of recovered solids (~ 1 mg) were removed from the filter disc and rinsed with deionized water to remove residual aqueous Fe, Mn, and buffer salts. Rinsed solids were placed on an aluminum microscopy stub and fixed with carbon tape. Imaging of resulting particles and surface precipitates was performed with a Hitachi S-4800 scanning electron microscope. Remaining Mn/Fe solids recovered after sequential reaction experiments were wrapped in Kapton oxygen-impermeable tape prior to analysis

with ^{57}Fe Mössbauer spectroscopy. Mössbauer spectra were collected in transmission mode using a ^{57}Co source and a Janis cryostat with temperature control to 13 K. Mössbauer spectra collected at room temp, 140 K, 77 K, and 13 K, and data was calibrated against α-Fe foil spectra collected at room temperature, Spectral fitting was performed with the Recoil Software package (http://www.isapps.ca/recoil/)

Oxidation states of Mn and Fe atoms near the surface of reacted Mn/Fe particles were characterized with x-ray photoelectron spectroscopy (XPS) using a Kratos Axis Ultra XPS system. Activated carbon was used as an internal reference standard in all samples. Mn oxidation states were assessed by comparing the difference in binding energies of the Mn $2p^{3/2}$ and O 1s peaks, a method successfully utilized to characterize oxidation of different transition metals (*148, 149*). Mn $2p^{3/2}$ – O *1s* differences were determined for unreacted MnO_2 starting material and compared to samples that had been reacted with 1 and 2 suspensions of aqueous Fe(II) in the manner described above.

Results and Discussion

Formation of Fe(III) Precipitate

Oxidation of aqueous Fe(II) by pyrolusite stimulated a rapid and pronounced change in observed particle morphology. After exposure to aqueous Fe(II), the normally featureless pyrolusite surface was completely transformed into a dense network of needlelike protrusions and fused platelets, likely due to formation of an Fe(III)-containing precipitate (Figure 5.1). Individual needles ranged in length from ~ 200 – 800 nm. Many Fe(III) oxides exist as rod-like structures, including goethite, lepidocrocite, and akaganeite, and schwertmannite (*24*).

Powder X-ray diffraction (XRD) patterns collected after pyrolusite solids were reacted with 3 mM Fe(II) at pH 7.5 reveal the presence of lepidocrocite (γ-FeOOH) in the solid phase, which is consistent with needle-like precipitate morphology observed in SEM images (Figure 5.1). No other Fe phases could be detected, indicating that

lepidocrocite is the dominant phase formed during Fe(II) oxidation by pyrolusite at pH 7.5. Synthetic lepidocrocite is commonly formed through rapid Fe(II) oxidation in air at near-neutral pH values (*24*), conditions which are analogous to our experimental work through heterogeneous redox reactions with Mn oxides, promoting rapid anaerobic oxidation of Fe(II) with pyrolusite.

Mössbauer spectra of the precipitate formed after the initial reaction of pyrolusite with aqueous ^{57}Fe(II) reveal several interesting characteristics. At room temperature (298 K), the Fe precipitate has doublet spectral parameters indicative of a ferric solid (center shift = 0.37 mm/s, quadrupole splitting = 0.53 mm/s). Absence of ferrous doublet character (with a larger center shifts and quadrupole splitting) in Mössbauer spectra indicates that all solid-associated Fe was oxidized to Fe(III) (Figure 5.3). Room-temperature Mössbauer parameters can not conclusively indicate the presence of lepidocrocite, as similar ferric doublets occur for multiple Fe oxides. At lower collection temperatures, spectral doublet features are replaced by a sextet as magnetic ordering occurs in the sample. Between 77 K and 13 K, the Fe phase is ordered into a sextet, characteristic of lepidocrocite or ferrihydrite (*68*). Mössbauer spectra collected at 13 K indicate that the initially observed doublet has not resolved into a fully ordered sextet, an uncommon observation for a majority of Fe(III) oxides. Lepidocrocite has an average ordering temperature of ~ 70 K (*68*). Potential explanations for decreased ordering temperature in Fe oxides include decreasing crystallite size and cation substitution into the solid structure. Although Mn incorporation has not previously been observed in lepidocrocite, estimates of ionic radii for Mn(II) or Mn(III) cations are similar to those expected for Fe(III) in oxides.

Formation of an Fe precipitate was supported by rapid loss of Fe(II) from the aqueous phase upon introduction to pyrolusite (Figure 5.4). According to equation 1, loss of Fe(II) should be accompanied by formation of aqueous Mn(II), although reaction stoichiometry in equation 1 predicts production of half as much Mn(II) produced as

Fe(II) consumed. Although our colorimetric method does not permit speciation of Mn, it is reasonable to assume that aqueous Mn is most likely Mn(II) based on solubility constraints (*17*). Aqueous Mn is produced as Fe(II) is consumed, but yields of Mn do not reach levels predicted by equation 1. Average recoveries, calculated as:

$$\text{Recovery (\%)} = \frac{100 \times 2 \times [\text{Mn produced}]}{[\text{Fe(II) Lost}]} \qquad (2)$$

are typically 40% in our experimental procedure for 3 mM Fe(II) reacted with 1 g/L pyrolusite. Non-stoichiometric production of aqueous Mn has previously been attributed to adsorption or entrainment of newly-produced Mn(II) in mineral surfaces (e.g., *15, 150*).

Acid extraction of Mn/Fe particles after reaction with aqueous Fe(II) was successful at recovering additional Mn as Fe(III) solids were dissolved. Compilation of Fe(III) recoveries and aqueous Mn recoveries for acid extractions in pH 1- 2 solutions at times ranging from 12-300 hours indicate relatively congruent dissolution of Mn and Fe(III), suggesting that Mn was evenly distributed throughout the Fe precipitate phase (Figure 5.5 and Table 5.1). Even distribution of Mn within Fe precipitates could be evidence for cation substitution of Mn into lepidocrocite, explaining the anomalously low ordering temperature observed in ^{57}Fe Mössbauer spectra. Contrary to expectations, we observed Mn recovery that more closely resembled a 1:1 ratio (solid line, Figure 5.5) with dissolved Fe(III) than a 1:2 ratio predicted by equation 1 (dashed line, Figure 5.5.) Although we cannot be certain due to our inability to speciate aqueous Mn, identical Mn and Fe recoveries may suggest a 1:1 reaction stoichiometry, meaning that Mn(III) was formed instead of Mn(II). Additional studies are currently being performed using extended X-ray absorption fine structure (EXAFS) spectroscopy to quantify Mn oxidation states of aqueous Mn initially produced from reactions with Fe(II) and Mn extracted from the solid phase. Control studies suspending unreacted pyrolusite particles

in pH 1.0 buffered solutions, our most extreme extraction condition, produced minimal Mn release after several days, suggesting Mn(IV) is not simply leaching into solution.

Sustained Redox Activity with Aqueous Fe(II)

Sustained exposure of pyrolusite particles to aqueous Fe(II) appears to induce noticeable shifts in observed Fe reaction products. After one reaction sequence with aqueous Fe(II), exposed surfaces of all visible Mn oxides are covered in needlelike precipitates, identified as lepidocrocite in XRD patterns (L - labeling, Figure 5.6-B-C). As these Mn/Fe oxide particles are resuspended in new Fe(II)-containing buffer solutions, clusters of small round precipitates begin to emerge and eventually dominate observed surface morphology (Figure 5.6-C, D).

^{57}Fe Mössbauer spectroscopy on Mn/Fe solids after successive resuspensions in aqueous Fe(II) indicate the formation of magnetite and/or maghemite (hereafter referred to as magnetite for simplicity). Magnetite commonly occurs as nanoscale spherical or cubic primary particles, consistent with observed particle morphology changes in SEM images (Figure 5.6). Room-temperature Mössbauer spectra clearly indicate increasing multi-sextet character indicative of magnetite as cumulative Fe(II) loading increases (Figure 5.7). Moreover, enriched ^{56}Fe and ^{57}Fe isotope experiments demonstrate sustained redox activity of newly introduced Fe(II) with Mn/Fe particles. Experiments were performed in which Mössbauer-active ^{57}Fe(II) was only exposed to Mn/Fe solids at the endpoint of reaction (all prior resuspensions in aqueous Fe(II) were performed using ^{56}Fe(II)). Mössbauer spectra collected after reaction of ^{57}Fe(II) in these cases provide a glimpse of marginal net reactivity of Fe(II) added to pyrolusite/lepidocrocite solids. In every case, ^{57}Fe(II) was observed to exist as an oxidized Fe solid consisting of lepidocrocite and/or magnetite, with no trace of adsorbed Fe(II) doublets (Figure 5.7). This was observed even after 9 resuspensions in 3 mM aqueous Fe(II) (8 x ^{56}Fe(II) + 1 x ^{57}Fe(II)), resulting in an addition of 27 mM of e^- to the system, exceeding theoretical

electron-accepting capacity of initial pyrolusite (1 g/L = 23 mM e^- for conversion of Mn(IV) to Mn(II)).

Attributing spectral area due to lepidocrocite (doublet) or magnetite (sextets) in Mössbauer data provides us with a means to quantify relative abundances of Fe phases present among the total population of ^{57}Fe atoms in the sample. Magnetite can display superparamagnetic behavior, which would cause magnetite to appear as a doublet in Mössbauer spectra and induce error in our estimations (e.g., *151*). This effect is minimized at low temperatures, and because the lepidocrocite doublet observed in our experimental protocol did not order until ~ 20 K, spectral fitting was performed at 77 K to minimize the errors caused by potential magnetite superparamagnetism. Analysis of spectra shown above in Figure 5.7 show a clear transition in marginal Fe(II) reaction products from lepidocrocite to predominantly magnetite after nine resuspensions in 3 mM aqueous Fe(II) (Figure 5.8). Lepidocrocite transformation to magnetite in the presence of aqueous Fe(II) is a commonly observed phenomenon (*89*), accomplished though solid-state transformations of lepidocrocite (*152*). A more quantitative assessment of the transition from lepidocrocite to magnetite precipitate formation is shown below in Table 5.2, as calculated by determining the proportion of spectral area at 77 K within the doublet and multi-sextet areas, respectively.

Impacts on Underlying Fe and Mn Solids

After pyrolusite solids had been exposed to ^{57}Fe in the reaction sequence, additional resuspensions in aqueous ^{56}Fe(II) allowed us to monitor changes occurring in previously-deposited Fe precipitates without interference due to formation of additional Fe precipitates.

Mössbauer spectra collected after additional rounds of Fe(II) addition show a general increase in magnetite character and a relative decrease in lepidocrocite doublet area, demonstrating that Fe atoms deposited in an initial precipitate are still able to

participate in redox reactions with aqueous Fe(II) (Figure 5.9, Table 5.2). A summary of spectral fitting for every sequential Fe isotope reaction series is shown in Table 5.2. Phase changes in Fe precipitates from oxidized lepidocrocite to mixed-valent magnetite provide evidence that Fe precipitates are able to participate in redox reactions with aqueous Fe(II), suggesting Mn/Fe particle complexes can still be important redox-active phases in reactions with constituents like Fe(II).

From aqueous Fe(II) data and Mössbauer data collected after sequential resuspensions in aqueous Fe(II), it is apparent that aqueous Fe(II) can still participate in redox transformations with pyrolusite particles, even after a surface precipitate of Fe has been formed. It is not clear, however, whether additional aqueous Fe(II) is reacting with the underlying Mn oxide, or solely with the Fe oxide precipitate. It is apparent that lepidocrocite to magnetite redox transformations are consuming some of the electron equivalents provided by additional aqueous Fe(II), as demonstrated by ^{57}Fe Mössbauer spectra (Figure 5.9). Resuspension of Mn/Fe particles in aqueous Fe(II) initiates a release of aqueous Mn in a similar non-stoichiometric fashion illustrated in Figure 5.4 (Figure 5.10), but no Mn is released into solution is the particles are simply resuspended in pH 7.5 buffer without aqueous Fe(II) (data not shown). Mn release from the solid phase upon Fe(II) addition could be an indication of further redox reaction between Mn(IV) and Fe(II). It could also simply be controlled by the physical changes that are taking place on the surface, as precipitated lepidocrocite is transformed to magnetite, allowing for release of adsorbed or incorporated Mn into solution. Regardless of the cause, aqueous Mn release in the presence of Fe(II) can be achieved despite the presence of an oxidized Fe surface precipitate, commonly thought to prevent further Mn chemical activity. As Fe precipitates may be prevalent on the surface of Mn oxides, the impact of Mn/Fe particle complexes on Mn release to environmental systems should not be ignored.

We analyzed solids formed after successive resuspensions in aqueous Fe(II) with XPS to examine the changes that occur to the near-surface manganese atoms after zero,

one, or two reactions with aqueous Fe(II). It appears that after reaction with Fe(II), observed energy differences between Mn *2p* $^{3/2}$ and O *1s* peaks are reduced from 112.4 eV to 111.3 eV, indicative of a reduced oxidation state for near-surface Mn (Table 5.3) (*148*). This trend does not appear to continue, however, in pyrolusite particles that have been reacted twice with aqueous Fe(II). Mn *2p* $^{3/2}$ – O *1s* differences for pyrolusite reacted once or twice with aqueous Fe(II) are nearly equivalent, indicating that any near-surface Mn present after two reactions with Fe(II) has the same average oxidation state as the near-surface Mn after only one reaction with Fe(II). XPS evidence seems to suggest the average redox state of near-surface Mn is not altered once an initial surface layer of Fe is deposited, indicating further redox transformations of Mn/Fe particles could be due to interactions with Fe precipitates, such as lepidocrocite in this case.

Conclusions

We have pursued a novel method to investigate evolving Fe-Mn heterogeneous redox activity, utilizing selective introduction of Fe isotopes in combination with ^{57}Fe Mössbauer spectroscopy to complement observations from bulk assessments of aqueous and solid phase transformations. In this fashion, we have shown that Fe(II) in the presence of pyrolusite at pH 7.5 stimulates rapid precipitation of a lepidocrocite phase with interesting morphology and possible incorporation of Mn (II) or Mn(III). Further redox reactions of Mn/Fe particle complexes with aqueous Fe(II) are still possible, as Fe precipitates can be reduced by exposure to additional Fe(II). Continued redox reactions with aqueous Fe(II) can also release additional Mn into solution, either through continued Fe-Mn redox activity or detachment of entrained manganese as surface properties of Mn/Fe particles complexes evolve. Contrary to assumptions previous assumptions, Mn oxide particles cannot simply be dismissed as passivated, redox-inactive phases after reaction with aqueous Fe(II), as important chemical transformations may still take place at Mn/Fe particle surfaces with newly increased surface area and reactive capacity.

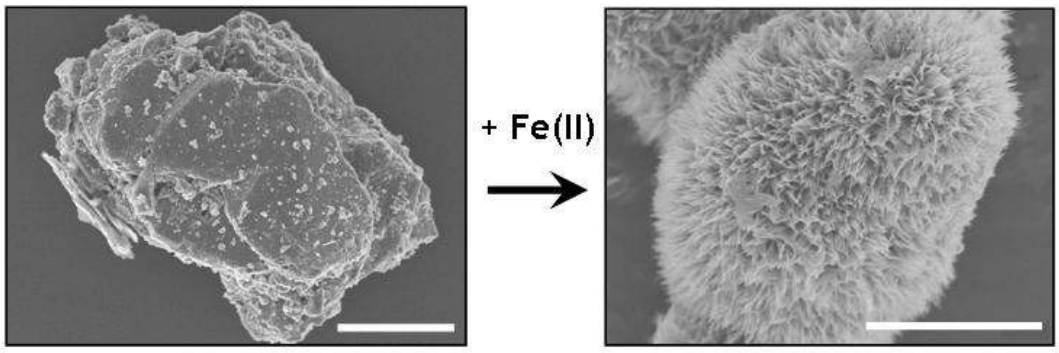

Figure 5.1 Scanning electron micrographs reveal the significant changes in particle morphology that occur when unreacted pyrolusite particles (left panel) are exposed to aqueous Fe(II). Extensive needlelike surface precipitates (right panel) cover the surface of every particle that was imaged, after one reaction sequence of pyrolusite with 3 mM aqueous Fe(II). Scale bars on both images are 5 microns.

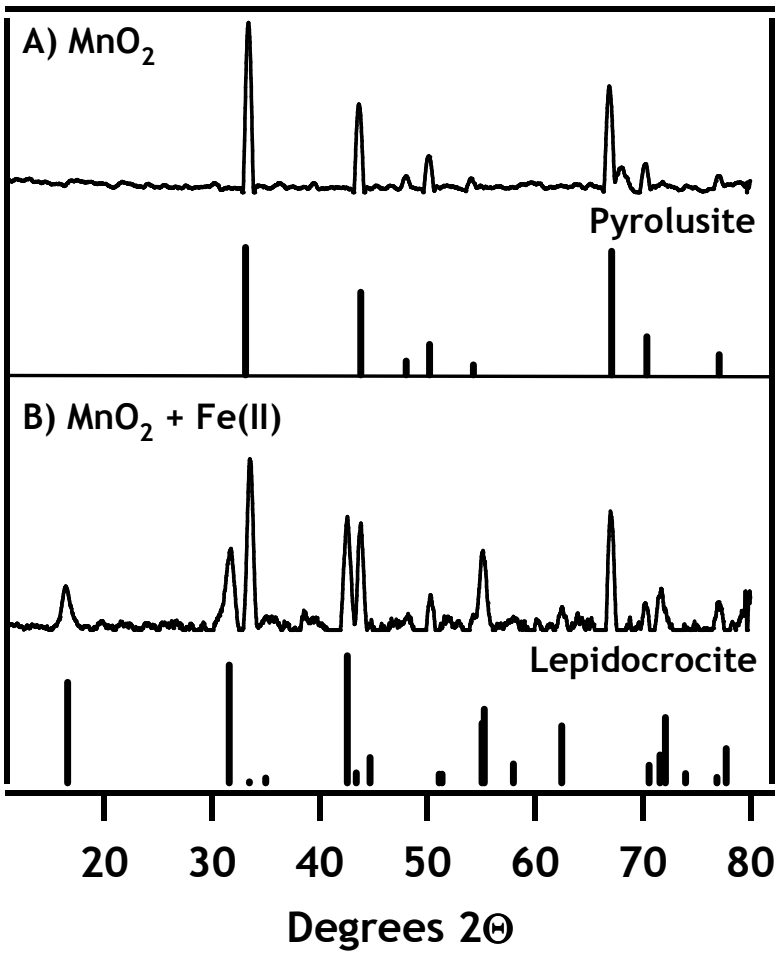

Figure 5.2 X-ray diffraction patterns of MnO_2 particles before and after reaction with aqueous Fe(II). Pyrolusite and lepidocrocite standard diffraction patterns are provided for reference.

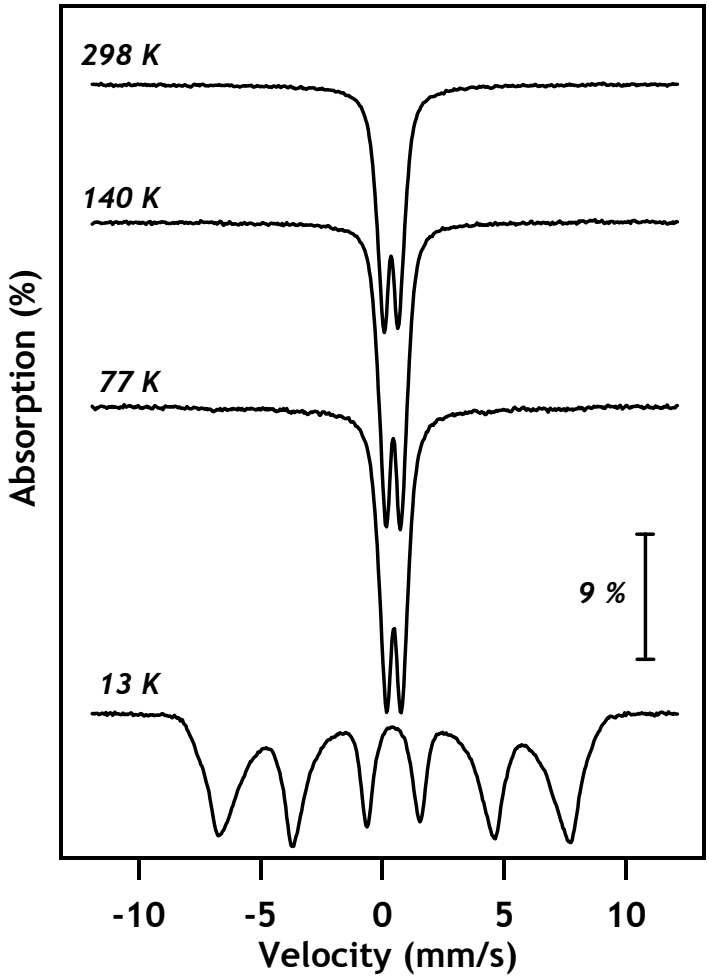

Figure 5.3 Mössbauer spectra of pyrolusite reacted with 3 mM ^{57}Fe(II). Spectra were collected at temperatures ranging from room temperature (298 K) to 13 K.

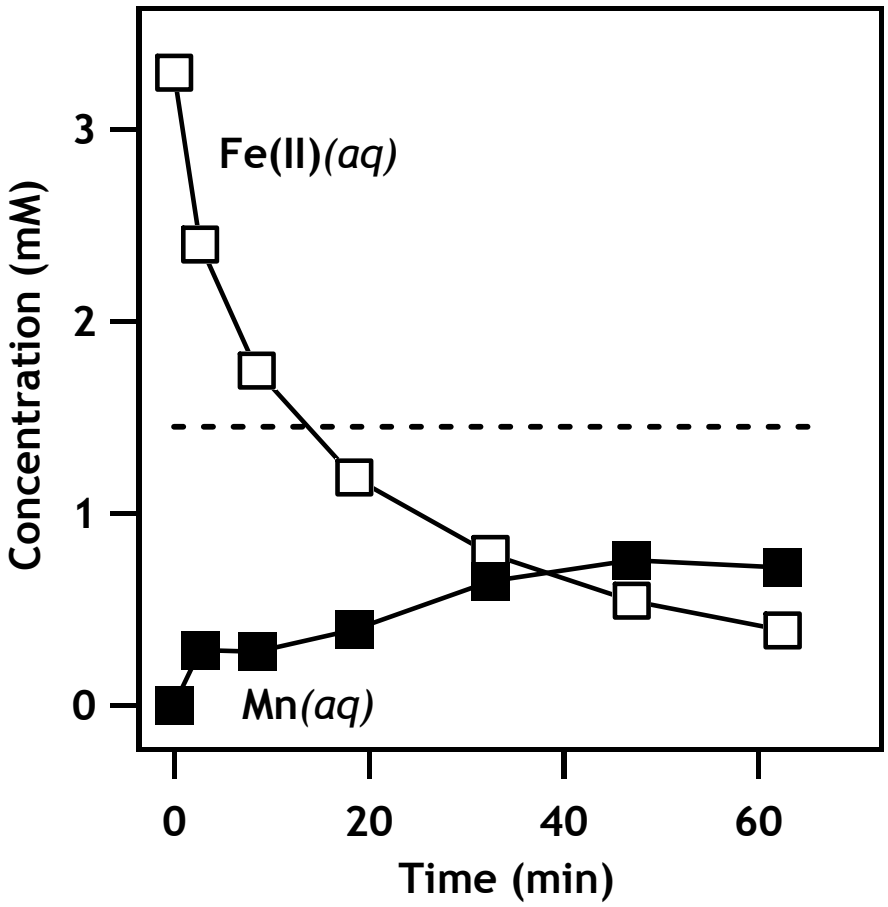

Figure 5.4 Example kinetics of Fe(II) loss from, and Mn appearance into, the aqueous phase after aqueous Fe(II) exposure to pyrolusite solids batch reactors. Dashed line represents theoretical predictions of Mn(II) based on stoichiometric redox reaction between Fe(II) and Mn(IV), shown in equation 2.

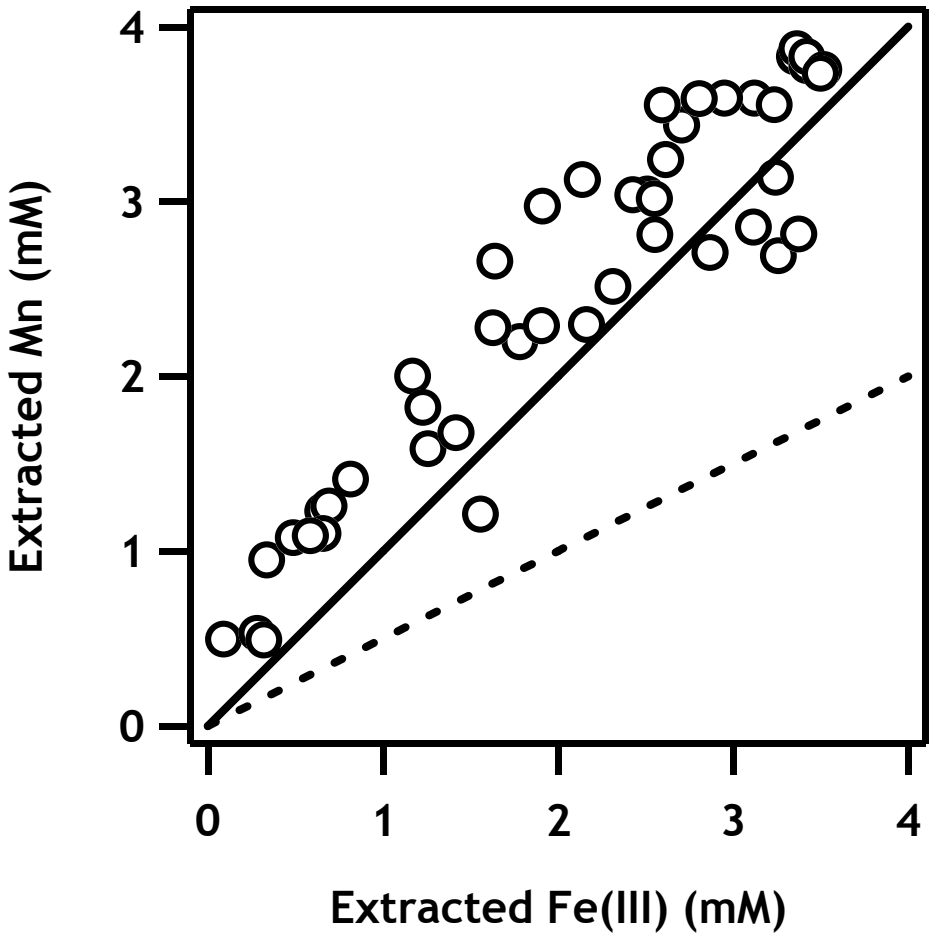

Figure 5.5 Summary of recovered Fe(III) and Mn after resuspension of Mn/Fe mixed-phase solids in low pH acid extraction reactors. Theoretical extraction results based on a 1 Fe : 1 Mn (—) or 2 Fe : 1 Mn (- - - -) reaction stoichiometry are provided for reference. Data cluster more closely around the 1:1 reaction line, indicating that Fe(II) may be reacting with Mn(IV) to produce Mn(III), which remains in the solid phase. A majority of data points cluster above the 1:1 line, due to the presence of ~ 0.6 mM Mn already existing in solution at the onset of acid extraction, as a result of the initial reaction between pyrolusite and Fe(II).

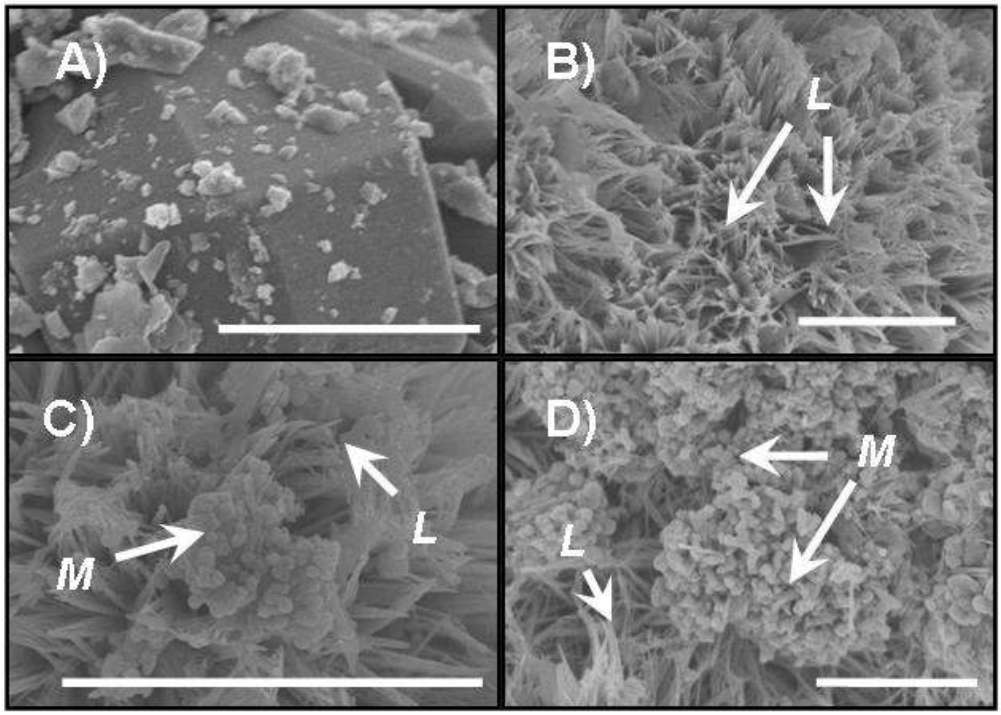

Figure 5.6 Scanning electron micrographs of unreacted pyrolusite particles (A), alongside pyrolusite particles resuspended one (B), twice (C), or three times (D) in 3 mM aqueous Fe(II). Scale bars in all images are 2 microns long. During successive exposures of the Mn/Fe particles to aqueous Fe(II), the appearance of smaller, round magnetite/maghemite clusters (M) begin to overtake the initial needlelike lepidocrocite (L) precipitates formed on the Mn surface. Fe phase identification as magnetite or maghemite is on the basis of observed morphology, ^{57}Fe Mössbauer spectroscopy, and x-ray diffraction results.

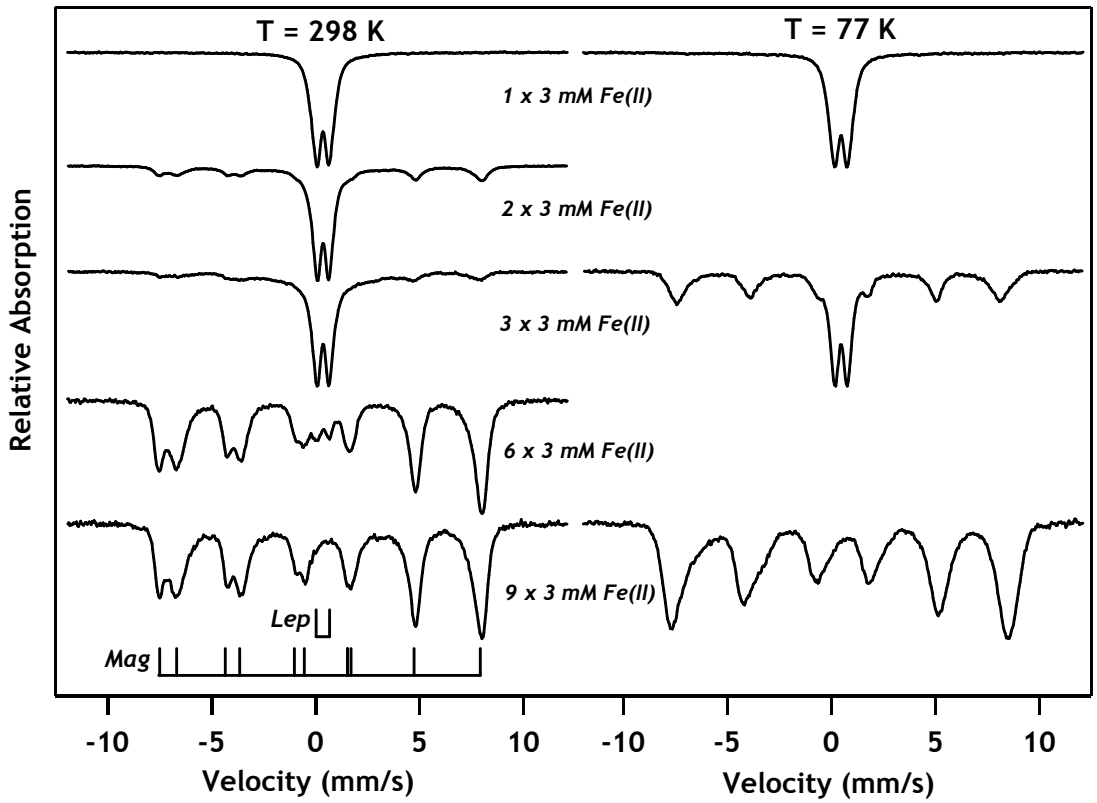

Figure 5.7 ^{57}Fe Mössbauer spectra of all experimental data collected in which only the final resuspension of Mn particles was done using ^{57}Fe(II). Room temperature (RT, 298 K) spectra are provided for all experiments (left column), with selected 77 K spectra of identical experiments (right column) for comparison. As the amount of Fe(II) exposure increases, we can see the final deposition of ^{57}Fe atoms onto the particle surface results in an increasingly large multi-sextet signal and a gradual disappearance of the doublet associated with lepidocrocite formation. Magnetite sextets appear to overlap more thoroughly at 77 K, which is commonly observed below the Verwey transition temperature (~ 120 K). Spectra collected at 77 K also contain a visibly higher ratio of sextet : doublet spectral area, possibly indicating the presence of unordered magnetite at room temperature, which orders into a typical sextet at lower collection temperatures.

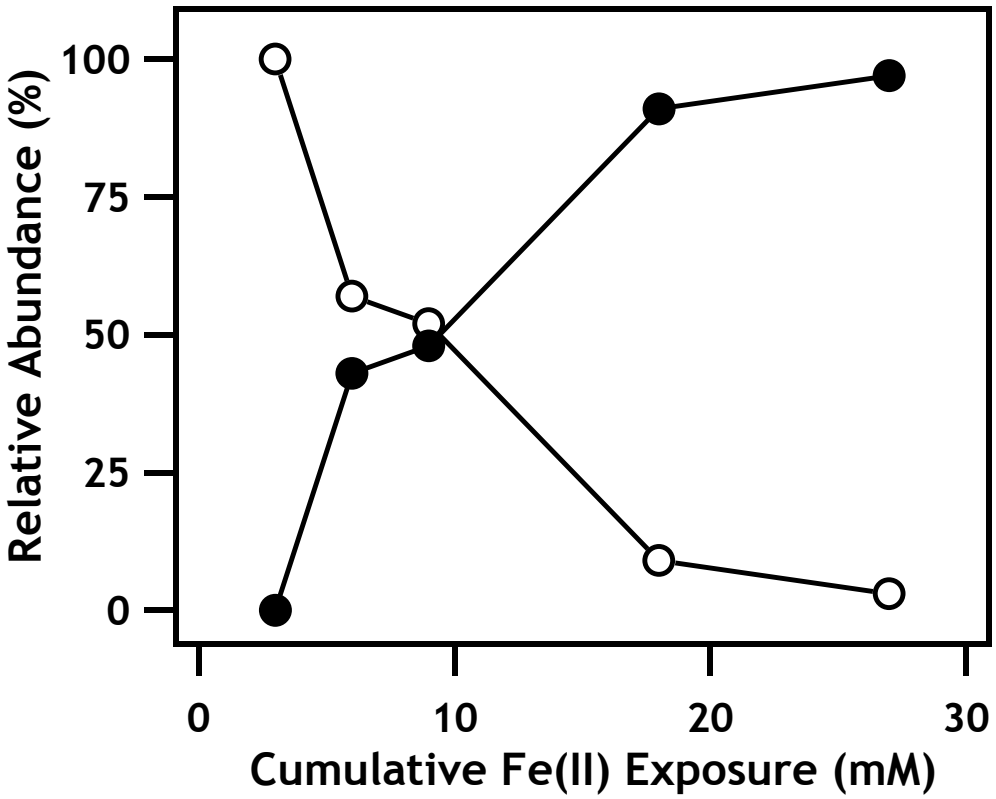

Figure 5.8 Relative abundances of lepidocrocite (open markers) and magnetite (closed markers) in marginal Fe(II) additions, as determined my Mössbauer spectral fitting of Fe phases at 77 K. Experiments were only exposed to ^{57}Fe during the final Fe(II) resuspension, permitting us to view chemical changes occurring to the marginal Fe(II) addition. Increasing Fe(II) exposure resulted in marginal Fe precipitate formation increasingly dominated by magnetite, as identified by characteristic overlapping sextets in Mössbauer spectra. .

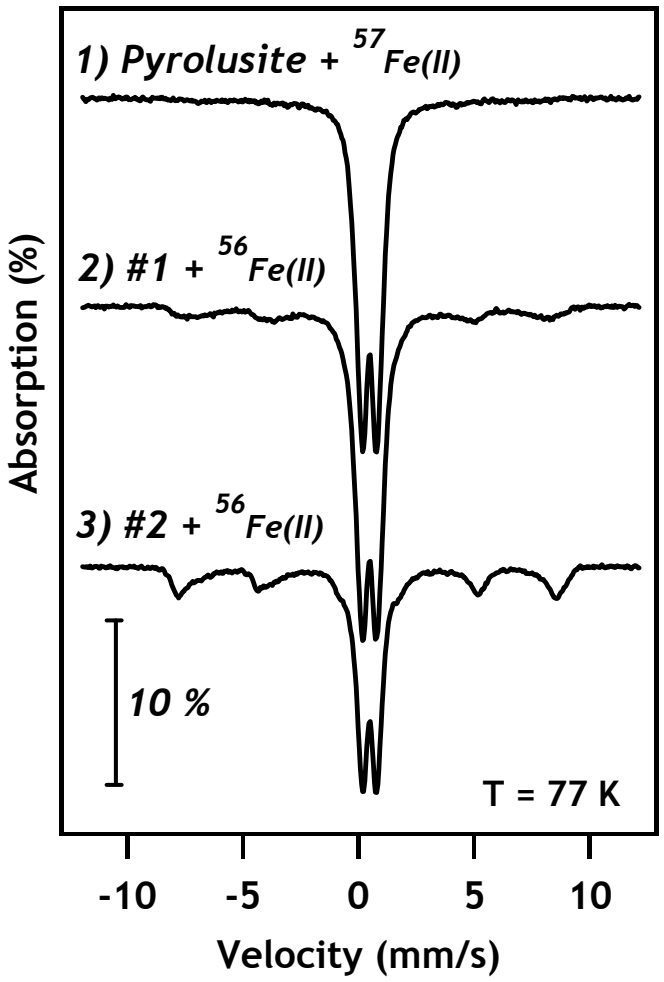

Figure 5.9 ^{57}Fe Mössbauer spectra of pyrolusite resuspended 1, 2, and 3 times in 3 mM aqueous Fe(II), where the Fe isotope order of addition was ^{57}Fe-^{56}Fe-^{56}Fe. A marked increase in magnetite character can be observed in successive spectra, which is indicative of chemical transformations occurring only in the initial ^{57}Fe atoms oxidized and precipitated on the pyrolusite surface.

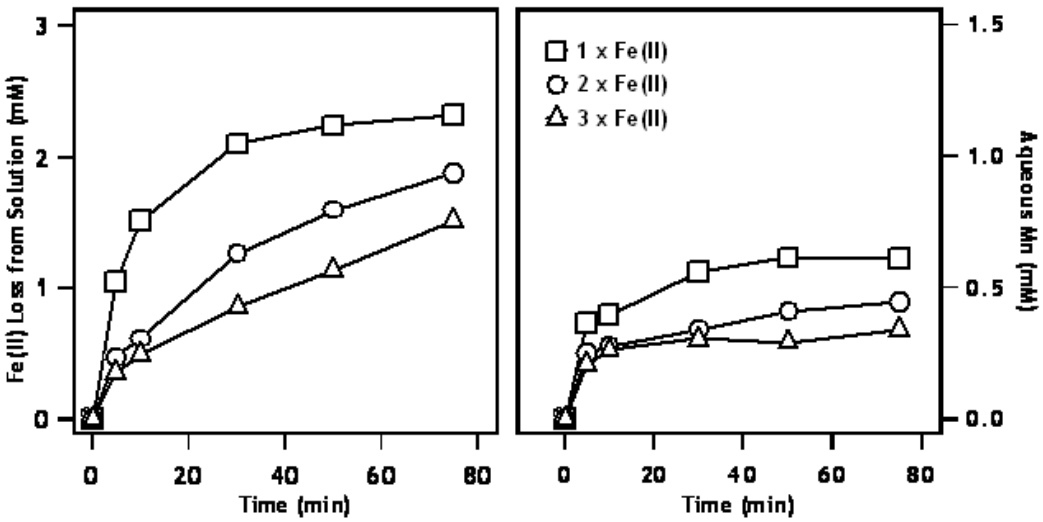

Figure 5.10 Kinetics of Fe(II) loss from (left panel, open markers) and Mn appearance into (right panel, filled markers) the aqueous phase. Squares (□) indicate data for the initial suspension of pyrolusite in Fe(II), circles (○) and triangles (Δ) indicate second and third resuspensions, respectively. Initial Fe(II) concentrations for this series of experiments were 2.4 mM. Note the difference in y-axis scaling between the two panels.

Table 5.1 Acid extraction data after reaction of 1 g/L pyrolusite with 3 mM Fe(II).

Sample No.	Acid Added[a] (mmol HCl)	Time (hr)	Fe(III) Extracted (mM)	Mn Extracted (mM)	$Fe(III)_{ext}$ / $Fe(II)_0$[b]	$Fe(III)_{ext}$ /: Mn_{ext}[c]
1	12.5	24.25	2.51	3.04	0.74	0.82
2	12.5	50.50	3.12	3.59	0.93	0.87
3	12.5	98.50	3.35	3.83	0.99	0.88
4	12.5	143.75	3.37	3.87	1.00	0.87
5	12.5	24.25	2.43	3.04	0.72	0.80
6	12.5	50.50	2.95	3.59	0.87	0.82
7	12.5	98.50	3.42	3.78	1.01	0.91
8	12.5	143.75	3.42	3.83	1.01	0.89
9	12.5	24.25	2.55	3.02	0.75	0.85
10	12.5	50.50	3.23	3.55	0.95	0.91
11	12.5	98.50	3.52	3.76	1.04	0.94
12	12.5	143.75	3.50	3.73	1.03	0.94
13	7.5	7.58	1.23	1.82	0.34	0.67
14	7.5	19.42	1.64	2.66	0.45	0.62
15	7.5	77.08	2.59	3.55	0.71	0.73
16	7.5	105.58	2.81	3.59	0.77	0.78
17	7.5	213.08	3.24	3.14	0.89	1.03
18	7.5	314.50	3.37	2.81	0.93	1.20
19	6.25	7.58	1.42	1.68	0.42	0.84
20	6.25	19.42	1.63	2.28	0.49	0.71
21	6.25	77.08	2.61	3.24	0.78	0.81
22	6.25	105.58	2.71	3.44	0.81	0.79
23	6.25	213.08	3.12	2.85	0.93	1.09
24	6.25	314.50	3.26	2.69	0.97	1.21
25	5	7.58	0.81	1.41	0.25	0.58
26	5	19.42	1.17	2.00	0.35	0.58
27	5	77.08	1.91	2.97	0.57	0.64
28	5	105.58	2.14	3.13	0.64	0.68

Table 5.1 Continued

29	5	213.08	2.55	2.81	0.77	0.91
30	5	314.50	2.87	2.71	0.86	1.06
31	3.75	7.58	1.56	1.21	0.46	1.28
32	3.75	19.42	1.26	1.59	0.37	0.79
33	3.75	77.08	1.78	2.20	0.53	0.81
34	3.75	105.58	1.90	2.29	0.57	0.83
35	3.75	213.08	2.16	2.30	0.64	0.94
36	3.75	314.50	2.31	2.51	0.69	0.92
37	2.5	7.58	0.34	0.95	0.10	0.35
38	2.5	19.42	0.49	1.08	0.15	0.45
39	2.5	77.08	0.66	1.23	0.20	0.53
40	2.5	105.58	0.69	1.26	0.21	0.55
41	2.5	213.08	0.66	1.10	0.20	0.60

[a]- Acid added as a spike of 5 M HCl.

[b]- Refers to the ratio of recovered Fe(III) as compared to Fe(II) concentration initially present in reactors before oxidation by pyrolusite.

[c]- Ratio of extracted Fe(III) to extracted Mn, at each time point.

Table 5.2 Relative abundances of lepidocrocite and magnetite/maghemite appearing in ^{57}Fe Mössbauer spectra at 77 K.

	Appearance of ^{57}Fe(II) in series[a]				
Fe(II) Addition	1st (Lep. / Mag.)	2nd (Lep. / Mag.)	3rd (Lep. / Mag.)	6th (Lep. / Mag.)	9th (Lep. / Mag.)
# 1	100 / 0	NA[b]	NA	NA	NA
# 2	85 / 15	57 / 43	NA	NA	NA
# 3	75 / 25	46 / 54	52 / 48	NA	NA
# 6	[c]----[c]	----	----	9 / 91	NA
# 9	----	----	----	----	3 / 97

[a]- Refers to the position of single ^{57}Fe(II) resuspension in the resuspension sequence. All other Fe(II) resuspensions were performed using ^{56}Fe(II), which would not contribute to observed Mössbauer spectra.

[b]- NA due to addition of ^{56}Fe(II) in this position. No Mössbauer spectral features were observed, as ^{56}Fe(II) is not visible to Mössbauer spectroscopy.

[c]-Dashed lines indicate that the experiment has not been performed.

Table 5.3 Summary of XPS data for manganese oxidation state characterization.

	Sample Description[a]		
	β-MnO_2	β-MnO_2 + Fe(II)	β-MnO_2 + Fe(II) + Fe(II)
Mn $2p^3/_2$ (eV)	641.5	638.9	640.2
O *1s* (eV)	529.1	527.6	528.8
Mn $2p^3/_2$ – O *1s* (eV)	112.4	111.3	111.4

[a]- Pyrolusite particles were reacted with aqueous Fe(II) using identical experimental conditions as other reported work (pH 7.5, 1 g/L pyrolusite, 3 mM Fe(II)).

CHAPTER 6: FE(II)-MAGNETITE ATOM EXCHANGE: EVIDENCE FROM ^{57}FE(II) TRACER STUDIES

Abstract

Fe(II) is known to reduce underlying Fe oxides through interfacial electron transfer, resulting in newly reduced Fe atoms within solid Fe oxides. Reduced Fe atoms may detach and resorb at new sites, resulting in dynamic and extensive Fe atom exchange with Fe(II) and Fe oxides, as has been recently demonstrated by our work with Fe(II) and goethite. Our goal for this project was to investigate Fe(II)-magnetite redox-driven atom exchange, as influenced by initial magnetite stoichiometry and cation substitution for Fe(II) in magnetite. Preliminary results indicate that Fe(II)-magnetite atom exchange does occur, although only a subset of Fe oxide Fe atoms appear to be participating after 30 d of reaction. Nonstoichiometric magnetite appears to exchange Fe atoms more rapidly than stoichiometric magnetite, although a lag period preceded steady atom exchange in nonstoichiometric magnetite. Co-substitution appears to reduce overall Fe atom exchange between Fe(II) and magnetite, perhaps limiting Fe exchange to the first few layers of Fe in the solid.

Introduction

Iron (Fe) is prevalent in a variety of geochemical settings, existing primarily in reduced ferrous (Fe(II) and ferric (Fe(III) states, in both aqueous and solid species. Interactions of aqueous Fe(II) with solid Fe oxides influence mineral transformations (*10, 89*), contaminant reduction (*90*), and Fe availability for participation in other biogeochemical cycles (*153*). Fe(II) can often stimulate secondary mineralization of unstable Fe oxides, controlling heavy metal fate and transport processes (*154*). Rather than interacting as passive sorbent on solid Fe phases, Fe(II) may participate in redox interactions with oxidized Fe solids, donating an electron into the bulk structure (*11, 12, 87*). Reduced structural Fe may detach from solids, resulting in Fe(II)-stimulated

reductive dissolution (*14*). Because the net result of this reaction would be one Fe(II) lost from solution plus one Fe(II) atom released into solution, traditional methods of aqueous and solid phase Fe analysis will have difficulty measuring the extent of this behavior.

Selective use of stable Fe isotopes allows us to resolve this quandary, due to recently-developed analytical techniques that can precisely measure Fe isotope ratios. We have recently taken advantage of this instrumentation to monitor Fe(II)-goethite redox reactions and atom exchange between the aqueous and solid phase. Using an Fe(II) tracer that was enriched in ^{57}Fe, we could track the introduction of ^{57}Fe(II) into the solid phase over time (*127, Chapters 3 and 4*). Results indicated that nearly all Fe(III) atoms initially present within goethite were able to equilibrate with enriched ^{57}Fe(II) atoms, resulting in isotope distributions in both the aqueous Fe(II) and solid phase Fe(III) that closely matched the isotope composition predicted from complete homogenization of Fe(II) spike and goethite Fe(III) atoms. Because net Fe(II) concentrations (after quick net Fe(II) uptake) or goethite particle morphology were unchanged during widespread atom exchange, we proposed a mechanism of spatially distinct Fe(II) oxidation and Fe(III) reduction sites on the goethite particle, linked by bulk conduction of electrons through the solid phase, as a means for inducing widespread Fe atom exchange. This mechanism has been clearly demonstrated in hematite crystals, and postulated by others to explain changing Fe(II) isotope signatures after reaction with goethite as well (*13, 96*).

In this study, our goal was to utilize a similar ^{57}Fe(II) isotope tracer approach to investigate the potential for redox-driven atom exchange in magnetite (Fe_3O_4). Magnetite contains Fe atoms in both +2 and +3 oxidation states, which may increase the rate at which electrons can move through the Fe oxide. Magnetite should contain a 1:2 ratio of Fe(II):Fe(III), but non-stoichiometric magnetite may also exist, with an Fe(II):Fe(III) ratio somewhere between 0.5 and 0. With no Fe(II) present, the oxide is completely transformed to maghemite (γ-Fe_2O_3), the fully oxidized counterpart of magnetite. This Fe(II):Fe(III) ratio, denoted as X in our work, has recently been shown to dictate the

extent of Fe(II) uptake in magnetite and overall reactivity with nitrobenzene (*155*). The influence of X on Fe atom exchange between Fe(II) and magnetite was examined by using two batches of magnetite solids with distinct X values. We also studied the effect of cation substitution on electron transfer, utilizing Cobalt (Co)-doped magnetite as an additional specimen. Replacement of redox-active Fe atoms with more insulating materials, such as Co, has been shown to influence electron-transfer capacity in magnetite (*156*).

Experimental Approach

Magnetite Synthesis and Characterization

Three different batches of magnetite solids were used in the following experiments. Fe magnetites were synthesized under anoxic conditions in a 93:7 N_2:H_2 anaerobic glovebox equipped with multiple Pd-catalysts for oxygen removal. Isotopically-normal Fe(II) and Fe(III) were combined at a 1:2 ratio in deionized water (added as $FeCl_2 \cdot 4H_2O$ and $FeCl_3 \cdot 6H_2O$, respectively) before raising solution pH to 10 with NaOH (*155, 157*). Magnetite precipitates were aged in anoxic suspension for 24 hr. To lower initial Fe(II) content of magnetite, one magnetite suspension was allowed to mix for an additional 24 hr in the presence of H_2O_2. Solids were collected by filtration and freeze-dried, with great care taken to prevent oxygen intrusion to anaerobic containers during the brief (~ 4 hr) removal from the glovebox atmosphere for freeze drying. A commercial sample of magnetite in which Fe(II) had been replaced with Co(II) was purchased (NanoAmor) and used as received.

Previous work with this magnetite synthesis method has reliably produced magnetite batches of relatively uniform particle morphology, with no observable secondary Fe phases in X-ray diffraction (XRD) patterns (*155*). Transmission electron microscopy (TEM) indicated that Co-substituted magnetite (Co-magnetite) was of a similar primary particle size (~ 25 nm diameter cubes) as synthetic magnetites. In all

three magnetites, surface Fe or Co atoms should account for ~ 5-10% of total Fe and Co atoms present within the structure, using simple geometric approximations based on observed morphology and particle size. Initial Fe(II)/Co(II):Fe(III) ratios and total Fe and Co content were assessed for all three samples by dissolving pre-weighed solid samples in 5 M HCl. Fe was measured colorimetrically using the phenanthroline method to measure Fe(II) (*128*). Hydroxylamine HCl was used to reduce all Fe to Fe(II) for total Fe determinations, and Fe(III) content was determined by difference between total Fe and Fe(II) measurements, in which ammonium fluoride was used to remove interferences from Fe(III) (*106*). In samples containing Fe(II), Fe(III), and Co, a rapid measurement of Fe(II) was required to prevent interference from Fe(III), which was reduced to Fe(II) in the presence of aqueous Co(II). Co concentrations were determined colorimetrically using l-Nitroso-2-naphthol-3,6-disulfonic acid disodium salt hydrate (NRS) as a complexing agent, adapting the method of Zahir and Keshtkar (*158*). Samples were buffered at pH 6.0, heated for 1 hr at 60 ºC, and acidified with HCl prior to analysis at 520 nm. NRS is not selective for Co(II), but Co(III) is not expected to be present in solution at pH 7.5 due to solubility constraints.

Fe(II):Fe(III) analyses of magnetite in which Fe(II):Fe(III) was added in the stoichiometric 1:2 ratio and not oxidized indicated an initial magnetite stoichiometry very close to the predicted value of X = 0.5 (X = 0.51 ± 0.01, S-magnetite). The magnetite batch exposed to H_2O_2 during aging had an initial Fe(II) content well below stoichiometry (X = 0.29 ± 0.01, NS-magnetite). Cobalt-substituted magnetite had an initial Co:Fe(III) ratio that was intermediate to the two Fe-magnetites (X_{Co} = 0.41 ± 0.003 assuming all Co was present at Co(II), Co-magnetite).

Fe Isotope Tracer Studies

Experiments involving enriched ^{57}Fe isotope tracer studies were performed in a similar fashion as our previous work (Chapters 3 and 4), with all work being performed

in an anaerobic glovebox. An aqueous Fe stock was created by combining different amount of dissolved ^{57}Fe and ^{56}Fe (Chemgas, 96% and 99%, respectively, 300 mM Fe(II) dissolved in 1 M HCl) to achieve a ~ 70% enrichment in ^{57}Fe, as compared to isotopically-normal Fe ($\delta^{57/56}Fe$ = 715.91‰). Small amounts of enriched ^{57}Fe(II) stock were added to 15 mL of 50 mM 3-(*N*-morpholino)-propanesulfonic acid (MOPS), buffered at pH 7.2, to create a ~ 1 mM Fe(II) solution. After 1 hr of equilibration, Fe(II)-MOPS solutions were filtered with 0.2-micron syringe-tip filters into a new glass vial. Initial Fe(II) content was measured, and experiments were initiated by adding 15 mg of magnetite solid (solids loading 1 g/L). Batch reactors were crimp-sealed and mixed on an end-over-end rotator in the dark. After time periods ranging from 10 min- 30 d, reactors were sacrificed in triplicate for chemical and isotope analysis. Control reactors were also initiated containing magnetite solids without aqueous Fe(II), and aqueous Fe(II) in the absence of magnetite solids. While not perfect, this approach minimizes pseudoreplication in our batch reactor protocol (*159*). Appropriate measures were taken to guard against demonic and non-demonic intrusions (*159*).

Sequential extractions were performed on individual reactors. Aqueous phase contents of batch reactors were separated by magnetically-separating solids and decanting the solution into a syringe filter equipped with a 0.2-micron filter. After filtering into a new vial, the solution was acidified to preserve Fe(II) and Co in solution. Magnetite solids were resuspended in 5 mL of a new buffer solution, with the goal of removing roughly as much Fe(II) as was lost due to net Fe(II) uptake during reaction. Fe(II) uptake capacity varied widely for each type of magnetite solid, so different extract protocols were employed for each type of solid (Table 1). After extraction, extract solutions were separated into new glass vials through similar magnetic separation / decanting / filtration steps. Magnetite solids remaining after extraction were completely dissolved in 5 M HCl. Complete dissolution occurred in a matter of minutes at room temperature for two Fe-only magnetites, while heating at 60 ºC for multiple hours was required for Co-magnetite.

In addition to colorimetric Fe(II), Fe(III), and Co analyses, each sample was analyzed for stable Fe isotope ratios using multi-collector inductively-coupled plasma mass spectrometry (MC-ICP-MS) (Micromass *Isoprobe*), following methods established previously (Chapters 3 and 4).

Results and Discussion

Results will be presented primarily as figures and tables, with preliminary discussion underneath appropriate figures. Tables 6.2, 6.3, and 6.4 contain raw data for S-magnetite, NS-magnetite and Co-magnetite, respectively. System-wide Fe isotope distributions were calculated by summing the mass-balance weighted isotope distributions of initial aqueous Fe(II) and magnetite Fe(III) added to the reactors, similar to Chapters 3 and 4 (equation 2). Percent Fe exchange was calculated using the formula in equation 3 (*130, Chapter 4*):

$$x\ \delta^{57/56}Fe_{sys} = \frac{[Fe_{aq,\ t=0}]x\ \delta^{57/56}Fe_{aq,\ t=0} + [Fe_{mag,\ t=0}]x\ \delta^{57/56}Fe_{mag,\ t=0}}{[Fe_{aq} + Fe_{mag}]} \quad (2)$$

$$\text{Percent Exchange (\%)} = \frac{100^{*}\ (\delta^{57/56}Fe_{meas} - \delta^{57/56}Fe_{initial})}{(\delta^{57/56}Fe_{sys} - \delta^{57/56}Fe_{initial})} \quad (3)$$

where $\delta^{57/56}Fe_{meas}$ represents observed isotope ratio in aqueous or residual extractions, $\delta^{57/56}Fe_{initial}$ is the starting isotope composition for aqueous Fe(II) or goethite Fe(III), and $\delta^{57/56}Fe_{sys}$ is the mass-balance weighted average isotope distribution calculated using equation 2. Calculated exchange values are presented in Table 6.5.

Results of aqueous Fe(II) and Co measurements revealed distinct differences between different magnetites over 30 d. Stoichiometric magnetite (X = 0.51) stimulated minor Fe(II) uptake from solution, while non-stoichiometric magnetite (X = 0.27) removed nearly all aqueous Fe(II). Magnetite in which Co(II) had been substituted for Fe(II) (X_{Co} = 0.41) removed an intermediate amount of Fe(II), corresponding to an intermediate initial (II):(III) ratio between the two Fe-only magnetites. Fe(II) uptake was

not immediate, as with goethite in Chapters 3 and 4, but rather occurred over a period of several days in NS-magnetite and Co-magnetite. Reaction of Co-substituted magnetite with aqueous Fe(II) prompted increasing release of Co into solution, suggesting cation exchange occurs is occurring within the magnetite structure. No Co was detected in control reactors of Co-substituted magnetite suspended in pH 7.2 buffer without aqueous Fe(II).

Acid extracts were performed to remove Fe(II) to an extent comparable to average net Fe(II) loss from solution during reaction, meaning different magnetite solids required different solution conditions for extraction (Table 6.1). Fe(II) recovery from non-stoichiometric magnetite was high, but generally decreased over time, suggesting Fe(II) taken up from solution is becoming more recalcitrant in the solid phase. Fe(II) amounts added were not enough to make non-stoichiometric magnetite have a fully-stoichiometric character (X after Fe(II) uptake = $X_{Fe(II)} = 0.40$), suggesting any added Fe(II) was being fully incorporated, perhaps moving into interior regions of the solid phase. Interestingly, an increasing amount of Fe(II) could be removed during the extraction of Co-magnetite, but much less Co was released into solution, despite evidence for Co release into aqueous phase samples after Fe(II) addition, shown in Figure 6.1. Co was released into solution during reactions with Fe(II), but most Co remaining in the solid phase appears resistant to extraction. Co resistance to extraction could be due to retention within interior regions of the particle, or solubility changes as Co(II) is oxidized to Co(III), which is much less stable at pH 7.2.

Aqueous Fe isotope ratios changed the least in Co-magnetite samples, nearing 600‰ and seeming to plateau over the last two weeks of reaction (Figure 6.3, Table 6.4). S-magnetite isotope ratios in the aqueous phase dropped more rapidly in early time points, but $\delta^{57/56}$Fe values entered a stage of more gradual exchange after ~ 1 d (Table 6.2). NS-magnetite isotope ratios started changing slowly, but around 1-2 days $\delta^{57/56}$Fe values actually decreased below S-magnetite samples and remained lower for remaining

time points (Table 6.3). Isotope ratios changed slowly for NS-magnetite at early time points, which corresponded to the time when significant Fe(II) was being incorporated into the solid phase. During this "net Fe(II) uptake" phase, it seems reasonable to expect that not much isotopically-light Fe(II) from magnetite would be entering the solid phase. After a majority of Fe(II) was taken up into solution, $\delta^{57/56}$Fe values started to change more rapidly, perhaps indicating redox-driven atom exchange could be established when an adequate amount of structural Fe(II) was obtained.

Stoichiometric magnetite isotope ratios for all three Fe fractions display interesting trends over 30 d (Figure 6.4). Aqueous Fe(II) and extracted Fe(II) appear to come from different reservoirs initially, as extracted Fe(II) is isotopically lighter at 10 min. These two Fe reservoirs quickly reach similar values, however, and remain nearly identical for remaining time points. Residual solids $\delta^{57/56}$Fe values increase from 0.07‰ to ~ 32‰, indicating a significant enrichment in ^{57}Fe. None of the extracts, however, appear to reach the $\delta^{57/56}Fe_{sys}$ value calculated for this system (59.63‰, from equation 2, dashed line), indicating complete Fe exchange with S-magnetite solids was not achieved in 30 d.

In non-stoichiometric magnetite trials, extracted Fe(II) appears to rise initially to match aqueous Fe(II) isotope data , but the two components never converge (Figure 6.5). A difference of ~ 50‰ is maintained between aqueous Fe(II) and extracted Fe(II) for the duration of the experiment. Aqueous Fe(II) isotope ratios become lighter for NS-magnetite than S-magnetite, and residual solids $\delta^{57/56}$Fe values display a greater enrichment in ^{57}Fe than S-magnetite as well, climbing from 0.08‰ to ~ 41.40‰. Higher measured ^{57}Fe incorporation for NS-magnetite could be expected, as significantly more Fe(II) was taken up from solution than in trials involving S-magnetite.

Co-magnetite has ~ 2/3 of the Fe initially present in other magnetite samples, due to cation substitution with Co, so the calculated $\delta^{57/56}Fe_{sys}$ value is noticeably higher (80.99‰, dashed line Figure 6.6). Much less change in Fe isotope ratios is observed in

aqueous Fe(II) samples. Extracted Fe(II) isotope ratios rise much higher in this case in order to converge with aqueous Fe(II), but incomplete convergence is again observed, with a constant separation of ~ 20‰. Interestingly, the degree of convergence between aqueous Fe(II) and extracted Fe(II) isotope ratios appears inversely proportional to Fe(II) uptake / extraction masses. It is not yet known whether this effect is due to larger Fe(II) uptake from solution, or a simply a result of greater Fe(II) extraction from the particles during sampling.

All three magnetite samples appear to have stabilized after 30 d, and none of the three magnetite solids were able to achieve 100 % exchange with aqueous Fe(II), according to equation 3 in the text (Figure 6.7, Table 6.5). NS-magnetite appears to have undergone more Fe atom exchange than S-magnetite , perhaps due to the greater net association between Fe(II) and magnetite in this case. In S-magnetite, Fe(II) sites were already filled to capacity, reducing potential driving forces for Fe(II) incorporation. Typically, equation 3 provides good agreement between values calculated using aqueous Fe(II) data or residual Fe solids data, as is the case in Chapter 4 and here with S-magnetite. NS-magnetite % Fe exchange values are reasonably similar, but Co-magnetite values are quite different between aqueous Fe(II) and residual solids calculations. This discrepancy could be due to replacement of Co for isotopically heavy Fe in the solid phase, while some of the cations released to solution were Co atoms, and thus not included in stable Fe isotope analysis. Analysis of only aqueous Fe(II) data, as is commonly seen in other work (*14, 96*), could potentially under-represent the actual amount of exchange occurring in cation-substituted solids.

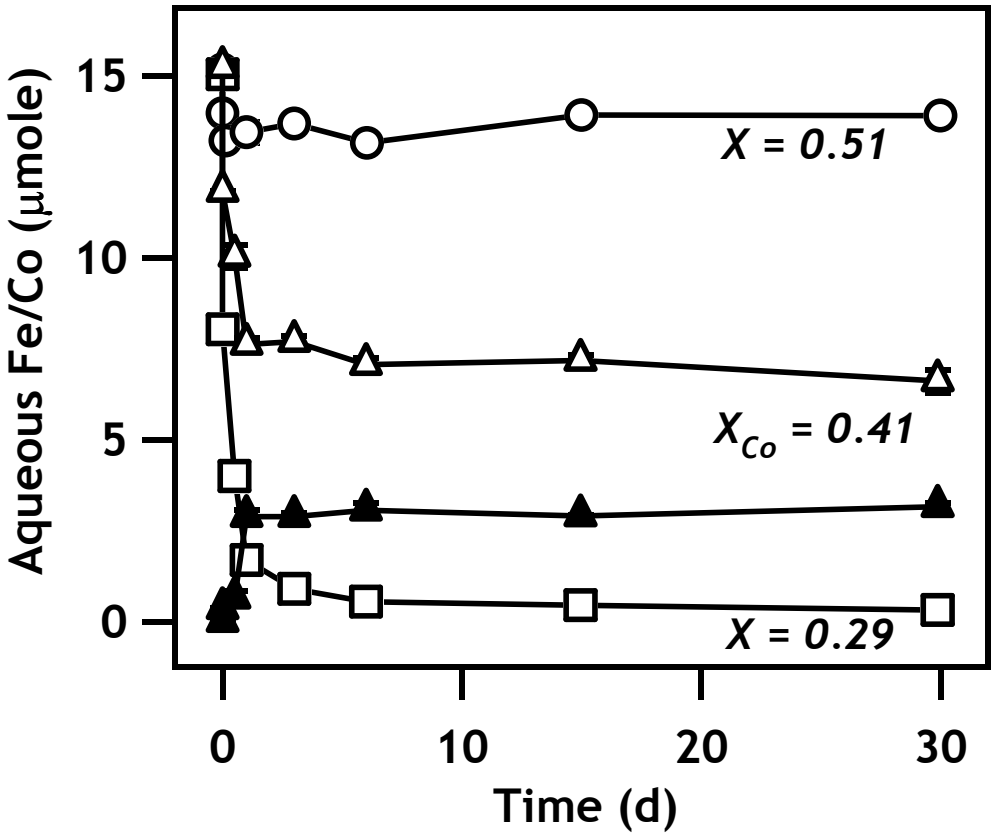

Figure 6.1 Colorimetric measurements of Fe(II) and Co concentrations over 30 d. Initial Fe(II) masses in all reactors were ~ 15.2 µmol. Stoichiometric magnetite (circles, X = 0.51), non-stoichiometric magnetite (squares, X = 0.27), and cobalt-substituted magnetite (triangles, X_{Co} = 0.41) stimulated different amounts of Fe(II) uptake from solution. Co-magnetite also released Co (dark triangles) into solution over 30 d after aqueous Fe(II) was added.

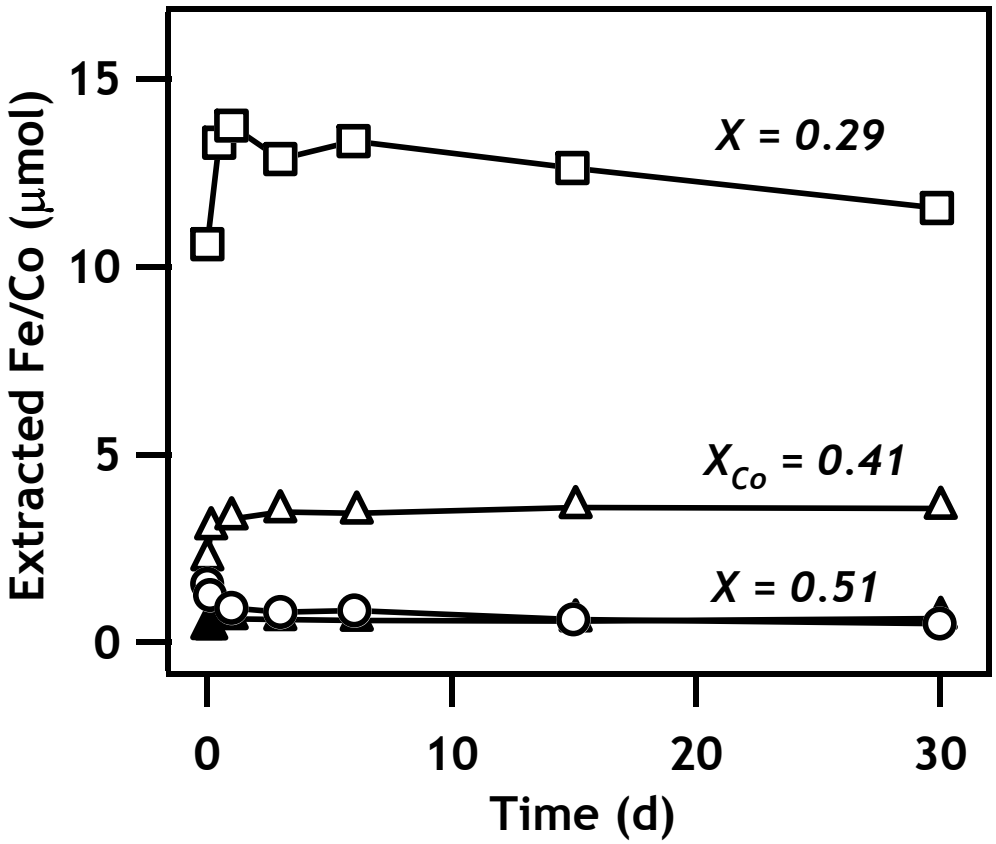

Figure 6.2 Extracted Fe(II) and Co from batch reactors. Data markers are similar to Figure 6.1.

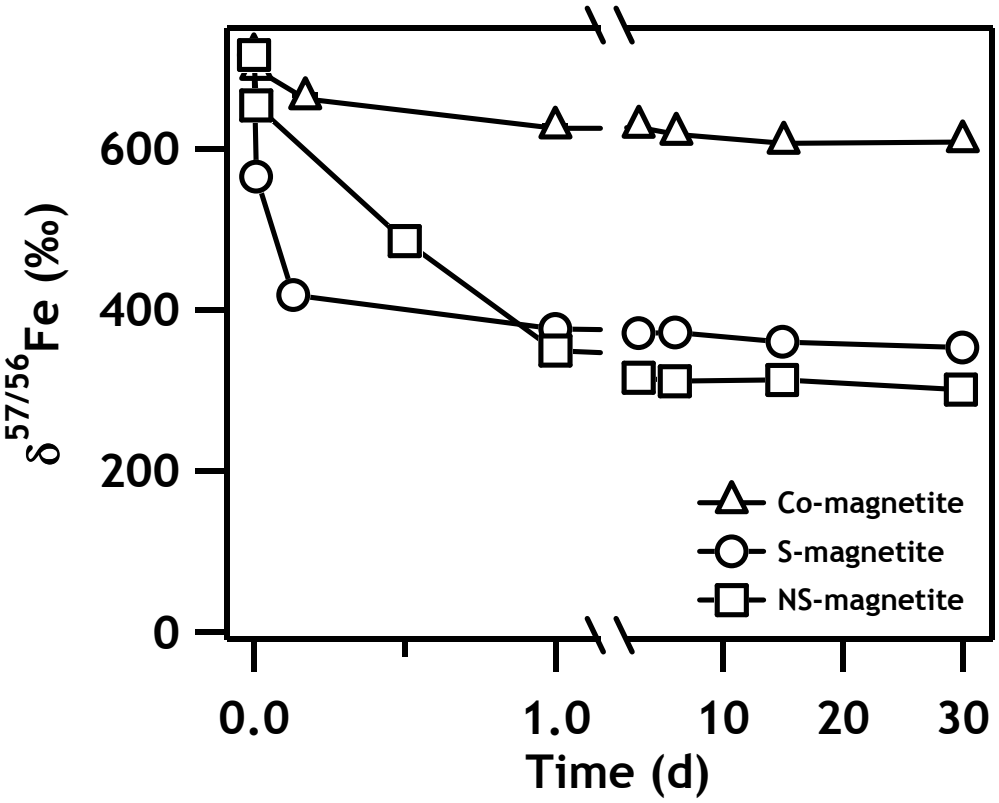

Figure 6.3 $\delta^{57/56}$Fe values for aqueous phase Fe(II) recovered over 30 d of reaction with three magnetite samples.

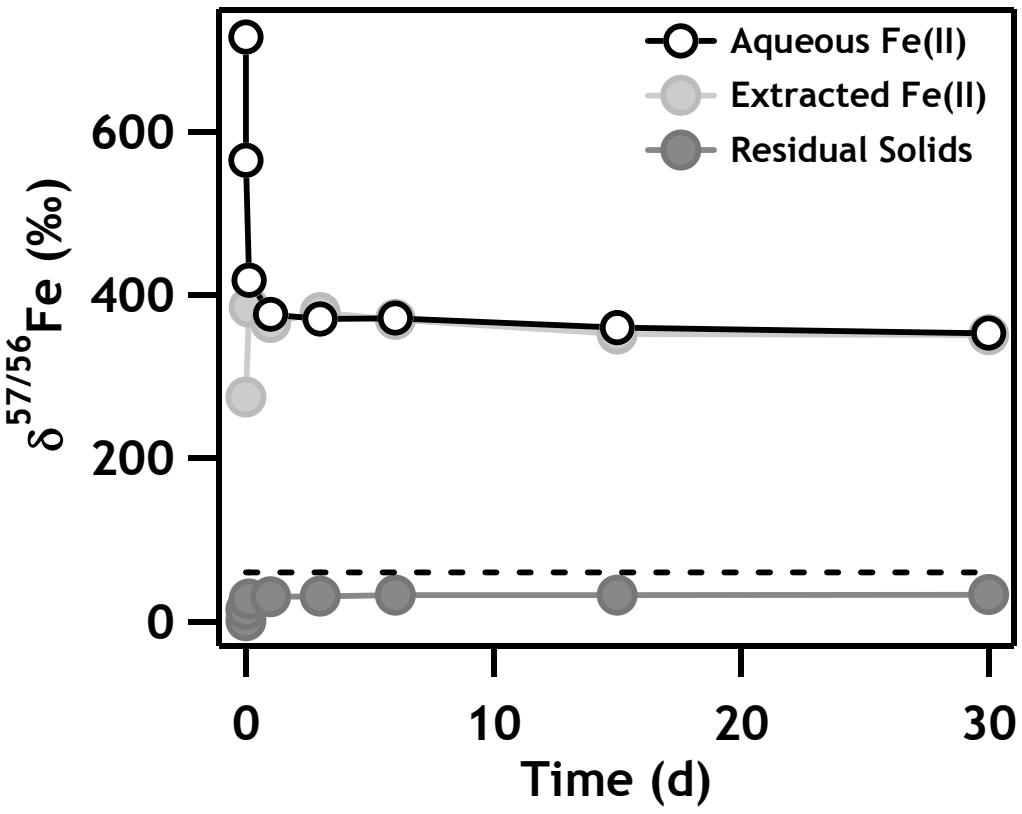

Figure 6.4 $\delta^{57/56}$Fe values for three S-magnetite extractions over 30 d.

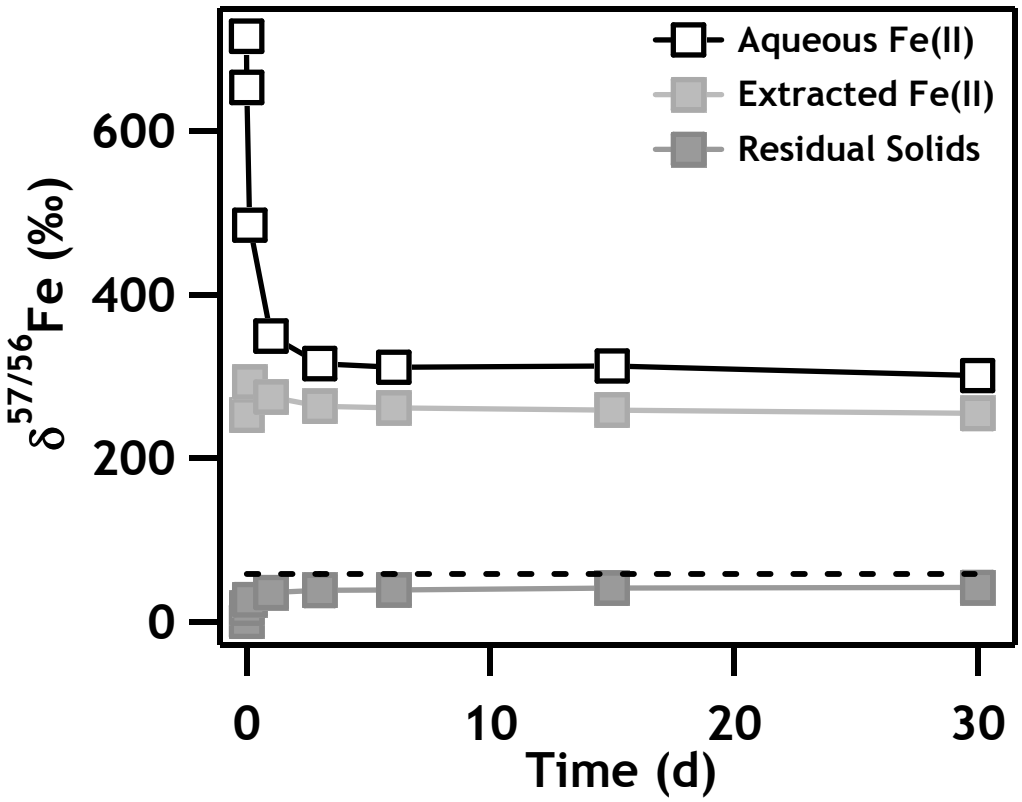

Figure 6.5 $\delta^{57/56}$Fe values for three NS-magnetite extractions over 30 d (Table 6.3).

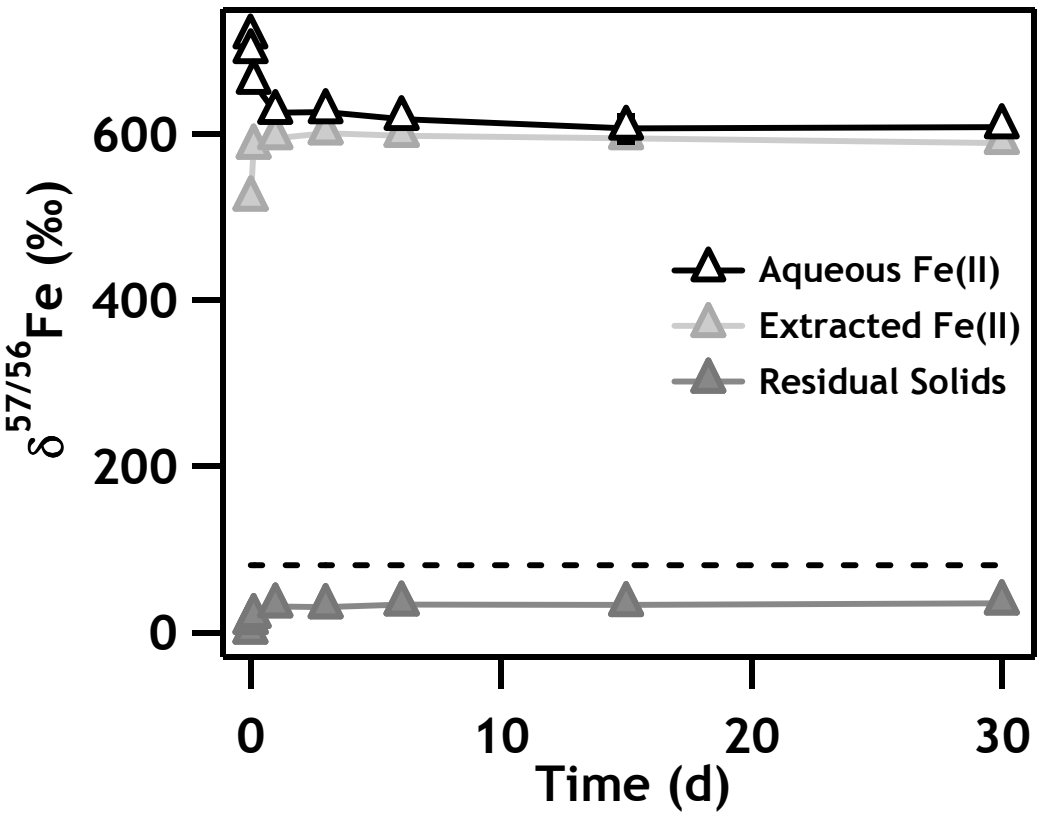

Figure 6.6 $\delta^{57/56}$Fe values for three Co-magnetite extractions over 30 d

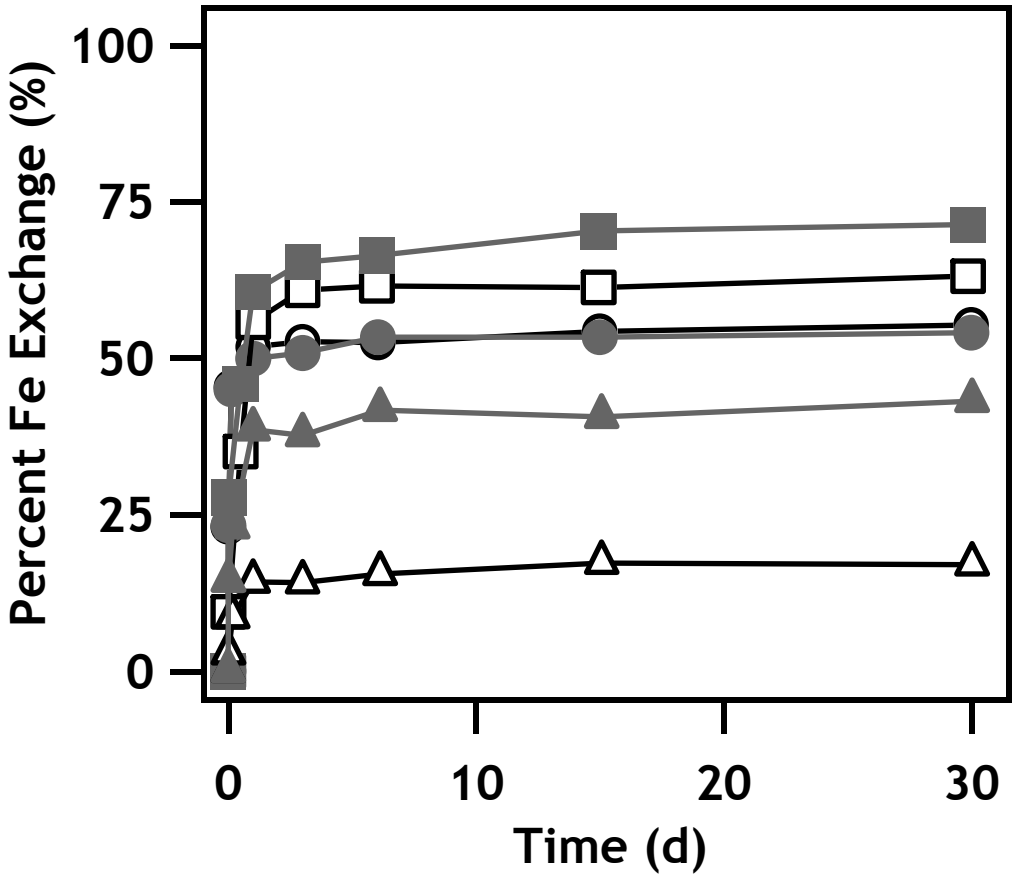

Figure 6.7 Percent atom exchange for three magnetite solids exposed to 1 mM Fe(II), determined using equation 3 in the text. Data from stoichiometric magnetite (S-magnetite, circles), non-stoichiometric magnetite (NS-magnetite, squares), and cobalt-substituted magnetite (Co-magnetite, triangles) is included. Percent exchange values calculated using aqueous $\delta^{57/56}$Fe data are displayed as open markers, while exchange values calculated from residual solids $\delta^{57/56}$Fe data are depicted as filled markers.

Table 6.1 Summary of Fe(II) extraction procedures for Fe-isotope tracer study.

	S-Magnetite	NS-Magnetite	Co-Magnetite
Extraction protocol	5 mL 50 mM MOPS pH 7.2, 20 min	5 mL 25 mM acetic acid pH 3.1, 45 min	5 mL 25 mM acetic acid pH 3.1, 60 min

Table 6.2 Summary of experimental data for Fe isotope tracer experiment with stoichiometric magnetite (S-magnetite).

	Aqueous Fe(II)		Extracted Fe(II)		Residual Solids		
Time (d)	Fe(II) mass (μmol)	$\delta^{57/56}$Fe (‰)	Fe(II) mass (μmol)	$\delta^{57/56}$Fe (‰)	Fe mass (μmol)	Fe(II) (%)	$\delta^{57/56}$Fe (‰)
0	15.17 (0.09)[a]	715.91 (0.24)			167.16 (6.24)	34.5	0.07 (0.02)
0.01	13.97 (0.00)	564.79 (4.40)	1.55 (0.01)	274.38 (3.47)	172.99 (6.07)	34.4	13.94 (0.11)
0.13	13.21 (0.04)	417.98 (6.29)	1.25 (0.02)	384.55 (17.61)	167.70 (6.17)	34.8	26.88 (0.27)
1.0	13.44 (0.28)	375.79 (7.20)	0.91 (0.03)	366.00 (13.66)	170.44 (3.26)	35.0	29.80 (0.24)
3.0	13.68 (0.05)	370.43 (3.85)	0.80 (0.01)	378.04 (14.31)	169.94 (2.32)	35.1	30.35 (0.16)
6.04	13.15 (0.08)	371.36 (6.71)	0.84 (0.07)	369.59 (6.41)	163.94 (3.19)	36.5	31.83 (0.83)
15.0	13.91 (0.10)	359.66 (6.52)	0.60 (0.03)	351.98 (4.81)	166.77 (5.31)	35.1	31.83 (0.51)
30.0	13.90 (0.07)	352.89 (2.81)	0.49 (0.03)	350.77 (3.51)	170.63 (2.05)	35.2	32.26 (0.23)

[a]- Numbers in parentheses represent 1-standard deviation of triplicate reactors.

Table 6.3 Summary of experimental data for Fe isotope tracer experiment with non-stoichiometric magnetite (NS-magnetite).

	Aqueous Fe(II)		Extracted Fe(II)		Residual Solids		
Time (d)	Fe(II) mass (μmol)	$\delta^{57/56}$Fe (‰)	Fe(II) mass (μmol)	$\delta^{57/56}$Fe (‰)	Fe mass (μmol)	Fe(II) (%)	$\delta^{57/56}$Fe (‰)
0	15.04 (0.09)[a]	715.91 (0.24)			170.85 (4.95)	22.5	0.08 (0.06)
0.01	8.03 (0.05)	653.34 (1.71)	10.59 (0.26)	252.35 (0.24)	157.89 (2.94)	20.2	16.11 (0.48)
0.5	4.00 (0.14)	484.94 (12.83)	13.29 (0.27)	292.94 (3.64)	165.69 (3.18)	20.6	26.66 (0.01)
1.0	1.69 (0.08)	349.05 (4.92)	13.75 (0.13)	274.58 (4.03)	166.76 (2.93)	21.8	35.19 (0.21)
3.0	0.90 (0.11)	315.43 (3.76)	12.86 (0.02)	263.04 (2.53)	171.21 (2.66)	22.5	37.91 (0.47)
6.0	0.55 (0.02)	310.90 (7.58)	13.34 (0.18)	261.16 (5.52)	173.31 (6.16)	22.4	38.53 (0.63)
15.0	0.45 (0.02)	312.54 (1.64)	12.62 (0.10)	258.52 (1.18)	167.03 (1.42)	22.7	40.81 (0.14)
29.9	0.32 (0.00)	300.70 (8.90)	11.55 (0.06)	254.20 (5.85)	165.64 (7.85)	23.3	41.40 (0.72)

[a]- Numbers in parentheses represent 1-standard deviation of triplicate reactors.

Table 6.4 Summary of experimental data for Fe isotope tracer experiment with Co-substituted magnetite (Co-magnetite).

	Aqueous Fe(II)			Extracted Fe(II)			Residual Solids			
Time (d)	Fe(II) mass (μmol)	$\delta^{57/56}$Fe (‰)	Co mass (μmol)	Fe(II) mass (μmol)	$\delta^{57/56}$Fe (‰)	Co mass (μmol)	Fe mass (μmol)	Fe(II) (%)	$\delta^{57/56}$Fe (‰)	Co mass (μmol)
0	15.21 (0.14)[a]	715.91 (0.24)					119.31 (2.10)	0	0.05 (0.04)	49.03 (0.69)
0.01	11.81 (11.81)	698.01 (0.08)	0.35 (0.02)	2.19 (0.02)	520.72 (0.01)	0.36 (0.01)	121.27 (4.03)	1.2	11.70 (0.08)	42.63 (1.68)
0.17	10.03 (0.31)	661.46 (5.81)	0.64 (0.20)	3.01 (0.07)	583.20 (4.77)	0.35 (0.06)	119.44 (0.48)	3.3	18.62 (1.74)	40.86 (0.18)
1.0	7.61 (0.18)	625.16 (2.92)	2.88 (0.18)	3.28 (0.03)	594.39 (3.59)	0.62 (0.04)	124.51 (0.83)	0.7	31.28 (0.93)	39.01 (0.60)
3.0	7.69 (0.17)	626.15 (2.63)	2.88 (0.12)	3.46 (0.03)	600.42 (1.65)	0.60 (0.02)	122.67 (1.64)	0.8	30.51 (0.54)	40.86 (1.03)
6.1	7.06 (0.19)	617.41 (3.88)	3.06 (0.22)	3.43 (0.01)	597.60 (1.01)	0.58 (0.06)	124.46 (1.10)	1.0	33.80 (0.92)	36.75 (0.20)
15.1	7.17 (0.15)	606.15 (15.08)	2.90 (0.03)	3.58 (0.07)	594.52 (2.84)	0.56 (0.02)	121.41 (2.65)	1.6	32.90 (0.37)	38.53 (1.12)
30.0	6.61 (0.32)	607.85 (4.14)	3.16 (0.09)	3.56 (0.03)	588.53 (4.27)	0.63 (0.03)	124.44 (3.58)	0.7	34.95 (0.34)	38.18 (1.47)

[a]- Numbers in parentheses represent 1-standard deviation of triplicate reactors.

Table 6.5 Calculated Fe exchange represented by $\delta^{57/56}$Fe values in aqueous and residual solids compartments.

	S-Magnetite		NS-Magnetite		Co-Magnetite	
Time[a] (d)	Aqueous Fe(II) (%)	Residual Solids (%)	Aqueous Fe(II) (%)	Residual Solids (%)	Aqueous Fe(II) (%)	Residual Solids (%)
0.007	23.0	23.3	9.5	27.7	2.8	14.4
0.17	45.4	45.0	35.1	45.9	8.6	23.0
1	51.8	49.9	55.8	60.6	14.3	38.6
3	52.6	50.8	60.9	65.3	14.1	37.6
6	52.5	53.3	61.6	66.4	15.5	41.7
15	54.3	53.3	61.3	70.3	17.3	40.6
30	55.3	54.1	63.1	71.3	17.0	43.1

[a]- Sampling times were similar, but not identical, for every type of magnetite solid, and values listed here represent "ballpark" times for each sampling period.

CHAPTER 7: ENGINEERING AND SCIENTIFIC SIGNIFICANCE

Summary

The studies described in thesis attempt to unravel fundamental processes to explain macroscopic redox behavior of Fe and Mn oxides exposed to aqueous Fe(II). Scenarios in which Fe and Mn oxides may encounter aqueous Fe(II) are widespread in natural and engineered settings, and reactions involving these common constituents of natural systems play an important role in governing fate and transport of a host of important chemical species. In order to examine specific interactions, we have taken a reductionist approach to our experimental work, but we believe experimental conditions used (relevant solids loading, solution pH, Fe(II) concentrations) are reasonable to simulate groundwater systems. These findings serve as a reminder that the absence of an observable net reaction does not mean that chemical species are static and unreactive. Results of these studies also demonstrate important redox mechanisms that could influence chemical reactivity of Fe and Mn oxides in real systems and future attempts to characterize or predict environmental outcomes should include a consideration of these effects.

Goethite is a prevalent Fe oxide that has been demonstrated to occur naturally in the nanoscale. In our studies of goethite nanorods and microrods, we have observed similar macroscopic reactivity of goethite solids with aqueous Fe(II) at circum-neutral pH, despite large differences in primary particle size. Particle aggregation, as opposed to intrinsic reactivity differences between nanoscale and bulk material, was found to provide the most satisfactory explanation of observed results. This result should temper the expectations of scientists eager to explain altered reactivity of nanoscale materials in terms of fundamental particle behavior, without considering implications of macroscopic behavior in aqueous suspensions. This study also highlights the importance of considering reactive surface area for heterogeneous reactions in aqueous systems, which

may not be comparable to estimated of available surface area using characterization data from dried solid samples. Characterizing particle aggregation using complementary techniques may not provide a quantitative measurement of reactive surface area, but studies of this nature can quickly determine whether such macroscopic behavior may be important in a specific heterogeneous system.

We have endeavored to extend our understanding of interfacial redox processes between Fe(II) and Fe oxides. Our work has demonstrated the clear utility of stable isotope tracer studies to examine these mechanisms, especially when measurements of solid phase Fe isotopes can be used to complement aqueous Fe measurements. Our demonstration of extensive Fe atom cycling in goethite during Fe(II) exposure builds on the work of others to completely alter prevailing notions of a passive solid phase in heterogeneous redox reactions. Chemically-induced surface potential gradients have been demonstrated in other Fe oxides, and our experimental studies using different experimental conditions and sequential extractions seem to support the existence of a similar mechanism in goethite, which is corroborated by molecular simulations. Fe oxides can be viewed as being in competition with other oxidized species for electrons from aqueous Fe(II), which has implications for the reductive transformation processes of a host of oxidized contaminants. Extensive restructuring of Fe oxides in the presence of aqueous Fe(II) also have clear implications for availability of co-precipitated or substituted heavy metals, which are important aspects of Fe oxide chemistry in natural systems. Our preliminary work with magnetite demonstrates important differences that may exist between Fe oxides in rates and extent of redox-drive Fe-atom exchange. Important variables like initial Fe(II) content and cation substitution, which occur to varying degrees in natural systems, have also been shown to influence Fe atom cycling in this work.

Interactions between manganese oxides and aqueous Fe(II) can exert important controls on reactivity of groundwater systems. By utilizing complementary techniques,

we are able to characterize the nature of Fe precipitates forming on the surface of pyrolusite at near-neutral pH. Properly characterizing Fe precipitates under relevant conditions will improve our ability to predict reactivity of resulting Mn/Fe particle complexes, as Fe oxides may differ drastically in their reactivity towards other important chemical species. Through our selective use of Fe isotopes in combination with ^{57}Fe Mossbauer spectroscopy, we are able to characterize the chemical fate of Fe(II) introduced to Mn/Fe particles at any point during their continued reaction. Through this approach we have shown that, contrary to popular opinion, Fe precipitates do not completely inhibit redox activity of manganese oxides, as Fe precipitates themselves may participate in redox reactions with additional aqueous Fe(II) or act as conduits for reaction with underlying Mn, potentially increasing surface area and overall reactivity.

Recommendations for Future Work

By demonstrating the potential for important macroscopic and intrinsic redox mechanisms to govern reactivity of heterogeneous Fe-Fe and Fe-Mn systems, our work will prompt many new directions for future research.

Particle aggregation was shown to be an important factor when considering reactivity of goethite with aqueous Fe(II). Our work was only performed under a few solution conditions, which could easily be expanded in future studies to include different pH regimes, influences of organic or inorganic adsorbents, and different Fe oxides of varying primary particle sizes. Presumably, aggregation of goethite nanorods can also explain reactivity towards other groundwater constituents. The potential for particle aggregation to impact a variety of processes, such as heavy metal adsorption or surface-catalyzed hydrolysis of pesticides, should be explored in order to examine overall relevance of aggregation in Fe oxide reactivity.

Our work involving redox-driven atom exchange between aqueous Fe(II) and goethite could also be explored under a variety of permutations, as our initial work was

only performed under a few set experimental conditions. Solution pH, ionic strength, Fe(II) loading, or availability of Fe(II)-complexing agents are relatively easy parameters to alter in order to further investigate process contributing to the overall mechanism. Considerations of molecular simulations concerning a variety of these specific details will ultimately improve our experimental design and interpretation of results. Cation substitution could potentially influence redox-driven atom exchange, and is an important natural phenomenon in goethite that merits consideration.

Other Fe oxides will need to be surveyed to assess potential for redox-driven atom exchange. Studies have already been initiated on magnetite and hematite. Results presented on magnetite highlight the importance of solids characteristics (Fe(II) content, cation substitution) in controlling rates and extent of Fe atom exchange. Extensive solid-phase characterization similar to the work conducted on goethite will be performed to complement observed isotope shifts. Optimizing extraction procedures to recover relevant "components" of Fe(II)-Fe oxide systems can also be varied in this case, in order to investigate the observed separation between aqueous and extracted Fe(II) isotope signatures.

There is also room for a variety of permutations of our work with manganese oxide reactivity towards aqueous Fe(II). Naturally-occurring manganese oxides are typically more unstable and have a higher primary particle surface area than commercially-available pyrolusite used in this study. Manganese oxide synthesis to yield different phases and morphologies will open the door for a quantitative assessment of the importance of Mn oxide phases to initial and evolving reactions with aqueous Fe(II). Our current interpretation of experimental results is also hampered by an accurate assessment of prevalent Mn oxidation states before and after reactions with Fe(II), which could potentially be assessed using spectroscopic techniques such as EXAFS.

APPENDIX: SUPPLEMENTAL INFORMATION

Supplemental Information for Chapter 2

This section contains Mössbauer spectra of dry nanorods and microrods, a plot of the relationship between geometric specific surface area and particle size for nanorods, TEM images of ^{56}Fe goethite particles, SEM images of particles from goethite suspensions, results from batch experiments examining the rate and pH-edge behavior of Fe(II) sorption on goethite, and sedimentation plots for goethite as a function of pH.

Supplemental Information for Chapter 3

In the following section we present five additional figures. Figure S1 displays the initial conditions for the isotope tracer study. Figure S2 displays the measured aqueous Fe(II) concentration in our batch reactors over the course of thirty days, alongside the measured isotopic composition of the aqueous Fe(II) during the same timecourse. Although aqueous Fe(II) concentrations reach a stable plateau after only a few minutes, the $\delta^{57/56}$Fe value of the aqueous phase continues to change over the course of the experiment, indicating that rapid and extensive atom exchange is occurring between aqueous Fe(II) and the goethite Fe(III) atoms. Figure S3 displays XRD patterns collected after goethite solids were allowed to react at pH 7.5 in the presence or absence of 1 mM aqueous Fe(II). Resulting patterns indicate that goethite is the only solid Fe phase present, and the differences between goethite crystal structures are negligible.

In Figure S4, high resolution TEM images of particles exposed to aqueous Fe(II) still have lattice spacings indicative of goethite, although the changes in crystallinity may have occurred when comparing these images with unreacted goethite rods. TEM images of the goethite particles mixing for 30 d with or without exposure to aqueous Fe(II) are shown in Figure S5. It was observed that overall goethite morphology and particle dimensions do not change with the addition of aqueous Fe(II).

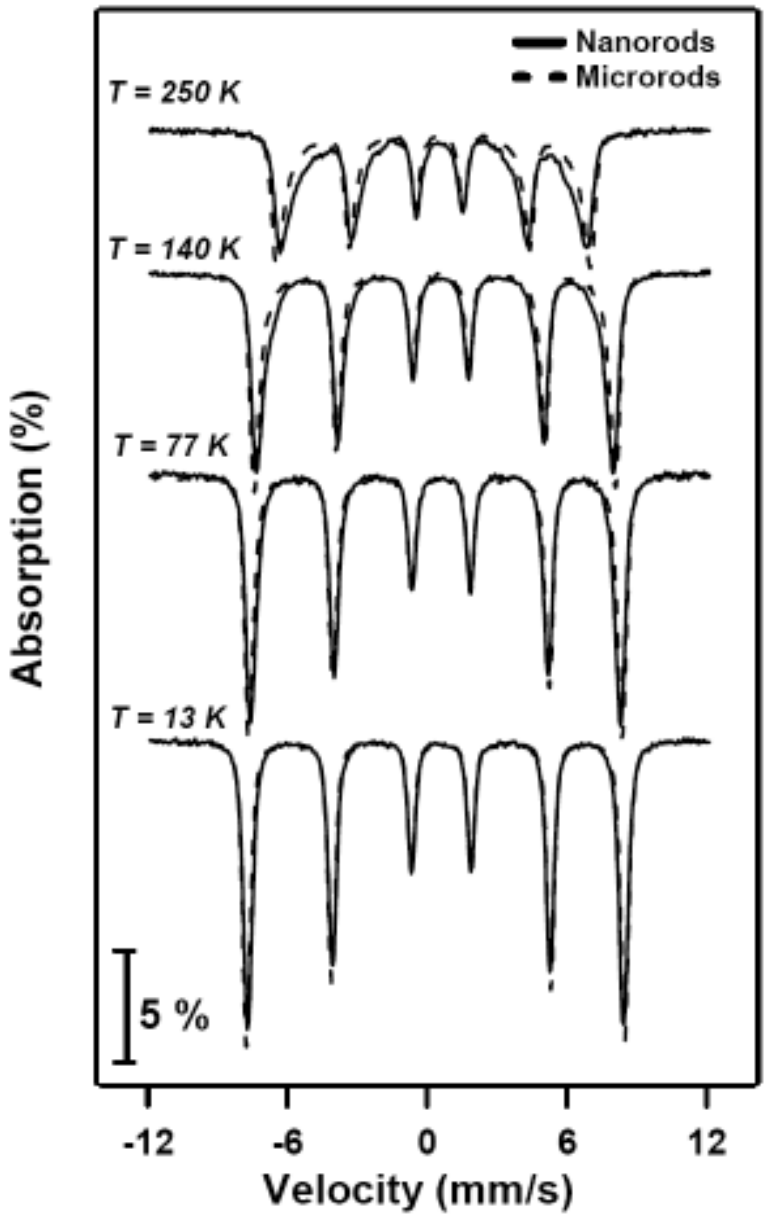

Figure A1 Mössbauer spectroscopy temperature profiles for goethite nanorods and microrods synthesized from naturally abundant iron starting materials. Mössbauer spectra collected at 298,250 and 140 K revealed less magnetic ordering in nanorods relative to microrods. Differences inmagnetic ordering observed from the Mössbauer characterization of these particles were subtle, however, and by 77 K, both the nanorods and microrods had achieved full magnetic ordering.

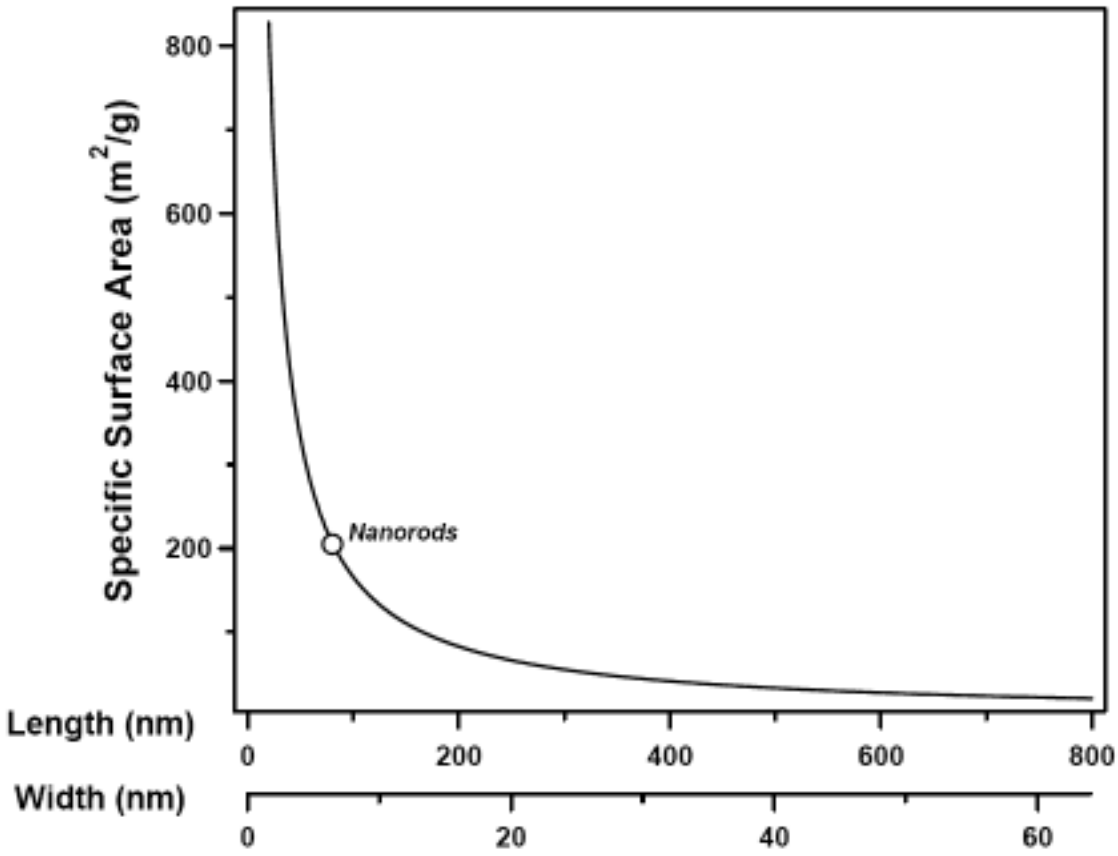

Figure A2 Relationship between goethite dimensions and specific surface area calculated by modeling the geometry of a goethite particle as a rhomboidal prism. Calculations assumed a goethite density of 4.26 g/cm3 and a particle aspect ratio (length:width) of 12.3, which is equal to that determined for nanorods via TEM particle size analysis. The dimensions and specific surface area of the nanorods investigated in the current study are noted. The dimensions and surface area of intermediate rods and microrods are not shown, as they exhibited a different aspect ratio (~25) relative to nanorods.

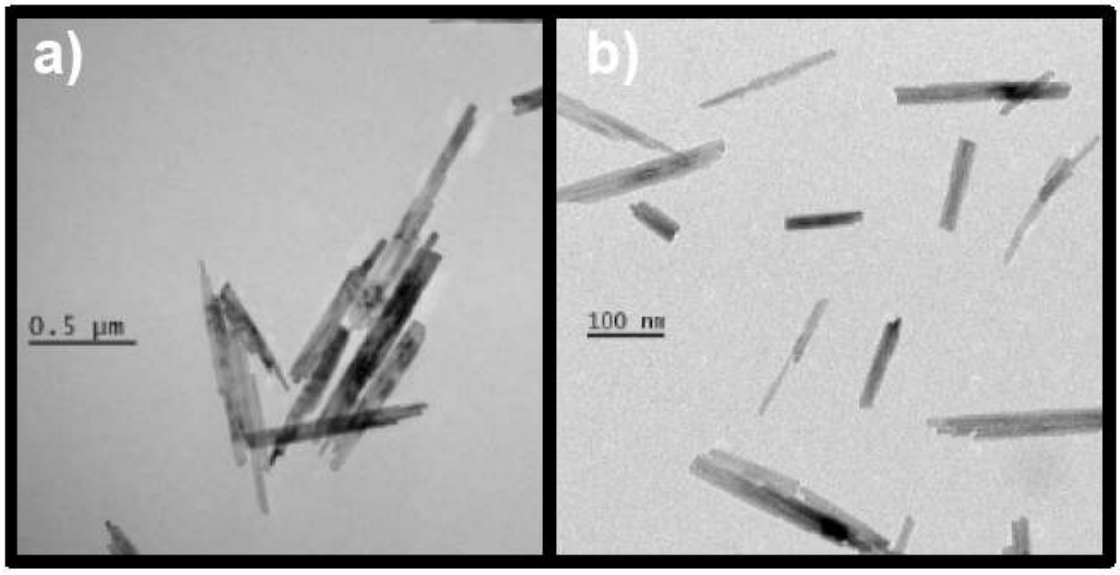

Figure A3 Representative TEM images of (a) ^{56}Fe microrods and (b) ^{56}Fe nanorods. Nanorods exhibited a tendency to adhere to one another.

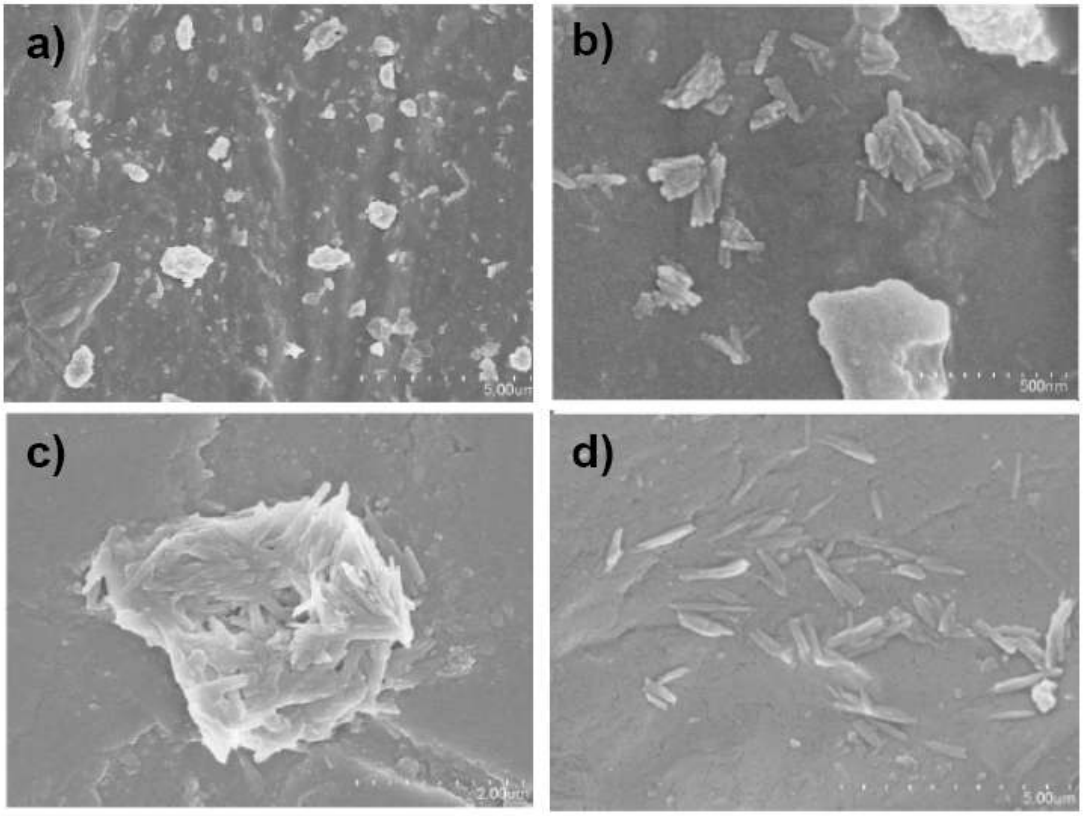

Figure A4 SEM images collected of nanorod (a and b) and microrod (c and d) suspensions at pH 7.5 after 30 minutes of settling time.

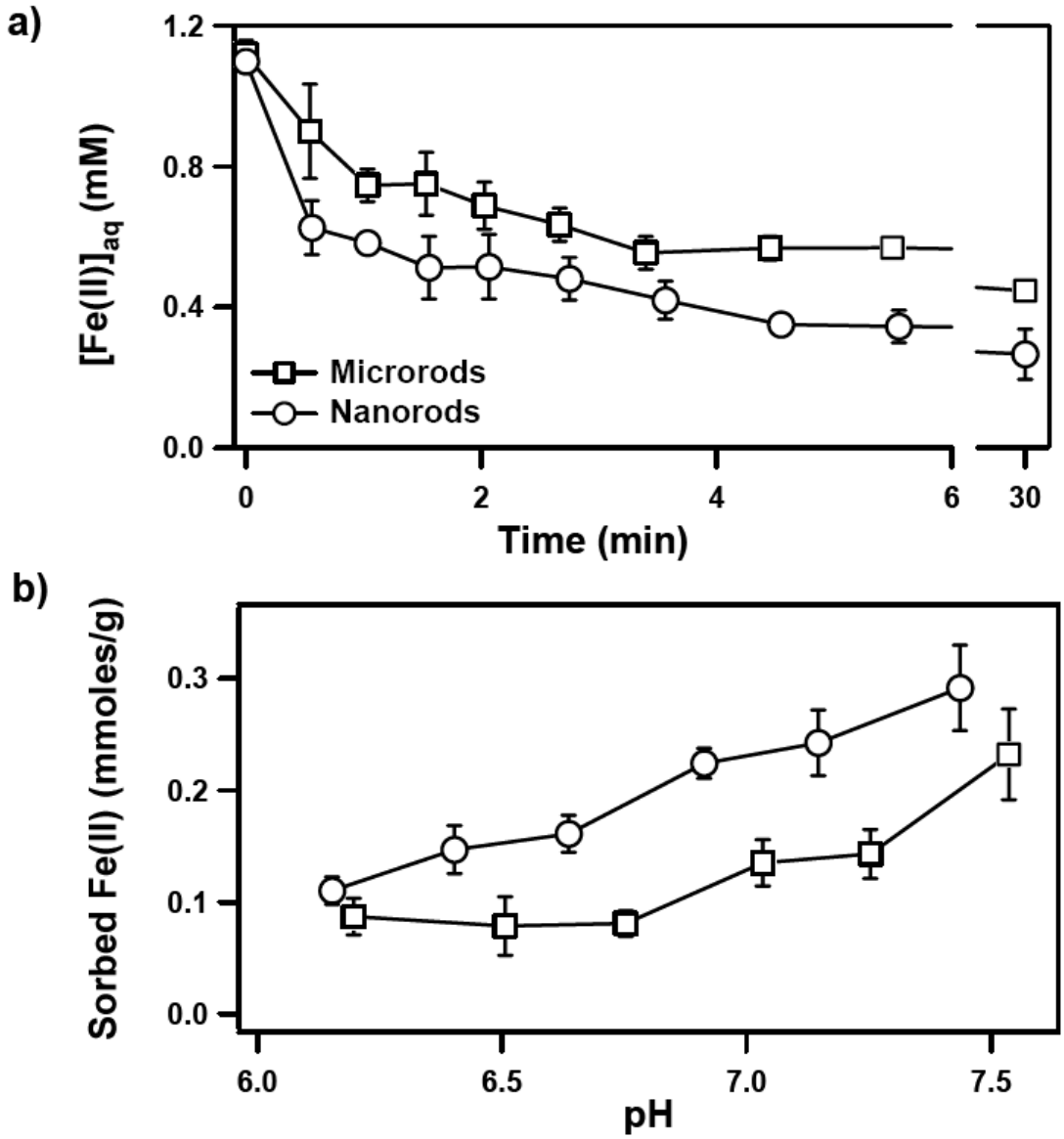

Figure A5 Results of batch studies examining (a) the rate and (b) the pH-edge behavior for Fe(II) sorption on goethite. Rate experiments were conducted at pH 7.5 in 25 mM HEPES buffer with 25 mM KBr, using 4 g/L goethite (60 mg into 15 mL) and an initial aqueous Fe(II) concentration of 1 mM. Reactors were slowly mixed end-over-end at 9 rpm. pH-edge experiments were conducted in 25 mM PIPES buffer with 25 mM KBr and an initial aqueous Fe(II) concentration of ~1 mM. Uncertainties represent one standard deviation determined from triplicate experiments.

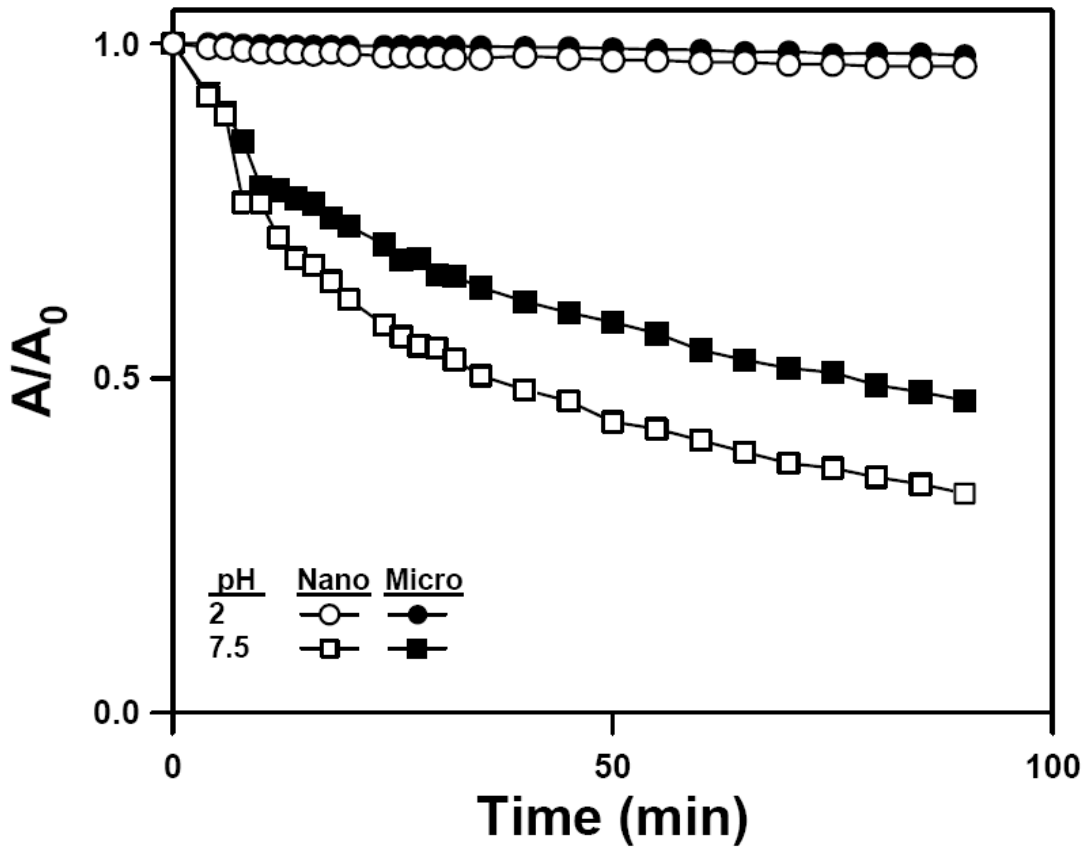

Figure A6 Sedimentation plots for nanorods and microrods shown as a function of pH for a fixed mass loading of 0.2 g/L. Suspensions were prepared in either 0.01 N HCl (pH 2.0) or 25 mM HEPES (pH 7.5). The ionic strength of all systems was adjusted to 25 mM with KBr. Normalized absorbance values correspond to the amount of light at wavelength 510 nm transmitted through a 1 cm path length cell containing goethite suspensions.

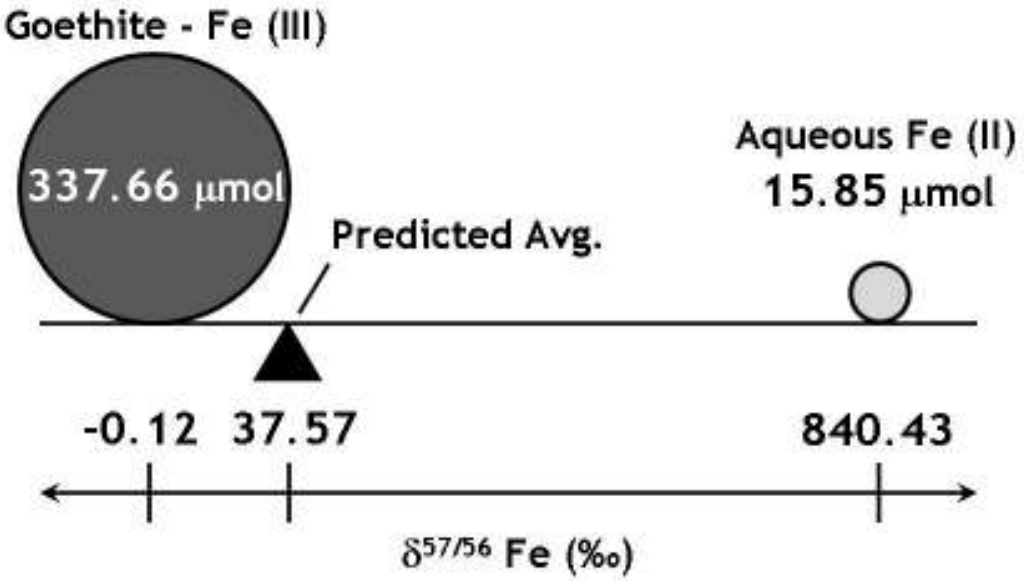

Figure A7 Balance diagram illustrating the initial mass and Fe isotope composition of the aqueous and goethite Fe in the ^{57}Fe(II) tracer study. The positions of the two circles along the schematic $\delta^{57/56}$ Fe scale give the initial isotopic composition of the aqueous and goethite Fe. The fulcrum (▲) of $\delta^{57/56}$ Fe = 37.57‰ represents the mass balance value for complete mixing between aqueous and goethite Fe. Note: distances are not to scale.

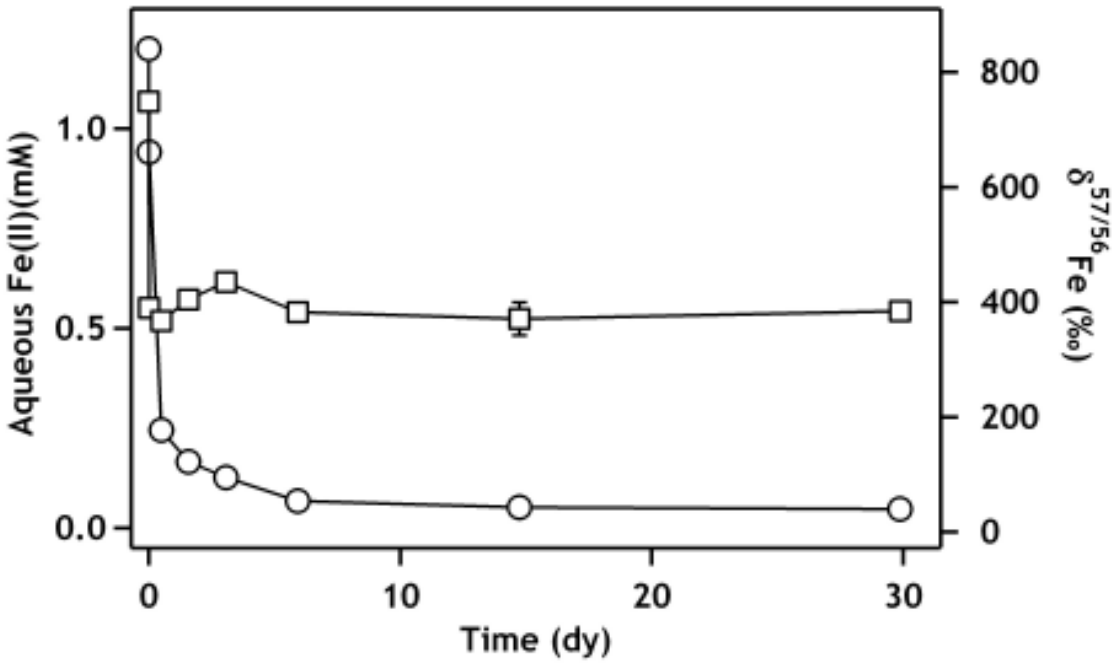

Figure A8 Aqueous Fe(II) concentration (□) and $\delta^{57/56}$Fe values (○) over time in the ^{57}Fe(II) tracer study. Experimental conditions: pH 7.5, 2 g/L goethite solids loading, ~ 1 mM initial aqueous Fe(II). Error bars represent 1-standard deviation of triplicate reactors, and in most cases they are contained within the margins of data markers.

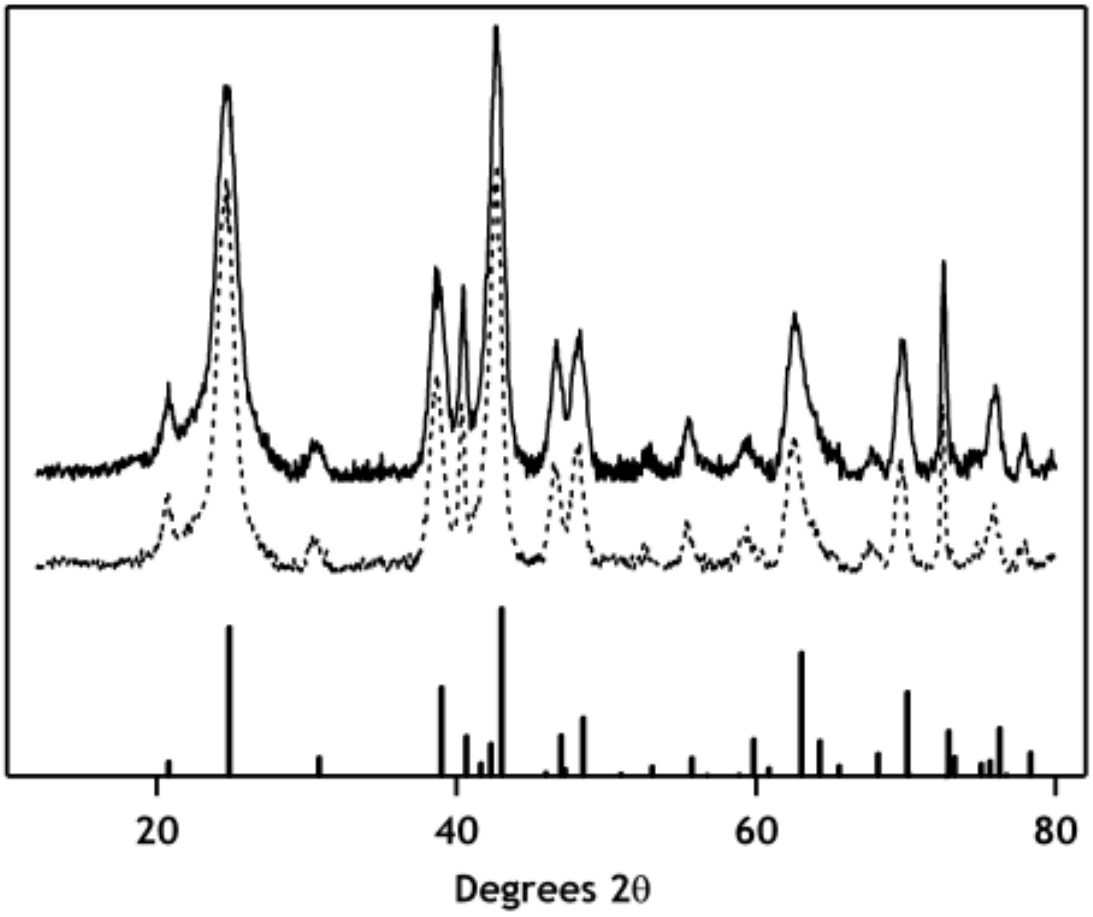

Figure A9 X-ray diffraction (XRD) patterns collected on goethite solids after mixing for 30 d in the presence (dashed line - - -) or absence (solid line ——) of 1 mM Fe(II). Goethite reference peaks are indicated by solid vertical lines below XRD patterns. In each case, no peaks indicating the presence of another Fe phase besides goethite could be detected. The peak width of major goethite reflections are slightly smaller for the goethite sample that was exposed to Fe(II), but the corresponding increase in crystallite size using the Scherrer equation is small (~ 1 nm).

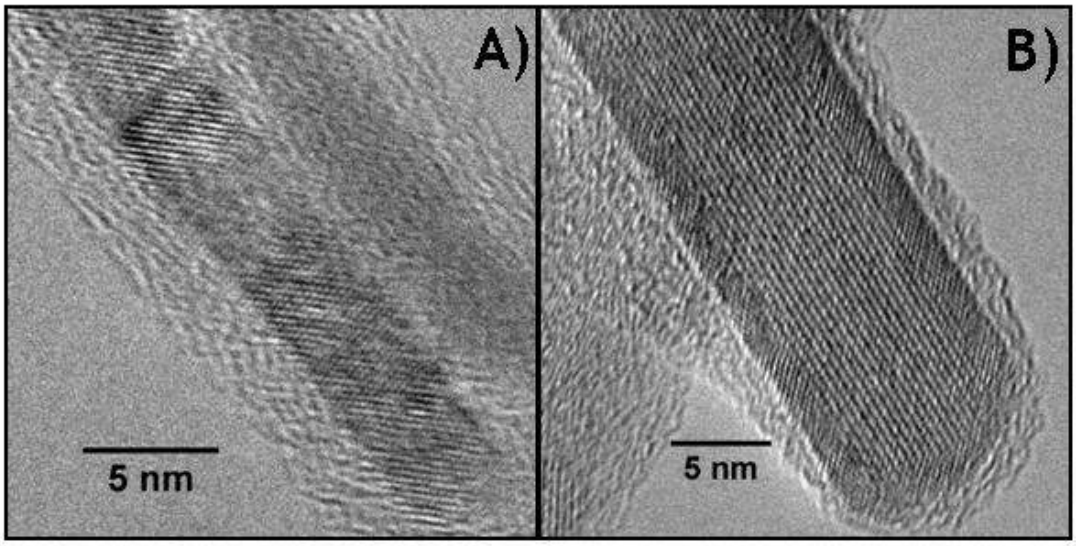

Figure A10 High-resolution TEM (HR-TEM) images of goethite rods after mixing alone (A) or in the presence of 1 mM dissolved Fe(II) (B). Unreacted rods contain lattice fringes that extend to the margins of the particle (A), while the particle imaged in (B) appear to have become more crystalline after reaction with Fe(II), and may have a rind of altered crystallinity. Spacings of lattice fringes in both cases are consistent with goethite. The entire unreacted particle in (A) and the rind of the particle in (B) have lattice spacings of ~2.7 Å, while the interior of the reacted particle in (B) has a lattice spacing of 4.1 Å. Amorphous regions of substance present on the exterior of goethite rods are due to the presence of methanol, which was used in sample preparation.

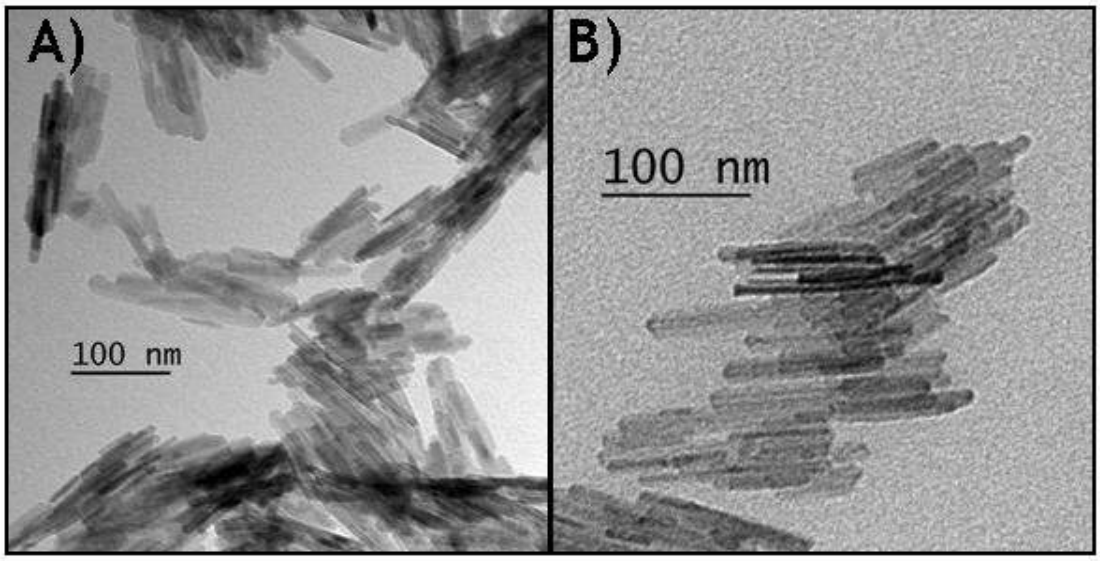

Figure A11 Goethite nanorods imaged with transmission electron microscopy (TEM) after mixing alone (A) or in the presence of 1 mM dissolved Fe(II) (B). No discernable difference in the morphology of the goethite could be detected.

REFERENCES

(1) Klein, C.; Hurlbut, C. S. J., *Manual of Mineralogy*. Wiley: New York, 1999.

(2) VanCappellen, P.; Wang, Y. F. Cycling of iron and manganese in surface sediments: A general theory for the coupled transport and reaction of carbon, oxygen, nitrogen, sulfur, iron, and manganese. *Am. J. Sci.* **1996,** *296*, 197-243.

(3) Bowell, R. J. Sorption of arsenic by iron oxides and hydroxides in soils. *Appl. Geochem.* **1994,** *9*, 279-286.

(4) Heijman, C. G.; Grieder, E.; Holliger, C.; Schwarzenbach, R. P. Reduction of nitroaromatic compounds coupled to microbial iron reduction in laboratory aquifer columns. *Environ. Sci. Technol.* **1995,** *29*, 775-783.

(5) Lovley, D. R.; Giovannoni, S. J.; White, D. C.; Champine, J. E.; Phillips, E. J. P.; Gorby, Y. A.; Goodwin, S. Geobacter-Metallireducens Gen-Nov Sp-Nov, a Microorganism Capable of Coupling the Complete Oxidation of Organic-Compounds to the Reduction of Iron and Other Metals. *Arch. Microbiol.* **1993,** *159*, 336-344.

(6) Luther, G. W.; Popp, J. I. Kinetics of the abiotic reduction of polymeric manganese dioxide by nitrite: An anaerobic nitrification reaction. *Aquat. Geochem.* **2002,** *8*, 15-36.

(7) Klausen, J.; Trober, S. P.; Haderlein, S. B.; Schwarzenbach, R. P. Reduction of substituted nitrobenzenes by Fe(II) in aqueous mineral suspensions. *Environ. Sci. Technol.* **1995,** *29*, 2396-2404.

(8) Liger, E.; Charlet, L.; Van Cappellen, P. Surface catalysis of uranium(VI) reduction by iron(II). *Geochim. Cosmochim. Acta* **1999,** *63*, 2939-2955.

(9) Dixit, S.; Hering, J. G. Sorption of Fe(II) and As(III) on goethite in single- and dual-sorbate systems. *Chem. Geol.* **2006,** *228*, 6-15.

(10) Hansel, C. M.; Benner, S. G.; Fendorf, S. Competing Fe(II)-induced mineralization pathways of ferrihydrite. *Environ. Sci. Technol.* **2005,** *39*, 7147-7153.

(11) Williams, A. G. B.; Scherer, M. M. Spectroscopic evidence for Fe(II)-Fe(III) electron transfer at the Fe oxide-water interface. *Environ. Sci. Technol.* **2004,** *38*, 4782-4790.

(12) Larese-Casanova, P.; Scherer, M. M. Fe(II) sorption on hematite: New insights based on spectroscopic measurements. *Environ. Sci. Technol.* **2007,** *41*, 471-477.

(13) Yanina, S. V.; Rosso, K. M. Linked reactivity at mineral-water interfaces through bulk crystal conduction. *Science* **2008,** *320*, 218-222.

(14) Pedersen, H. D.; Postma, D.; Jakobsen, R.; Larsen, O. Fast transformation of iron oxyhydroxides by the catalytic action of aqueous Fe(II). *Geochim. Cosmochim. Acta* **2005,** *69*, 3967-3977.

(15) Postma, D. Concentration of Mn and separation from Fe in sediments - I. Kinetics and stoichiometry of the reaction between birnessite and dissolved Fe(II) at 10C. *Geochim. Cosmochim. Acta* **1985,** *49*, 1023-1033.

(16) Krishnamurti, G. S. R.; Huang, P. M. The catalytic role of birnessite in the transformation of iron. *Can. J. Soil Sci.* **1987,** *67*, 533-543.

(17) Morgan, J. J.; Stumm, W. S. Analytical chemistry of aqueous manganese. *J. Am. Water Works Assoc.* **1965,** *57*, 107-119.

(18) Amacher, M. C.; Baker, D. A. Redox reactions involving chromium, plutonium, and manganese in soils. PhD Thesis, The Pennsylvania State University, University Park, PA, 1982.

(19) Villinski, J. E.; Saiers, J. E.; Conklin, M. H. The effects of reaction-product formation on the reductive dissolution of MnO2 by Fe(II). *Environ. Sci. Technol.* **2003,** *37*, 5589-5596.

(20) Stone, A. T.; Morgan, J. J. Reduction and Dissolution of Manganese(III) and Manganese(IV) Oxides by Organics .1. Reaction with Hydroquinone. *Environ. Sci. Technol.* **1984,** *18*, 450-456.

(21) Eary, L. E.; Rai, D. Kinetics of chromium(III) oxidation to chromium(VI) by reaction with manganese-dioxide. *Environ. Sci. Technol.* **1987,** *21*, 1187-1193.

(22) Banfield, J. F.; Zhang, H., Nanoparticles in the Environment. In *Nanoparticles and the Environment*, Banfield, J. F.; Navrotsky, A., Eds. The Mineralogical Society of America: Washington, D.C., 2001; Vol. 44, pp 1-58.

(23) Madden, A. S.; Hochella, M. F. A test of geochemical reactivity as a function of mineral size: Manganese oxidation promoted by hematite nanoparticles. *Geochim. Cosmochim. Acta* **2005,** *69*, 389-398.

(24) Cornell, R. M.; Schwertmann, U., *The Iron Oxides: Structure, Properties, Reactions, Occurrence, and Uses*. VCH: New York, 2003.

(25) van der Zee, C.; Roberts, D. R.; Rancourt, D. G.; Slomp, C. P. Nanogoethite is the dominant reactive oxyhydroxide phase in lake and marine sediments. *Geology* **2003,** *31*, 993-996.

(26) Larese-Casanova, P.; Scherer, M. M. Morin transition suppression in polycrystalline ^{57}Hematite (alpha-Fe_2O_3) exposed to ^{56}Fe(II). *Hyperfine Interact.* **2007,** *174*, 111-119.

(27) Hartenbach, A.; Hofstetter, T. B.; Berg, M.; Bolotin, J.; Schwarzenbach, R. P. Using nitrogen isotope fractionation to assess abiotic reduction of nitroaromatic compounds. *Environ. Sci. Technol.* **2006,** *40*, 7710-7716.

(28) Crosby, H. A.; Johnson, C. M.; Roden, E. E.; Beard, B. L. Coupled Fe(II)-Fe(III) electron and atom exchange as a mechanism for Fe isotope fractionation during dissimilatory iron oxide reduction. *Environ. Sci. Technol.* **2005,** *39*, 6698-6704.

(29) Nealson, K. H.; Myers, C. R. Microbial reduction of manganese and iron: New approaches to carbon cycling. *App. Environ. Microbiol.* **1992,** *58*, 439-443.

(30) Lovely, D. R. Microbial Fe(III) reduction in subsurface environments. *FEMS Microbiol. Rev.* **1997,** *20*, 305-313.

(31) Elsner, M.; Schwarzenbach, R. P.; Haderlein, S. B. Reactivity of Fe(II)-bearing minerals toward reductive transformation of organic contaminants. *Environ. Sci. Technol.* **2004,** *38*, 799-807.

(32) McCormick, M. L.; Adriaens, P. Carbon tetrachloride transformation on the surface of nanoscale biogenic magnetite particles. *Environ. Sci. Technol.* **2004,** *38*, 1045-1053.

(33) Gregory, K. B.; Larese-Casanova, P.; Parkin, G. F.; Scherer, M. M. Abiotic transformation of hexahydro-1,3,5-trinitro-1,3,5-triazine by Fe^{II} bound to magnetite. *Environ. Sci. Technol.* **2004,** *38*, 1408-1414.

(34) Gander, J. W.; Parkin, G. F.; Scherer, M. M. Kinetics of 1,1,1-trichloroethane transformation by iron sulfide and a methanogenic consortium. *Environ. Sci. Technol.* **2002,** *36*, 4540-4546.

(35) Hofstetter, T. B.; Heijman, C. G.; Haderlein, S. B.; Holliger, C.; Schwarzenbach, R. P. Complete reduction of TNT and other (poly)nitroaromatic compounds under iron-reducing subsurface conditions. *Environ. Sci. Technol.* **1999,** *33*, 1479-1487.

(36) Strathmann, T. J.; Stone, A. T. Mineral surface catalysis of reactions between Fe^{II} and oxime carbamate pesticides. *Geochim. Cosmochim. Acta* **2003,** *67*, 2775-2791.

(37) Anastasio, C.; Martin, S. T., Atmospheric Nanoparticles. In *Nanoparticles and the Environment*, Banfield, J. F.; Navrotsky, A., Eds. The Mineralogical Society of America: Washington, D.C., 2001; Vol. 44, pp 293-349.

(38) Penn, R. L.; Zhu, C.; Xu, H.; Veblen, D. R. Iron oxide coatings on sand grains from Atlantic coastal plain: High-resolution transmission electron microscopy characterization. *Geology* **2001,** *29*, 843-846.

(39) Poulton, S.; Raiswell, R. Chemical and physical characteristics of iron oxides in riverine and glacial meltwater sediments. *Chem. Geol.* **2005,** *218*, 203-221.

(40) Swartz, C. H.; Ulery, A. L.; Gschwend, P. M. An AEM-TEM study of nanometer-scale mineral associations in an aquifer sand: Implications for colloid mobilization. *Geochim. Cosmochim. Acta* **1997,** *61*, 707-718.

(41) Navrotsky, A., Thermochemistry of Nanomaterials. In *Nanoparticles and the Environment*, Banfield, J. F.; Navrotsky, A., Eds. Mineralogical Society of America: Washington, D.C., 2001; Vol. 44, pp 73-104.

(42) Waychunas, G. A.; Kim, C. S.; Banfield, J. F. Nanoparticulate iron oxide minerals in soils and sediments: Unique properties and contaminant scavenging mechanisms. *J. Nanopart. Res.* **2005,** *7*, 409-433.

(43) Langmuir, D. Particle size effect on the reaction goethite = hematite + water. *Am. J. Sci.* **1971,** *271*, 147-156.

(44) Klabunde, K. J.; Stark, J.; Koper, O.; Mohs, C.; Park, D. G.; Decker, S.; Jian, Y.; Lagadic, I.; Zhang, D. Nanocrystals as stoichiometric reagents with unique surface chemistry. *J. Phys. Chem.* **1996,** *100*, 12142-12153.

(45) Anschutz, A. J.; Penn, R. L. Reduction of crystalline iron(III) oxyhydroxides using hydroquinone: influence of phase and particle size. *Geochem. Trans.* **2005,** *6*, 60-66.

(46) Madden, A. S.; Hochella, M. f., Jr.;; Luxton, T. P. Insights for size-dependent reactivity of hematite nanomineral surfaces through Cu^{2+} sorption. *Geochim. Cosmochim. Acta* **2006,** *70*, 4095-4104.

(47) Tratnyek, P. G.; Johnson, R. L. Nanotechnologies for environmental cleanup. *Nano Today* **2006,** *1*, 44-48.

(48) Brant, J.; Lecoanet, H.; Wiesner, M. R. Aggregation and deposition characteristics of fullerene nanoparticles in aqueous systems. *J. Nanopart. Res.* **2005,** *7*, 545-553.

(49) Prasher, R.; Phelan, P. E.; Bhattacharya, P. Effect of aggregation kinetics on the thermal conductivity of nanoscale colloidal solutions (nanofluid). *Nano Lett* **2006,** *6*, 1529-1534.

(50) Dunphy Guzman, K. A.; Finnegan, M. P.; Banfield, J. F. Influence of surface potential on aggregation and transport of titania nanoparticles. *Environ. Sci. Technol.* **2006,** *40*, 7688-7693.

(51) Adams, L. K.; Lyon, D. Y.; Alvarez, P. J. J. Comparative eco-toxicity of nanoscale TiO_2, SiO_2, and ZnO water suspensions. *Wat. Res.* **2006,** *40*, 3527-3532.

(52) Nurmi, J. T.; Tratnyek, P. G.; Sarathy, V.; Baer, D. R.; Amonette, J. E.; Pecher, K.; Wang, C.; Linehan, J. C.; Matson, D. W.; Penn, R. L., et al. Characterization and properties of metallic iron nanoparticles: Spectroscopy, electrochemistry, and kinetics. *Environ. Sci. Technol.* **2005,** *39*, 1221-1230.

(53) Vikesland, P. J.; Heathcock, A. P.; Rebodos, R. L.; Makus, K. E. Particle size and aggregation effects on magnetite reactivity towards carbon tetrachloride. *Environ. Sci. Technol.* **2007,** *41*, 5277-5283.

(54) Amonette, J. E.; Workman, D. J.; Kennedy, D. W.; Fruchter, J. S.; Gorby, Y. A. Dechlorination of carbon tetrachloride by Fe(II) associated with goethite. *Environ. Sci. Technol.* **2000,** *34*, 4606-4613.

(55) Anderson, M. A.; Tejedor-Tejedor, M. I.; Stanforth, R. R. Influence of aggregation on the uptake kinetics of phosphate by goethite. *Environ. Sci. Technol.* **1985,** *19*, 632-637.

(56) Hansel, C. M.; Benner, S. G.; Neiss, J.; Dohnalkova, A.; Kukkadapu, R.; Fendorf, S. Secondary mineralization pathways induced by dissmilatory iron reduction of ferrihydrite under advective flow. *Geochim. Cosmochim. Acta* **2003,** *67*, 2977-2992.

(57) Pedersen, H. D.; Postma, D.; Jakobsen, R. Release of arsenic associated with the reduction and transformation of iron oxides. *Geochim. Cosmochim. Acta* **2006,** *70*, 4116-4129.

(58) Tronc, E.; Belleville, P.; Jolivet, J. P.; Livage, J. Transformation of ferric hydroxide into spinel by Fe(II) adsorption. *Langmuir* **1992,** *8*, 313-319.

(59) Silvester, E.; Charlet, L.; Tournassat, C.; Gehin, A.; Greneche, J.-M.; Liger, E. Redox potential measurements and Mössbauer spectrometry of Fe^{II} adsorbed onto Fe^{III} (oxyhdr)oxides. *Geochim. Cosmochim. Acta* **2005,** *69*, 4801-4815.

(60) Mulvaney, P.; Swayambunathan, V.; Grieser, F.; Meisel, D. Effect of the ζ potential on electron transfer to colloidal iron oxides. *Langmuir* **1990,** *6*, 555-559.

(61) Mulvaney, P.; Swayambunathan, V.; Grieser, F.; Meisel, D. Dynamics of interfacial charge-transfer in iron(III) oxide colloids. *J. Phys. Chem.* **1988,** *92*, 6732-6740.

(62) Mulvaney, P.; Cooper, R.; Grieser, F.; Meisel, D. Charge trapping in the reductive dissolution of colloidal suspensions of iron(III) oxides. *Langmuir* **1988,** *4*, 1206-1211.

(63) Schwertmann, U.; Cornell, R. M., *Iron Oxides in the Laboratory: Preparation and Characterization*. 2nd ed.; Wiley-VCH: New York, 2000; p 188.

(64) Burleson, D. J.; Penn, R. L. Two-step growth of goethite from ferrihydrite. *Langmuir* **2006,** *22*, 402-409.

(65) Penn, R. L.; Erbs, J. J.; Gulliver, D. M. Controlled growth of alpha-FeOOH nanorods by exploiting oriented aggregation. *J. Cryst. Growth* **2006,** *293*, 1-4.

(66) Phenrat, T.; Saleh, N.; Sirk, K.; Tilton, R. D.; Lowry, G. V. Aggregation and sedimentation of aqueous nanoscale zerovalent iron dispersions. *Environ. Sci. Technol.* **2007,** *41*, 284-290.

(67) Saleh, N.; Phenrat, T.; Sirk, K.; Dufour, B.; Ok, J.; Sarbu, T.; Matyjaszewski, K.; Tilton, R. D.; Lowry, G. V. Adsorbed triblock copolymers deliver reactive iron nanoparticles to the oil/water interface. *Nano Lett* **2005,** *5*, 2489-2494.

(68) Murad, E.; Cashion, J., *Mossbauer Spectroscopy of Environmental Materials and their Industrial Utilization*. Kluwer Academic Publishers: 2004.

(69) Nikolaev, V. I.; Shipilin, A. M.; Zakharova, I. N. On estimating the nanoparticle size with the help of the Mössbauer effect. *Phys. Solid State* **2001,** *43*, 1515-1517.

(70) Yen, S. T.; Liu, S. P.; Kolpin, D. W. Analysis of nitrate in near-surface aquifers in the midcontinental United States: An application of the inverse hyperbolic sine Tobit model. *Water Resources Research* **1996,** *32*, 3003-3011.

(71) Verwey, E. J. W.; Overbeek, J. T. G., *Theory of the Stability of Lyophobic Colloids*. Elsevier: Amsterdam, 1948; p 216.

(72) Li, X.-Y.; Logan, B. E. Permeability of fractal aggregates. *Wat. Res.* **2001,** *35*, 3373-3380.

(73) Berne, B. J.; Pecora, R., *Dynamic Light Scattering: With Applications to Chemistry, Biology and Physics*. Wiley: Dover, NY, 2000.

(74) Savage, N.; Diallo, M. S. Nanomaterials and water purification: Opportunities and challenges. *J. Nanopart. Res.* **2005,** *7*, 331-342.

(75) Zhang, H.; Penn, R. L.; Hamers, R. J.; Banfield, J. F. Enhanced adsorption of molecules on surfaces of nanocrystalline particles. *J. Phys. Chem. B* **1999,** *103*, 4656-4662.

(76) Mayo, J. T.; Yavuz, C.; Yean, S.; Cong, L.; Shipley, H.; Yu, W.; Falkner, J. C.; Kan, A. T.; Tomson, M.; Colvin, V. L. The effect of nanocrystalline magnetite size on arsenic removal. *Sci. Technol. Adv. Mat.* **2007,** *8*, 71-75.

(77) Villalobos, M.; Trotz, M. A.; Leckie, J. O. Variability in goethite surface site density: Evidence from proton and carbonate sorption. *J. Colloid Interf. Sci.* **2003,** *268*, 273-287.

(78) Rustad, J. R.; Felmy, A. R. The influence of edge sites on the development of surface charge on goethite nanoparticles: A molecular dynamic investigation. *Geochim. Cosmochim. Acta* **2005,** *69*, 1405-1411.

(79) Gaboriaud, F.; Ehrhardt, J.-J. Effects of different crystal faces on the surface charge of colloidal goethite (α-FeOOH) particles: An experimental and modeling study. *Geochim. Cosmochim. Acta* **2003,** *67*, 967-983.

(80) Jickells, T. D.; An, Z. S.; Andersen, K. K.; Baker, A. R.; Bergametti, G.; Brooks, N.; Cao, J. J.; Boyd, P. W.; Duce, R. A.; Hunter, K. A., et al. Global iron connections between desert dust, ocean biogeochemistry, and climate. *Science* **2005,** *308*, 67-71.

(81) Dixit, S.; Hering, J. G. Comparison of arsenic(V) and arsenic(III) sorption onto iron oxide minerals: Implications for arsenic mobility. *Environ. Sci. Technol.* **2003,** *37*, 4182-4189.

(82) Dong, D. M.; Nelson, Y. M.; Lion, L. W.; Shuler, M. L.; Ghiorse, W. C. Adsorption of Pb and Cd onto metal oxides and organic material in natural surface coatings as determined by selective extractions: new evidence for the importance of Mn and Fe oxides. *Water Res.* **2000,** *34*, 427-436.

(83) Chapelle, F. H.; Lovley, D. R. Competitive exclusion of sulfate reduction by Fe(III)-reducing bacteria: A mechanism for producing discrete zones of high-iron ground water. *Ground Water* **1992,** *30*, 29-36.

(84) Jeon, B. H.; Dempsey, B. A.; Burgos, W. D.; Royer, R. A. Reactions of ferrous iron with hematite. *Colloids Surf., A* **2001,** *191*, 41-55.

(85) Coughlin, B. R.; Stone, A. T. Nonreversible adsorption of divalent metal-ions (Mn(II), Co(II), Ni(II), Cu(II), and Pb(II)) onto goethite - effects of acidification, Fe(II) addition, and picolinic-acid addition. *Environ. Sci. Technol.* **1995,** *29*, 2445-2455.

(86) Jeon, B. H.; Dempsey, B. A.; Burgos, W. D. Kinetics and mechanisms for reactions of Fe(II) with iron(III) oxides. *Environ. Sci. Technol.* **2003,** *37*, 3309-3315.

(87) Silvester, E.; Charlet, L.; Tournassat, C.; Gehin, A.; Greneche, J. M.; Liger, E. Redox potential measurements and Mossbauer spectrometry of Fe(II) adsorbed onto Fe(III) (oxyhydr)oxides. *Geochim. Cosmochim. Acta* **2005,** *69*, 4801-4815.

(88) Peretyazhko, T.; Zachara, J. M.; Heald, S. M.; Jeon, B. H.; Kukkadapu, R. K.; Liu, C.; Moore, D.; Resch, C. T. Heterogeneous reduction of Tc(VII) by Fe(II) at the solid-water interface. *Geochim. Cosmochim. Acta* **2008,** *72*, 1521-1539.

(89) Tamaura, Y.; Ito, K.; Katsura, T. Transformation of gamma-FeO(OH) to Fe_3O_4 by adsorption of iron(II) ion on gamma-FeO(OH). *J. Chem. Soc., Dalton Trans.* **1983**, 189-194.

(90) Pecher, K.; Haderlein, S. B.; Schwarzenbach, R. P. Reduction of polyhalogenated methanes by surface-bound Fe(II) in aqueous suspensions of iron oxides. *Environ. Sci. Technol.* **2002,** *36*, 1734-1741.

(91) Cwiertny, D. M.; Handler, R. M.; Schaefer, M. V.; Grassian, V. H.; Scherer, M. M. Interpreting nanoscale size-effects in aggregated Fe-oxide suspensions: reaction of Fe(II) with goethite. *Geochim. Cosmochim. Acta* **2008,** *72*, 1365-1380.

(92) Beard, B. L.; Johnson, C. M. High precision iron isotope measurements of terrestrial and lunar materials. *Geochim. Cosmochim. Acta* **1999,** *63*, 1653-1660.

(93) Beard, B. L.; Johnson, C. M.; Skulan, J. L.; Nealson, K. H.; Cox, L.; Sun, H. Application of Fe isotopes to tracing the geochemical and biological cycling of Fe. *Chem. Geol.* **2003,** *195*, 87-117.

(94) Beard, B. L.; Johnson, C. M. Fe isotope variations in the modern and ancient earth and other planetary bodies. *Rev. Mineral. Geochem.* **2004,** *55*, 319-357.

(95) Bullen, T. D.; White, A. F.; Childs, C. W.; Vivit, D. V.; Schulz, M. S. Demonstration of significant abiotic iron isotope fractionation in nature. *Geology* **2001,** *29*, 699-702.

(96) Jang, J. H.; Mathur, R.; Liermann, L. J.; Ruebush, S.; Brantley, S. L. An iron isotope signature related to electron transfer between aqueous ferrous iron and goethite. *Chem. Geol.* **2008,** *250*, 40-48.

(97) Icopini, G. A.; Anbar, A. D.; Ruebush, S. S.; Tien, M.; Brantley, S. L. Iron isotope fractionation during microbial reduction of iron: The importance of adsorption. *Geology* **2004,** *32*, 205-208.

(98) Teutsch, N.; von Gunten, U.; Porcelli, D.; Cirpka, O. A.; Halliday, A. N. Adsorption as a cause for iron isotope fractionation in reduced groundwater. *Geochim. Cosmochim. Acta* **2005,** *69*, 4175-4185.

(99) Crosby, H. A.; Roden, E. E.; Johnson, C. M.; Beard, B. L. The mechanisms of iron isotope fractionation produced during dissimilatory Fe(III) reduction by Shewanella putrefaciens and Geobacter sulfurreducens. *Geobiology* **2007,** *5*, 169-189.

(100) Skulan, J. L.; Beard, B. L.; Johnson, C. M. Kinetic and equilibrium Fe isotope fractionation between aqueous Fe(III) and hematite. *Geochim. Cosmochim. Acta* **2002,** *66*, 2995-3015.

(101) Poulson, R. L.; Johnson, C. M.; Beard, B. L. Iron isotope exchange kinetics at the nanoparticulate ferrihydrite surface. *Am. Mineral.* **2005,** *90*, 758-763.

(102) Welch, S. A.; Beard, B. L.; Johnson, C. M.; Braterman, P. S. Kinetic and equilibrium Fe isotope fractionation between aqueous Fe(II) and Fe(III). *Geochim. Cosmochim. Acta* **2003,** *67*, 4231-4250.

(103) Shahar, A.; Young, E. D.; Manning, C. E. Equilibrium high-temperature Fe isotope fractionation between fayalite and magnetite: An experimental calibration. *Earth Planet. Sci. Lett.* **2008,** *268*, 330-338.

(104) Silverman, J.; Dodson, R. W. The Exchange Reaction between the 2 Oxidation States of Iron in Acid Solution. *J. Phys. Chem.* **1952,** *56*, 846-852.

(105) Campion, R. J.; Sutin, N.; Conocchioli, T. J. Inner-Sphere Activated Complex for Electron Exchange of Iron(II) + Monochloro Complex of Iron(III). *J. Am. Chem. Soc.* **1964,** *86*, 4591-4594.

(106) Tamura, H.; Goto, K.; Yotsuyan.T; Nagayama, M. Spectrophotometric determination of iron(II) with 1,10-phenanthroline in presence of large amounts of iron(III). *Talanta* **1974,** *21*, 314-318.

(107) Sabioni, A. C. S.; Huntz, A. M.; Daniel, A.; Macedo, W. A. A. Measurement of iron self-diffusion in hematite single crystals by secondary ion-mass spectrometry (SIMS) and comparison with cation self-diffusion in corundum-structure oxides. *Philos. Mag.* **2005,** *85*, 3643-3658.

(108) Freer, R.; Hauptman, Z. Experimental study of magnetite-titanomagnetite interdiffusion. *Phys. Earth Planet. Inter.* **1978,** *16*, 223-231.

(109) Atkinson, A.; Taylor, R. I. Diffusion of ^{55}Fe in Fe_2O_3 Single-Crystals. *J. Phys. Chem. Solids* **1985,** *46*, 469-475.

(110) Bruemmer, G. W.; Gerth, J.; Tiller, K. G. Reaction kinetics of the adsorption and desorption of nickel, zinc and cadminum by goethite. I. adsorption and diffusion of metals. *J. Soil Sci.* **1988,** *39*, 37-52.

(111) Mikutta, C.; Lang, F.; Kaupenjohann, M. Citrate impairs the micropore diffusion of phosphate into pure and C-coated goethite. *Geochim. Cosmochim. Acta* **2006,** *70*, 595-607.

(112) Fischer, L.; Brummer, G. W.; Barrow, N. J. Observations and modelling of the reactions of 10 metals with goethite: adsorption and diffusion processes. *Eur. J. Soil Sci.* **2007,** *58*, 1304-1315.

(113) Guskos, N.; Papadopoulos, G. J.; Likodimos, V.; Patapis, S.; Yarmis, D.; Przepiera, A.; Przepiera, K.; Majszczyk, J.; Typek, J.; Wabia, M., et al. Photoacoustic, EPR and electrical conductivity investigations of three synthetic mineral pigments: hematite, goethite and magnetite. *Mater. Res. Bull.* **2002,** *37*, 1051-1061.

(114) Weidler, P. G.; Hug, S. J.; Wetche, T. P.; Hiemstra, T. Determination of growth rates of (100) and (110) faces of synthetic goethite by scanning force microscopy. *Geochim. Cosmochim. Acta* **1998,** *62*, 3407-3412.

(115) Chun, C. L.; Penn, R. L.; Arnold, W. A. Kinetic and microscopic studies of reductive transformations of organic contaminants on goethite. *Environ. Sci. Technol.* **2006,** *40*, 3299-3304.

(116) Larsen, F.; Postma, D. Nickel mobilization in a groundwater well field: Release by pyrite oxidation and desorption from manganese oxides. *Environ. Sci. Technol.* **1997,** *31*, 2589-2595.

(117) Lack, J. G.; Chaudhuri, S. K.; Kelly, S. D.; Kemner, K. M.; O'Connor, S. M.; Coates, J. D. Immobilization of radionuclides and heavy metals through anaerobic bio-oxidation of Fe(II). *Appl. Environ. Microbiol.* **2002,** *68*, 2704-2710.

(118) Ren, J. H.; Packman, A. I. Coupled stream-subsurface exchange of colloidal hematite and dissolved zinc, copper, and phosphate. *Environ. Sci. Technol.* **2005,** *39*, 6387-6394.

(119) Erbs, M.; Hansen, H. C. B.; Olsen, C. E. Reductive dechlorination of carbon tetrachloride using iron(II) iron(III) hydroxide sulfate (green rust). *Environ. Sci. Technol.* **1999,** *33*, 307-311.

(120) Park, B.; Dempsey, B. A. Heterogeneous oxidation of Fe(II) on ferric oxide at neutral pH and a low partial pressure of 0(2). *Environ. Sci. Technol.* **2005,** *39*, 6494-6500.

(121) Becker, U.; Rosso, K. M.; Hochella, M. F. The proximity effect on semiconducting mineral surfaces: A new aspect of mineral surface reactivity and surface complexation theory? *Geochim. Cosmochim. Acta* **2001,** *65*, 2641-2649.

(122) Benner, S. G.; Hansel, C. M.; Wielinga, B. W.; Fendorf, S. Reductive dissolution and biomineralization of iron hydroxide under dynamic flow conditions. *Environ. Sci. Technol.* **2002,** *36*, 1705-1711.

(123) Rosso, K. M.; Smith, D. M. A.; Dupuis, M. An *ab initio* model of electron transport in hematite (α-Fe_2O_3) basal planes. *J. Chem. Phys.* **2003,** *118*, 6455-6466.

(124) Kerisit, S.; Rosso, K. M. Kinetic Monte Carlo model of charge transport in hematite (α-Fe_2O_3) *J. Chem. Phys.* **2007,** *127*.

(125) Kerisit, S.; Rosso, K. M. Computer simulation of electron transfer at hematite surfaces. *Geochim. Cosmochim. Acta* **2006,** *70*, 1888-1903.

(126) Wiederhold, J. G.; Kraemer, S. M.; Teutsch, N.; Borer, P. M.; Halliday, A. N.; Kretzschmar, R. Iron isotope fractionation during proton-promoted, ligand-controlled, and reductive dissolution of goethite. *Environ. Sci. Technol.* **2006,** *40*, 3787-3793.

(127) Handler, R. M.; Beard, B. L.; Johnson, C. M.; Scherer, M. M. Atom exchange between aqueous Fe(II) and goethite: An Fe isotope tracer study. *Environ. Sci. Technol.* **2009,** *43*, 1102-1107.

(128) Fortune, W. B.; Mellon, M. G. Determination of iron with o-phenanthroline - A spectrophotometric study. *Ind. Eng. Chem., Anal. Ed.* **1938,** *10*, 0060-0064.

(129) Postma, D. The Reactivity of Iron-Oxides in Sediments - a Kinetic Approach. *Geochim. Cosmochim. Acta* **1993,** *57*, 5027-5034.

(130) Mills, G. A.; Urey, H. C. The kinetics of isotopic exchange between carbon dioxide, bicarbonate ion, carbonate ion and water. *J. Am. Chem. Soc.* **1940,** *62*, 1019-1026.

(131) Cole, D. R.; Chakraborty, S., Rates and mechanisms of isotopic exchange. In *Stable Isotope Geochemistry*, 2001; Vol. 43, pp 83-223.

(132) Cousins, A. B.; Badger, M. R.; von Caemmerer, S. In *C-4 photosynthetic isotope exchange in NAD-ME- and NADP-ME-type grasses*, 2008; Oxford Univ Press: 2008; pp 1695-1703.

(133) Davis, J. A.; Hayes, K. F., Geochemical processes at mineral surfaces: an overview. In *Geochemical Processes at Mineral Surfaces*, Davis, J. A.; Hayes, K. F., Eds. American Chemical Society: Washington, DC, 1986; Vol. 323, pp 2-18.

(134) Kosmulski, M., *Chemical Properties of Material Surfaces*. CRC Press: New York, 2001.

(135) Jang, J. H.; Brantley, S. L. Investigation of Wustite (FeO) Dissolution: Implications for Reductive Dissolution of Ferric Oxides. *Environ. Sci. Technol.* **2009,** *43*, 1086-1090.

(136) Ulrich, H. J.; Stone, A. T. Oxidation of chlorophenols adsorbed to manganese oxide surfaces. *Environ. Sci. Technol.* **1989,** *23*, 421-428.

(137) Di-Ruggiero, J.; Gounot, A. M. Microbial manganese reduction mediated by bacterial strains isolated from aquifer sediments. *Microb. Ecol.* **1990,** *20*, 53-63.

(138) Lovley, D. R.; Phillips, E. J. P. Novel mode of microbial energy metabolism: organic carbon oxidation coupled to dissimilatory reduction of iron or manganese. *Appl. Environ. Microbiol.* **1988,** *54*, 1472-1480.

(139) Widerlund, A., Ingri, J. Redox cycling of iron and manganese in sediments of the Kalix River estuary, Northern Sweden. *Aquat. Geochem.* **1996,** *2*, 185-201.

(140) van der Zee, C.; Slomp, C. P.; Rancourt, D. G.; de Lange, G. J.; van Raaphorst, W. A Mossbauer spectroscopic study of the iron redox transition in eastern Mediterranean sediments. *Geochim. Cosmochim. Acta* **2005,** *69*, 441-453.

(141) Stollenwerk, K. G. Geochemical interactions between constituents in acidic groundwater and alluvium in an aquifer near Globe, Arizona. *Appl. Geochem.* **1994,** *9*, 353-369.

(142) Villinski, J. E.; O'Day, P. A.; Corley, T. L.; Conklin, M. H. In situ spectroscopic and solution analyses of the reductive dissolution of MnO2 by Fe(II). *Environ. Sci. Technol.* **2001,** *35*, 1157-1163.

(143) Postma, D.; Appelo, C. A. J. Reduction of Mn-oxides by ferrous iron in a flow system: Column experiment and reactive transport modeling. *Geochim. Cosmochim. Acta* **2000,** *64*, 1237-1247.

(144) Krishnamurti, G. S. R.; Huang, P. M. Influence of manganese oxide minerals on the formation of iron oxides. *Clays Clay Miner.* **1988,** *36*, 467-475.

(145) Laha, S.; Luthy, R. G. Oxidation of aniline and other primary aromatic amines by manganese dioxide. *Environ. Sci. Technol.* **1990,** *24*, 363-373.

(146) McCobb, T. D.; LeBlanc, D. R.; Walter, D. A.; Hess, K. M.; Kent, D. B.; Smith, R. L. Phosphorus in a ground-water contaminant plume discharging to Ashumet Pond, Cape Cod, Massachusetts. *U.S. Geological Survey Water Resources Investigations Report 02-4306* **1999**, 70p.

(147) Abel, R. Scavenging of particulate and dissolved lead compounds by coprecipitation with manganese oxyhydroxides. Electronic M.S. thesis, Virginia Tech, 1998.

(148) Coulston, G. W.; Thompson, E. A.; Herron, N. Characterization of VPO catalysts by X-ray photoelectron spectroscopy. *J. Catal.* **1996,** *163*, 122-129.

(149) Hadnadjev, M.; Vulic, T.; Marinkovic-Neducin, R.; Suchorski, Y.; Weiss, H. The iron oxidation state in Mg-Al-Fe mixed oxides derived from layered double hydroxides: An XPS study. *Appl. Surf. Sci.* **2008,** *254*, 4297-4302.

(150) Morgan, J. J.; Stumm, W. Colloid-Chemical Properties of Manganese Dioxide. *J. Coll. Sci.* **1964,** *19*, 347-&.

(151) Morup, S.; Topsoe, H.; Lipka, J. Modified theory for Mossbauer spectra of superparamagnetic particles: Application to Fe_3O_4. *J. Phys. Colloque* **1976,** *6*, 287-290.

(152) Cudennec, Y.; Lecerf, A. Topotactic transformations of goethite and lepidocrocite into hematite and maghemite. *Solid State Sci.* **2005,** *7*, 520-529.

(153) Deng, Y. W.; Stumm, W. Reactivity of aquatic iron(III) oxyhydroxides: Implications for redox cycling of iron in natural-waters. *Appl. Geochem.* **1994,** *9*, 23-36.

(154) Appelo, C. A. J.; Van der Weiden, M. J. J.; Tournassat, C.; Charlet, L. Surface complexation of ferrous iron and carbonate on ferrihydrite and the mobilization of arsenic. *Environ. Sci. Technol.* **2002,** *36*, 3096-3103.

(155) Gorski, C. A.; Scherer, M. M. Influence of magnetite stoichiometry on Fe(II) uptake and nitrobenzene reduction. *Environ. Sci. Technol.* **2009,** *In press*.

(156) Jolivet, J.-P.; Tronc, E. Interfacial electron transfer in colloidal spinel iron oxide. Conversion of Fe_3O_4-γFe_2O_3 in aqueous solution. *J. Colloid Interface Sci.* **1988,** *125*, 688-701.

(157) Regazzoni, A. E.; Urrutia, G. A.; Blesa, M. A.; Maroto, A. J. G. Some observations on the composition and morphology of synthetic magnetites obtained by different routes. *J. Inorg. Nucl. Chem.* **1981,** *43*, 1489-1493.

(158) Zahir, K. O.; Keshtkar, H. A colorimetric method for trace level determination of cobalt in natural and waste water samples. *Int. J. Environ. Anal. Chem.* **1998,** *72*, 151-162.

(159) Hurlbert, S. H. Pseudoreplication and the Design of Ecological Field Experiments. *Ecological Monographs* **1984,** *54*, 187-211.